INFORMATION TO USERS

This manuscript has been reproduced from the microfilm master. UMI films the text directly from the original or copy submitted. Thus, some thesis and dissertation copies are in typewriter face, while others may be from any type of computer printer.

The quality of this reproduction is dependent upon the quality of the copy submitted. Broken or indistinct print, colored or poor quality illustrations and photographs, print bleedthrough, substandard margins, and improper alignment can adversely affect reproduction.

In the unlikely event that the author did not send UMI a complete manuscript and there are missing pages, these will be noted. Also, if unauthorized copyright material had to be removed, a note will indicate the deletion.

Oversize materials (e.g., maps, drawings, charts) are reproduced by sectioning the original, beginning at the upper left-hand corner and continuing from left to right in equal sections with small overlaps.

Photographs included in the original manuscript have been reproduced xerographically in this copy. Higher quality 6" x 9" black and white photographic prints are available for any photographs or illustrations appearing in this copy for an additional charge. Contact UMI directly to order.

ProQuest Information and Learning
300 North Zeeb Road, Ann Arbor, MI 48106-1346 USA
800-521-0600

UMI®

A NUMERICAL INVESTIGATION OF THE TRANSFORMATION OF A LONG-LIVED MESOVORTEX INTO A TROPICAL STORM

By

Ning Bao

SUBMITTED IN PARTIAL FULFILMENT OF THE REQUIRMENTS FOR THE
DEGREE OF
DOCTOR OF PHILOSOPHY
AT
McGILL UNIVERSITY
MONTREAL, QUEBEC
August, 1999

Abstract

The evolution of a long-lived mesovortex and its transformation into a tropical storm are studied by a three dimensional mesoscale model. The major aspects of the work are: 1) to demonstrate the mesoscale predictability of a long-lived mesoscale convective system (MCS) from a mid-level vortex over land to a tropical storm over ocean, 2) to understand the processes involved in the transformation of a mid-level continental vortex into a tropical storm, and 3) to perform sensitivity experiments to assess the impact of model physics on an idealized simulation.

The major conclusions are:

The 90-h real-data simulation shows that the mesoscale model reproduces very well much of the meso-β-structures and the evolution of the long-lived MCS. These include the development and dissipation of the continental mesovortex, the initiation of a new MCS both in time and in space, the genesis of a surface mesolow over the warm Gulf Stream water, the track and the deepening of the surface cyclone into a "tropical storm", the maintenance of a mid-level mesovortex system, and the propagation of a large-scale cold front with respect to the surface cyclone.

The simulation also shows that the mid-level mesovortex provides persistent convergence at its southern periphery for the continued convective development, whereas the convectively enhanced low-level flow increases surface energy fluxes over the warm

water causing further conditional instability. Such feedback processes lead to the rapid deepening of the "tropical storm".

An idealized simulation was performed to eliminate the possible influence of the cold frontal system on the genesis of the tropical storm. The initial conditions resemble the basic structure of the subtropical high in the real-data case, but without the embedded frontal system. The simulation reproduces almost all of the essential features in the real-data simulation. In particular, the eye-like warm core structure of the tropical storm is well simulated. By decomposing the vertical relative vorticity into the curvature vorticity and the shear vorticity, it is shown that the amplification of a low-level vortex after 36 h arises mainly from the increase of curvature vorticity. The quasi-Lagrangian θ budget calculation shows that the descending motion in the center of the surface cyclone contributes to the formation of the warm core at 800 hPa.

The results of sensitivity experiments demonstrate the impact of model physics on the idealized simulation. Using the Betts-Miller scheme, we showed that the model fails to simulate the multiple-episodes of convective activity which are present in observational studies of tropical cyclogenesis and in the simulation using the Kain-Fritsch scheme. We further found that the surface latent heat fluxes represent a dominant factor in the production of CAPE to maintain the persistent convection. Finally, we discussed the cumulative cooling effect by long-wave radiation on the destabilization of the environment of the storm.

Résumé

L'évolution d'un mésovortex persistant et sa transformation en tempête tropicale sont simulés au moyen d'un modèle numérique tridimensionnel à méso-échelle. Les aspects majeurs de ce travail consistent: 1) de démontrer la prévisibilité d'un système de convection a méso-échelle (SCM) depuis l'apparition d'un vortex a méso-échelle continental à son développement en tempête tropicale océanique sur une période de 90 heures. 2) de comprendre les processus impliqués lors de cette transformation aux niveaux intermédiaires de la troposphère. 3) d'effectuer différents tests de sensibilité afin de déterminer l'impact de divers processus physiques sur les simulations numériques.

Les conclusions principales sont les suivantes:

La simulation en données réelles de 90 heures démontre que le modèle numérique à méso-échelle reproduit bien les caractéristiques méso-β et l'évolution à longue durée du système. Ceci inclut le développement et la dissipation du mésovortex continental l'apparition d'un nouveau SCM. De plus, le modèle reproduit l'intensification et la trajectoire de la dépression de surface antérieure à la formation de la tempête tropicale et arrive à maintenir un mésovortex aux niveaux intermédiaires de la troposphère.

La simulation démontre également que le mésovortex à mi-niveaux entretient la convergence dans la partie sud-est du système précipitant. Les flux de la surface générés par la convection provoquent la dissipation d'énergie de surface au-dessus des eaux

chaudes, ce qui a pour effet d'augmenter l'instabilité conditionnelle des basses couches, amenant à une intensification rapide de la tempête tropicale.

Une simulation idéalisée a été entreprise afin d'exclure l'influence possible du front froid sur la genèse de cette tempête tropicale. Les conditions initiales forment la structure de base d'un anticyclone subtropical décrit dans ce cas à partir de données réelles, privé de front froid. Le modèle reproduit presque toutes les caractéristiques essentielles associées au cycle de vie du mésovortex précédent issu de la simulation avec données réelles. En décomposant le tourbillon relatif vertical associé au système en terme de basculement et de cisaillement, notre analyse démontre que l'intensification d'un vortex dans les basses couches après 36 heures est dû en grande partie au basculement. Le calcul du bilan quasi-Lagrangien de θ montre une subsidence dans le centre du cyclone à la surface qui contribue à la formation d'un noyau central chaud à 800 hPa.

D'autres parts, les expériences de sensibilité révèlent l'impact des divers processus physiques sur la simulation idéalisée. Le modèle ne reproduit pas les épisodes multiples de convection observés durant la genèse de cyclones tropicaux, que ce soit en utilisant le schéma de Betts-Miller ou bien celui de Kain-Fritsch. L'étude montre également que les flux de chaleur latente sont un facteur dominant dans la production d'énergie potentielle nécessaire au maintient de la convection. Finalement, les effets du refroidissement radiatif sur l'environnement du système sont aussi discutés.

Acknowledgment

I wish to express my great appreciation to my thesis advisors, Drs. Da-Lin Zhang and M. K. Yau, for their continuous encouragement and inspiration during the course of this work. I am especially grateful to Dr. M. K. Yau for undertaking the task of supervision when I was under the most difficult circumstance during the study. I wish also to thank Dr. J. R. Gyakum for his valuable comments during the progress of my work.

I am indebted to my friends in the department both for their moral support and for scientific discussions during the long years of my project. The valuable suggestions of Dr. Yubao Liu are appreciated. I would like to thank Badri Nagarajan for his timely proof-reading of the thesis and Stephen Dery for the French version of the abstract. Mr. Alan Schwartz is acknowledged for his technical assistance in solving computer problems.

I would like to thank my parents for their love and support.

Finally, I would like to express gratitude to my beloved wife, Zimei, for her constant moral support and understanding during the past six years, an unforgettable journey of my life.

MANUSCRIPTS AND AUTHORSHIP

In accordance with Thesis Specification of the " Guidelines Concerning Thesis Preparation" (Faculty of Graduate studies and Research), the following text is cited:

" Candidates have the option of including, as part of the thesis, the text of one or more papers submitted, or to be submitted, for publication, or clearly-duplicated text (not the reprints) of one or more published papers. These texts must conform to the Thesis Preparation Guidelines with respect to font size, line spacing and margin sizes and must be bound together as an integral part of the thesis.

The thesis must be more than a collection of manuscripts. All components must be integrated into a cohesive unit with a logical progression from on chapter to the next. In order to ensure that the thesis has continuity, connecting texts that provide logical bridges between the different papers are mandatory.

The thesis must conform to all other requirements of the "Guidelines for Thesis preparation" in addition to the manuscripts. The thesis must include the following: a table of contents; an abstract in English and French; an introduction which clearly states the rational and objectives of the research, a comprehensive review of the literature ; a final conclusion and summary.

As manuscripts for publication are frequently very concise documents, where appropriate, additional material must be provided (e.g. in appendices) in sufficient detail to allow a clear and precise judgment to be made of the importance and originality of the research reported in the thesis.

In general, when co-authored papers are included in a thesis the candidate must have made a substantial contribution to all papers included in the thesis. In addition, the candidate is required to make an explicit statement in the thesis as to who contributed to such work and to what extent. This statement should appear in a signal section entitled " Contributions of Authors" as a preface to the thesis. The supervisor must attest to the accuracy of this statement at the doctoral oral defense. Since the task of the examiners is made more difficult in these cases, it is in the candidate's interest to clearly specify the responsibilities of all the authors of the co-authored papers."

Contributions of Authors

Chapter 2-3* of this thesis are based on papers published in *Mon. Wea. Rev.* The results presented in these papers originated from the research work I performed within the context of the Ph.D. project. The co-author of the papers, Dr. Da-Lin Zhang contributed to providing the supervision of the project and writing the papers.

* The introduction and conclusion sections of Chapter 2-3 have been modified to provide continuity between each of these chapters and subsequent chapters. Chapter 3 has been slightly modified based on the recent results of the research. In addition, Chapter 2-3 have also been reformatted to conform with the requirements of the McGill thesis format.

Statement of Originality

The thesis contains the following original material:

1. The first real-data simulation using a three dimensional mesoscale model to study the transformation of a long-lived mesovortex into a tropical storm.

2. The finding that the long-lived mid-level mesovortex, as it moves toward the warm Gulf Stream water, provides the necessary forcing for the initiation and organization of deep convection, whereas the new convective system contributes to the amplification of the low-level cyclonic vorticity.

3. An idealized simulation of the transformation of a mid-level mesovortex into a tropical storm in a near equivalent barotropic environment. The identification of the amplification of the low-level vortex mainly due to the increase of curvature vorticity.

4. The identification of the eye-like structure during the rapid deepening of a tropical storm in the simulation. The finding that the descending motion in the "eye" of the storm is slow but persistent. The application of quasi-Lagrangian θ budget calculation to assess the contribution of the descending motion in the "eye" of the storm to the formation of the warm core at 800 hPa.

5. A sensitivity study associated with the cumulus parameterization scheme, surface energy fluxes and long wave radiation. Of particular interest is the sensitivity of the idealized simulation to the Betts-Miller scheme.

Table of Contents

List of Figures

Chapter 1

Introduction

1.1 Background

Despite considerable research in tropical meteorology, tropical cyclogenesis remains one of the least explored areas. In contrast to mid-latitude cyclogenesis, no widely accepted theory has been proposed. Indeed, even the terminology "tropical cyclogenesis" is unclear and researchers have often used inconsistent or nonstandard definitions. According to Zehr (1992), 'genesis' refers to weather systems and their ongoing atmospheric processes during the time periods before their initial designation as a tropical storm or tropical cyclone. The term 'intensification' refers to the time periods after tropical storm forms. Fig. 1.1 (from Zehr 1992) depicts typical genesis and intensification periods, their associated minimum sea level pressure (MSLP) and the maximum surface wind.

The occurrence of tropical storms is associated with a number of climatological parameters. Gray (1979) summarized the six factors favoring tropical cyclogenesis as:

(1) Sufficiently high Coriolis parameter

(2) High low-level relative vorticity

(3) Small tropospheric vertical wind shear

(4) High sea surface temperature

(5) Large surface to 500 hPa lapse rates for equivalent potential temperature

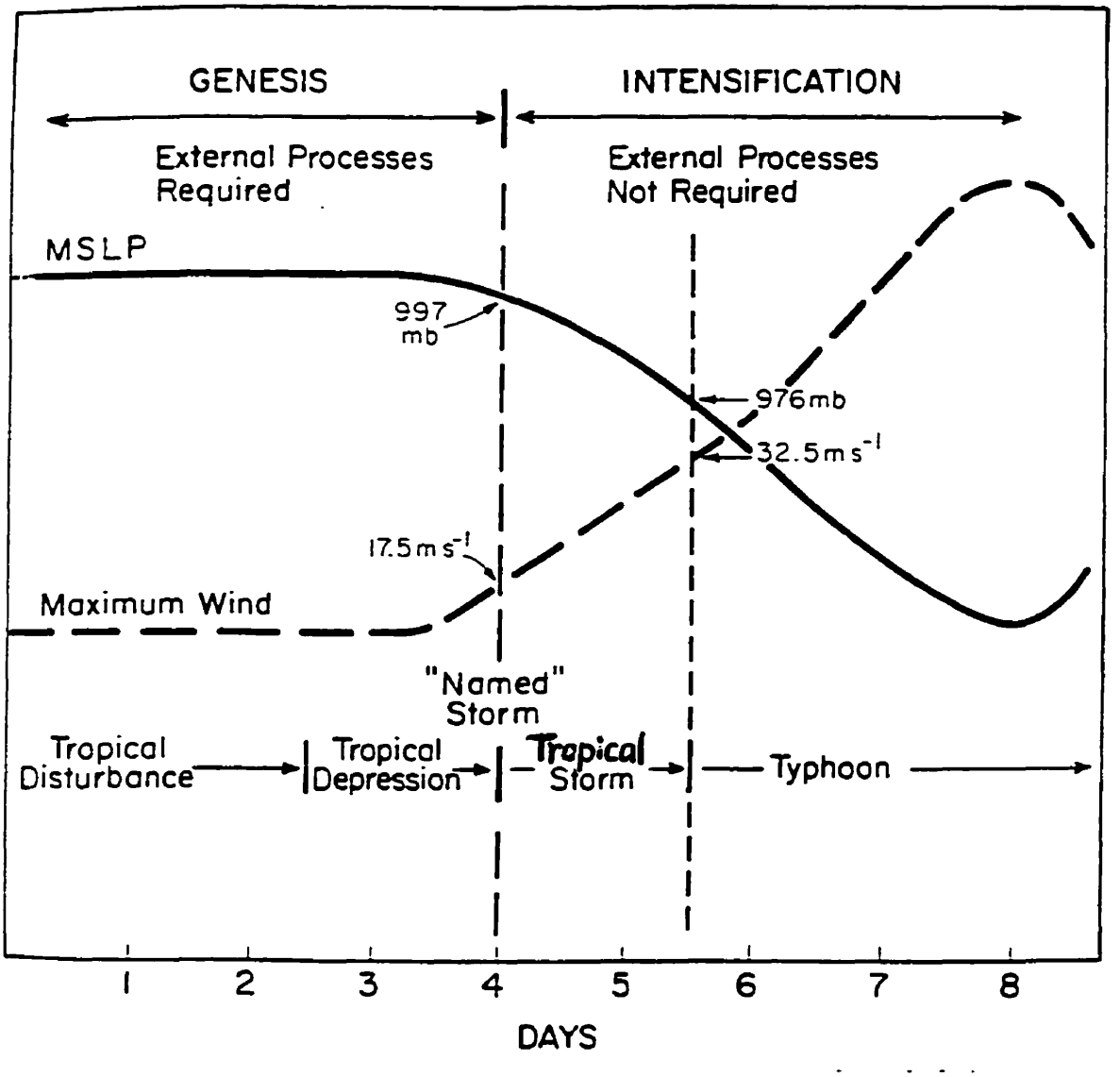

Fig. 1.1 Depiction of typical genesis and intensification periods and their associated MSLP and maximum surface wind speed. (from Zehr, 1992)

(6) High mid-tropospheric relative humidity

Although these factors define some necessary conditions for the formation of tropical cyclones, they offer limited predictive capability. The reason is that the last three parameters change little with time in the tropics. In addition, conditions 2 and 3 are not sufficient conditions. Therefore, individual case of genesis requires additional ingredients.

1.1.1 Early studies

Early studies (1960s ~ early 1980s) on tropical cyclogenesis were mostly based on synoptic analysis and composite technique. Synoptic analysis is useful in depicting the detailed evolution of a particular tropical storm. The analysis by Hawkins et al, (1968), and Vincent et al (1979) reveal the existence of large scale vertical motion over most of the troposphere and the occurrence of low-level confluence in the environment of some pre-tropical storm disturbances. Other studies (e.g. Sadler, 1976, 1978; Dovark, 1975) suggest that the Tropical Upper Tropospheric Trough (TUTT) influences the evolution of low-level tropical disturbances. However, Simpson et al (1968) argues that the TUTT may actually suppress the development of the incipient disturbance.

The composite method has been applied to many observations to extract the averaged features in the formation of tropical storms (Frank, 1977a,b; Gray, 1979; McBride, 1981a,b). Is has also been used to analyze the structure and behavior of easterly waves over Africa and eastern Atlantic (Burpee, 1972, 1974, 1975). Results of composite studies have advanced our knowledge of the structure of developing

tropical storms and the associated important physical processes. However, they still fall short in the ability to discriminate between a developing and a non-developing case.

Theoretical studies represent another tool to explore possible mechanisms responsible for tropical cyclogenesis. (Yanai, 1961; Shapiro, 1977; Schubert and Hack, 1982). They range from baroclinic instability, non-linear amplification of a finite-amplitude wave, to the relationship between convective heating and inertia stability. The most influential one is the CISK (Conditional Instability of the Second Kind) theory proposed by Charney and Eliassen (1964). It describes the unstable growth of a group of convective clouds on a spatial (400 km -500 km) and time scale larger than that of an individual cumulus. Low-level frictional convergence is proposed to be a dominant mechanism leading to the establishment of a self-sustaining process. However, Gray (1998) argues that CISK occurs on a small spatial scale of around 50 km. It is therefore not a mechanism for 'genesis', but a mechanism for 'developed' tropical cyclone.

Kurihara and Tuleya (1981) reported on a numerical simulation of the genesis of a tropical storm. Their initial condition is based on the mean condition at 80° W during Phase III of GATE and a specified wave disturbance. The 96 hour simulation shows that a tropical depression develops and the MSLP falls by 5.8 hPa. However, their coarse horizontal resolution (5/8 °) precludes the proper resolution of the meso-β scale features associated with the genesis stage. In addition, Gray (1998) argues that

to use the mean state during Phase III of GATE as the initial condition is not realistic in the simulation of tropical cyclogenesis.

Although the early large-scale studies presented above are useful in suggesting possible conditions for tropical cyclogenesis, their results are by no means conclusive. The reasons are that (i) some conditions favorable for genesis are also observed in non-developing cases, and (ii) on the synoptic scale, the difference in environment conditions between developing and non-developing cases is small.

1.1.2 Recent studies

Since the late 1980s, information on the mesoscale becomes available. In particularly, observation from satellites has led to the recognition of important mesoscale features in tropical cyclogenesis (Zehr, 1992; Harr and Elsberry, 1996; Bister and Emanuel, 1997; Gray, 1998). Based on the analysis of satellite, aircraft reconnaissance and conventional data, Zehr (1992) proposed a two-stage conceptual model for the formation of tropical storms. Each of the stages is marked by a maximum in convective activity associated with a MCS. A period of 1-3 days when little convective activity occurs separates the two stages. The formation of a tropical storm is associated with the outbreak of convection during the second stage.

Gray (1998) further elaborated on Zehr's conceptual model. He suggests that the triggering of convection during the two stages may be due to external forced convergence (EFC) related perhaps to the trade-wind and the monsoon trough. Another important type of EFC is the rapid increase of convergence near a disturbance as it moves into an environment with a quasi-stationary wind field. Gray

states that this type of EFC is a crucial feature in a large numbers of cases for tropical cyclogenesis such as the one reported by Harr et al (1996). Once EFC initiates deep convection, under certain circumstances (e.g. concentrated relative vorticity, low vertical wind shear), the small area of MCSs may develop a self-sustaining process with continuous increase in convergence leading to the unstable growth of an area of convection. This self-sustaining process is termed internal forced convergence (IFC). The establishment of IFC is hypothesized to lead to the formation of a tropical storm with the inner convection organizing itself into an eye-wall type of convection, which in turn prolongs the IFC process.

Based on data collected in hundreds of flights into tropical disturbances by the US Air Force, Gray (1998) suggests that during the first stage, EFC acts to trigger strong and concentrated convection over a small area (MCS scale) from which a mid-level mesoscale convective vortex (MCV) develops. Using Doppler wind data during the Tropical Experiment in Mexico (TEXMEX), Bister and Emanuel (1997) documented the existence of such an MCV which led to the formation of Hurricane Guillermo. Davidson et al. (1990) found in the Australian Monsoon Experiment, that Tropical Cyclones Irma and Jason initially had their maximum intensity in the middle troposphere. Once formed, these MCVs may continue to exist even after the convection associated with their parent MCSs has dissipated. These weak vortices may last between 1-3 days during a period of minimum convective activity. However, they set the stage for the spin-up of the disturbance if a later EFC initiates organized deep convection near the vortex. This second round of deep convection

may lead to the start of IFC. Since the probability of the second round of EFC occurring at the location of the previous vorticity is not high, the second stage of development does not occur frequently.

In contrast to the generation of mid-level circulation by the first stage of mesoscale convection, the second EFC usually brings about low-level convergence and concentration of cyclonic vorticity (Gray 1998). In addition, the mid-level MCV, generated in the first stage, displays a warm core above with a cold pool below (Bister and Emanuel, 1997). To form a tropical storm characterized by a warm core with concentrated vortex at low-levels, the cold pool must be transformed into a warm core structure during the second stage. The mechanism of transformation of the cold pool associated with mid-level MCV into a warm core low-level vortex is still unclear. Gray (1998) suggests that the large inertial stability associated with the strong circulation of the mid-level MCV prevents the generation of large convergence at these levels during the second stage. On the other hand, the low levels represent a region of much smaller vorticity and inertial stability and favor the development of low-level convergence by the second EFC. Bister and Emanuel (1997) propose that the diabatic cooling from the evaporation of stratiform rain transports the mid-level mesovortex downward to the sea surface. Rogers (1999) proposes that the redevelopment of convection within the center of a long-lived mesovortex may amplify the warm core leading to its penetration toward the surface.

Based on the above review, it appears that one of the mechanism for tropical cyclogenesis involves the presence of a long-lived mid-level mesovortex (survives

long enough for the second EFC to act), the triggering of a second round of deep convection near the previous mesovortex, the transformation of the cold pool into a warm core structure and the development of self-sustaining deep convection within an environment climatologically favorable for the formation of tropical cyclones.

While a considerable amount of work has been done to explore the relation between MCVs and tropical cyclogenesis through observation, only a few numerical studies have been carried out. Bister and Emanuel (1997) used a nonhydrostatic axisymmetric model to simulate the evolution of an initially cold-pool mid-level vortex into a tropical cyclone. They demonstrated that the downward expansion of an evaporatively cooled vortex could lead to the development of a surface-flux-driven warm core cyclone. However, due to the limitation of an axisymmetric model, the simulation cannot address the effect of the relative flow through the system on the formation of the vortex, and the effect of the mean flow on surface fluxes and the outer convection.

A major problem in a simulation is the specification of initial conditions. The conventional weather network could not resolve many characteristics of MCSs, especially over the ocean. Although data sets collected during field programs over tropical oceans can alleviate this problem, they are still insufficient to generate a spatially consistent data set to be used as initial conditions in three-dimensional models. Furthermore, the time scale of the processes involved in the transformation of a MCV into a tropical cyclone is about a couple of days. During this time, the mesovortex may undergo cycles including generation, dissipation and re-

intensification. Simulation of multiple cycles associated with meso-β features over such time scales by a mesoscale model remains a highly challenging task.

To avoid the problem of the sparseness of data over the ocean, one may resort to the results of observational studies of MCSs around the world (Velasco and Fritsch, 1987; Miller and Fritsch, 1991; Laing and Fritsch, 1993) which show many similarities between MCSs over the continental US and over the tropics. Some land-based MCSs have been shown to evolve into tropical storms. It is therefore useful to approach the problem of tropical cyclogenesis by exploring how long-lived MCV initiated over land in the midlatitude can evolve into a tropical storm over the warm water at lower latitudes. Such an approach also has some observational basis.

Since the early 1980s, numerous observational studies have focused on mesoscale convective complexes (MCCs) or mesoscale convective systems (MCSs) formed over the eastern slope of the Rocky Mountains during the summer season (Maddox, 1980; Rodgers et al. 1983; 1985; Augstuine and Howard 1988, 1991). Some of these MCCs frequently produce mesoscale convective vortex (MCV) and can persist for several days (Menard and Fritsch, 1989; Bartels and Maddox, 1991). Wetzel et al. (1983) reported on the evolution of 14 MCCs within eight days in August 1977 with their initial positions over the Colorado Rockies. Three of the MCCs maintain their identity for more than 3 days as they move east toward the Atlantic Ocean. Fritsch et al (1994) documented a case of long-lived MCS. It formed over eastern Colorado and underwent five cycles of convective development and finally dissipated over a period of 3 days. The characteristic multiple episodes of

convection associated with the MCS indicates some similarities to the two stage formation of tropical cyclones (Zehr 1992, Gray 1998). Also of interest is the case analyzed by Bosart and Sanders (1981, hereafter BS81). This long-lived MCS originated from South Dakota and it was responsible for the 19-20 July 1977 Johnstown flash flood. The MCS underwent nearly 30 hours of dissipation and reintensified as an oceanic cyclone after it moved over the warm water of the Gulf Stream. It is interesting to note that BS81 named the oceanic cyclone a "tropical storm". The same term was also used by Velasco and Fritsch (1987) and Bister and Emanuel (1997).

Since such MCSs originally formed over land in mid-latitudes (central US) where observational data are relatively abundant, considerable efforts have been made to understand their structure and evolution. Studies have suggested that a mid-level mesovortex can be generated in the trailing stratiform region with a warm core appearing in the upper levels and a cold pool appearing below (Zhang and Fritsch 1987, 1988a; Bartels and Maddox, 1991, Chen and Frank, 1993). In addition, when the circulation of the mesovortices is sufficiently intense and balanced (Davis and Weisman 1994; Raymond 1992), the presence of a weak-sheared environment and an inertially stable circulation may help to extend the life of the MCS. We remark that the aforementioned modeling works (Zhang and Fritsch 1987, Chen and Frank 1993) focused on the genesis stage of MCVs and their early evolution. The simulations were for a period less than 36 hours before the MCVs transform into tropical storms. Therefore, it is highly desirable to perform a longer-term simulation to understand the

transformation process. Important questions that need answers are: What environmental conditions will help the transformation? During the transformation, what processes are involved? What are the relationships between the formation of a tropical storm and deep convection? How does a mid-level mesovortex evolve into a tropical storm with intense cyclonic vorticity at low levels? What processes are responsible for the transformation of a cold pool system into a warm core system?

1.2 Objectives and approach

The objectives of this study are (a) to perform a 90 h simulation of the MCSs responsible for the July 1977 Johnstown, Pennsylvania, flood (the MCSs resulted in a barotropic oceanic cyclogenesis after moving offshore), (b) to conduct a 72 h idealized simulation of the transformation of a convectively generated midlevel MCV into a tropical storm having a low-level warm core vortex; and (c) to analyze the two sets of simulation results to shed light on the important questions posed above. We begin with the case documented by BS81 for our real-data simulation experiment. The choice is motivated by the following reasons: (i) it is a well-known and well-documented case of a long-lived MCS that evolved into a tropical storm. The mid-level mesovortex associated with the MCSs originated over land in the midlatitude and the data coverage was good, and (ii) Zhang and Fritsch (1986, 1987), hereafter referred to as ZF86 and ZF87 respectively, have performed a successful 18 h simulation which reproduces very well the evolution and the structures of a mid-level mesovortex. Our 90 hour simulation covers the whole duration during which the dissipated MCS transforms into a tropical storm.

As will be shown in Chapter 2 and 3, the real data simulation is not straight forward because of the presence of a frontal system that may affect the formation of the tropical storm. We therefor also conduct an idealized simulation with much simplified initial conditions. Specifically, the large scale flow resemble the basic structure of the subtropical high presented in BS81, but without the embedded frontal system. The near equivalent barotropic environment in the idealized simulation is similar to the situation over tropical regions where the majority of tropical cyclones occur. An analytical initialization package is used to generate the initial conditions for the idealized simulation.

The Penn State-National Center of Atmospheric Research (PSU/NCAR) mesoscale model (version 4) is used in this study. Some improvements to the model were made to obtain a realistic simulation. These include the incorporation of a modified version of a long-wave radiation scheme and the implementation of a moving nested grid technique. In addition, a channel domain configuration, which is necessary to allow long time integration with idealized initial conditions, is added to the modeling system.

In Chapter 2, the 90 hours real data simulation is presented. The model simulated well the meso-β structure and the evolution of the long-lived MCS as verified against the detailed analyses of Hoxit et al. (1978, hereafter H78) and BS81. The mechanism associated with the redevelopment of deep convection leading to the formation of the tropical storm is then addressed. The analyses of the vertical

structure of the mesovortex, the calculation of vorticity and heat budget for the real-data simulation are given in Chapter 3.

Chapter 4 describes the idealized simulation. Comparison is made between the idealized and the real-data simulations to clarify the processes responsible for the amplification of a low-level vorticity maximum and the formation of the warm core. The sensitivity of the simulation to the cumulus parameterization schemes, the role of surface energy fluxes and the cumulated effect of long wave radiation in destabilizing the environment of the storm are discussed in Chapter 5. Finally, Chapter 6 presents a summary of the results and possible future work.

Chapter 2

Oceanic cyclogenesis[1] as induced by a mesoscale convective system moving offshore: a 90 h real-data simulation

2.1 Introduction

As discussed in Chapter 1, ZF86 and ZF87 have presented a successful 18 h simulation of the squall line and MCC that were associated with the Johnstown flood events, as verified against the detailed analyses of H78 and BS81. The integration was terminated at 18 h because the model simulated MCC and convectively generated circulation weakened rapidly thereafter. However, as documented by BS81, a surface trough left behind by the dissipated MCC appeared to "reintensify" to a closed mesolow at 36 h after it drifted into the Atlantic Ocean. Then, the surface mesolow developed to tropical storm intensity in 24 h (i.e., at 0000 UTC 23 July) before it was overtaken by a large-scale cold-frontal system. Therefore, for the purpose of the present study, we utilize a much larger domain size to extend the previously documented 18 h integration of the case to 90 h, at which time the surface cyclone had reached tropical storm intensity.

[1] We used the term oceanic cyclogenesis in this chapter because when the paper, related to this chapter, was submitted for publication, one of the reviewer suggested the use of the term 'oceanic barotropical cyclone', instead of "tropical storm" referred to by others for this case. In this thesis, the oceanic cyclogenesis is used interchangeably with tropical cyclogenesis. This applies also to oceanic cyclone and tropical storm or cyclone.

The outline of this chapter is as follow. Section 2.1 describes briefly the major improvements and additions of the PSU-NCAR mesoscale model for this study. Section 2.3 provides verification of the 90 h simulation against BS81's surface analysis and other available observation, and presents the basic sequence leading to the development of the "tropical storm." The relative significance of convective versus large-scale forcing in the cyclogenesis will also be evaluated. Section 2.4 shows the simulated structure and evolution of a mesovortex[2] , its associated short-wave trough and larger-scale flows in relation to the surface development. Section 2.5 discusses the mechanism(s) by which the oceanic storm[3] is initiated as the dissipated MCC moves offshore, and then organized after 60 h into the model integration. A summary and concluding remarks are given in the final section.

2.2 Model description and initial conditions

The numerical model used in this study is an improved version of the PSU-NCAR three-dimensional, hydrostatic, nested-grid, mesoscale model (MM4, see Anthes et al. 1987), which is similar to that used by ZF86, Zhang et al. (1988a) and Zhang (1989) for the 18 h simulation of the same case. The fundamental features of the model used for this study include (i) a two-way interactive nested-grid procedure that allows incorporation of realistic topography (Zhang et al. 1986b); (ii) an explicit moisture scheme containing prognostic equations for cloud water (ice) and rainwater(snow) (Hsie et al. 1984; Zhang 1989; Dudhia 1989); (iii) the Blackadar

[2] A mesovortex is defined here as a closed wind circulation at a scale of greater than 150 km with its relative vorticity larger than that of the local Coriolis parameter f (see ZF87).

[3] Note that the "oceanic storm" is used here to denote organized convection occurring near the mesovortex after it moves over the ocean. It should be distinguished from the "tropical storm" in Chapters 4, 5, and 6.

boundary layer parameterization scheme (Zhang and Anthes 1982); and (iv) the specification of the coarse-mesh outermost lateral boundary conditions by linearly interpolating 12 h observations according to Perkey and Kreitzberg (1976).

2.2.1 Model improvements

While the basic model framework is the same as that used in ZF86 and Zhang (1989), There are a few important additions and improvements that have been incorporated in order to obtain realistic simulations of long-lived MCSs. First, the Kain-Fritsch (1990, 1993, hereafter KF) convective parameterization scheme is used instead of the Fritsch-Chappell (1980) scheme for the fine-mesh portion of the model in order to minimize the differences between subgrid-scale and grid-scale moist physics representations (Molinari and Dudek 1992; Zhang et al. 1994), while for the coarse mesh the Anthes-Kuo (Anthes et al. 1987) scheme is still utilized. The KF scheme is based upon the same closure assumptions as the Fritsch-Chappell scheme, but uses a cloud model that is designed to allow updraft entrainment and detrainment rates to vary more realistically as a function of environmental conditions. In particular, the latest version of the KF scheme allows the direct feedback of both vapor and hydrometeors to the grid scale, thereby eliminating the uncertainty associated with the sedimentation process in the Fritsch-Chappell scheme (see Zhang et al. 1994). The coupling of the KF scheme with the explicit moisture scheme tends to help reproduce different types of mesoscale precipitation systems (Zhang et al. 1988; Molinari and Dudek 1992).

Second, an improved version of the Garand (1983) broadband infrared radiation scheme is adopted to account for the effect of persistent cloudiness associated with the long-lived MCSs under investigation. The Garand radiation scheme includes water vapor line and continuum absorption, clouds, carbon dioxide, and ozone with tabulated transmission functions based on the HITRAN (Rothman et al. 1987), spectroscopic databank. This version of the scheme is very similar to that used in the operational version of the Canadian regional finite-element model (Benoit et al. 1989), except that cloud amount is defined here in accordance to the model-predicted grid-scale cloud water (ice) and rainwater(snow) instead of relative humidity. The scheme is computed every 30 min and it costs less than 5% of total CPUs due to the use of the tabulated database. Krishnamurti et al. (1991), Kurihara and Tuleya (1981), and others have documented the importance of including long wave radiative transfer in obtaining realistic simulations of tropical storms.

Third, because the long-lived MCSs under study traverse a great distance during the 90 h period (see Fig. 2.1), a simple grid-moving strategy is developed to reduce the storage and computational costs. In this strategy, the fine-grid mesh can be moved at the times and speeds as specified. A shift of the nested-grid mesh is achieved by changing coarser-mesh points at the leading side to fine-mesh points and fine-mesh points at the trailing side to coarse-mesh points. All prognostic variables in the newly formed coarse- and fine-mesh regions are obtained by nine-point averaging and interpolation, respectively. Special care has been taken to ensure the consistency

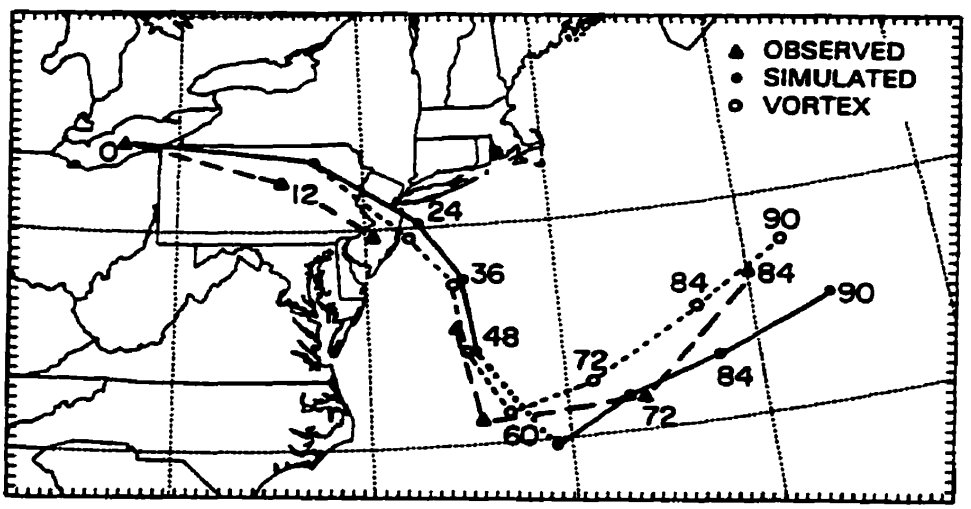

Fig. 2.1 Comparison of the tracks of the observed surface mesolow (long dashed) with the model-simulated (solid) over the fine-mesh domain. Dotted portion of the simulated track indicates the dissipation of the previous mesolow and the formation of a new mesolow. The path of the 700 hPa vortex center is also given (25 km for fine mesh; similarly in the rest of figures.

of topography (Zhang et al. 1986b) and surface parameters for each shift of the nested-grid mesh.

Fourth, the geographic distribution of the surface parameters, that is , moisture availability, roughness, albedo, and thermal inertial, which determine surface energy budgets and the development of the planetary boundary layer (PBL), is derived from the land-use data archived at NCAR using MM4's standard processing programs, rather than specified as that in ZF86.

The nested-grid ratio is 1: 3 with a fine-mesh length of 25 km and a coarse-mesh length of 75 km. The (x, y, σ) dimensions of the coarse and fine meshes are 59 x 45 x 19 and 85 x 49 x 19, respectively. The vertical terrain-following coordinate σ is defined as $\sigma = (p - p_t)/(p_s - p_t)$, where p_t is the pressure at the model top (in this case 70 hPa) and p_s is the surface pressure. Figures 2.1 and 2.2 show the fine-mesh (at the initial time) and coarse-mesh domains, respectively (whereas the fine-mesh domain after 60 h integration is given in Fig. 2.16). See Anthes et al. (1987), ZF86, Zhang et al. (1988), and Zhang(1989) for other details of the model being used.

2.2.2 Initial Conditions

The nested-grid model is initialized at 1200 UTC 19 July 1977 using the same dataset and same procedures as those described by ZF86, and then integrated to 90 h. The model initial conditions at 700 hPa and the surface are given in Fig. 2.2. Sea surface temperatures (SST) are also plotted, which are derived from the National Meteorological Center (NMC, now referred to as the National Centers for Environmental Prediction) global analysis and enhanced by ship reports and buoy

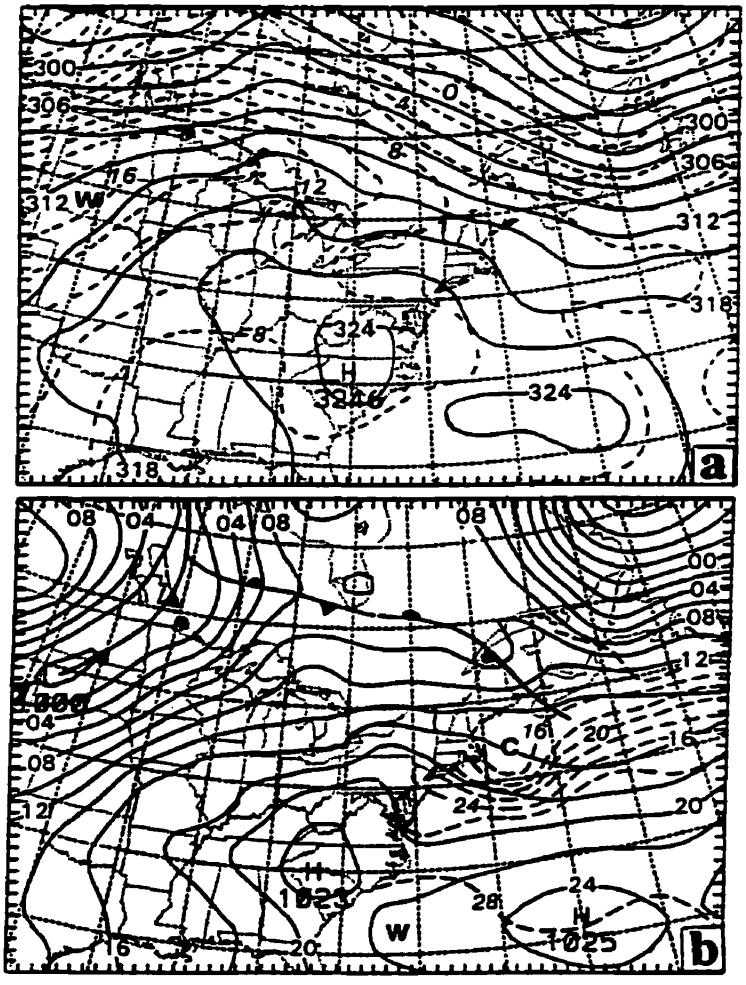

Fig. 2.2 Model initial conditions over the coarse-mesh domain at 1200 UTC 19 July 1977. (a) Geopotential heights (solid) at intervals of 3 dam and temperature (dashed) at intervals of 2°C at 700 hPa. (b) Sea level pressures at intervals of 2 hPa, labeled as the excess over 1000 hPa, e.g., "0.8" = 1008 hPa; similarly for the rest of figures. Dashed marked on the frame are mesh grids (75 km for coarse mesh; similarly in the rest of figures).

data. One can see that most of the eastern United State is under general anticyclonic flow around a quasistationary subtropical high centered in the western Atlantic. Because of this flow structure, there is a continuous flow of warm and moist air into the Mid-Atlantic States (see H78; ZF86). A sea level pressure trough associated with a short-wave trough aloft, which is evident over the Great Lakes region, is superposed on the large-scale (subtropical) ridge. BS81 showed that this mesoscale disturbance has propagated with the MCSs since its initiation in South Dakota 3 days earlier. Associated with the short-wave trough is a nearly balanced vortex circulation in the midtroposphere (see ZF86 and ZF87). As will be seen later, this trough/vortex system also moves eastward at the same speed as the surface trough (or later mesolow) during the subsequent 90 h. Evidently, this trough system plays an important role in inducing favorable upward motion for the initiation of new convection over Lake Erie at the model initial time (see ZF86). To the west of the trough, strong warm advection occurs in the lowest 300-400 hPa (Fig. 2.2a), and it decreases rapidly upward (see BS81 and ZF86). Farther to the north is strong baroclinicity associated with a large-scale frontal system that extends from central Canada into the northern high plains of the United States. It is this cold front that will catch up with the oceanic cyclone near the end of the 90 h integration. As Zhang and Fritsch (1988b) demonstrated with a series of sensitivity simulations, this frontal system provides a favorable environment for the development of the MCSs, but its forcing is too remote to determine the structure and evolution of the MCSs during the first 18 h integration.

2.3 Numerical Simulations

In this section, we document the sequence of events from the initial convective development over land to the final "tropical storm" stage over ocean, and verify the 90 h simulation against available observations. ZF86 have shown that the first 18 h model integration reproduces many of the different aspects of the MCC and squall line that were responsible for the heavy rain over western Pennsylvania. These include the development of surface mesohighs, mesolows, and outflow boundaries, the propagation of mesoscale gravity waves and the evolution of midlevel short-wave trough and a mesovortex, as verified against detailed observational analyses by H78 and BS81. By 0600 UTC 20 July (i.e., 18 h into the integration), henceforth 20/06-18, the MCSs have dropped substantial rainfall over the Johnstown area and begun to dissipate quickly hereafter (see Fig. 2.3a). The MCSs left behind two surface mesohighs, that is, one over eastern Pennsylvania and the other over the west central portion of the state, with a surface mesolow in between (see , Fig. 2.4). Note that this surface mesolow was located in the trailing stratiform region to the north of the convective line. The mesolow was maintained for at least another 3 h as the MCC moved southeastward and dissipated, and then it weakened to a mesotrough (see H78). The evolution of the surface mesolow (or trough) in relation to the midlevel trough/mesovortex system is of particular relevance to the present study. Since H78, BS81, and ZF86 have discussed extensively the life cycle of the MCSs up to 20/06-18, we will focus mainly on the evolution of the system during the subsequent 72 h and identify the sequences leading to the eventual tropical-storm intensity.

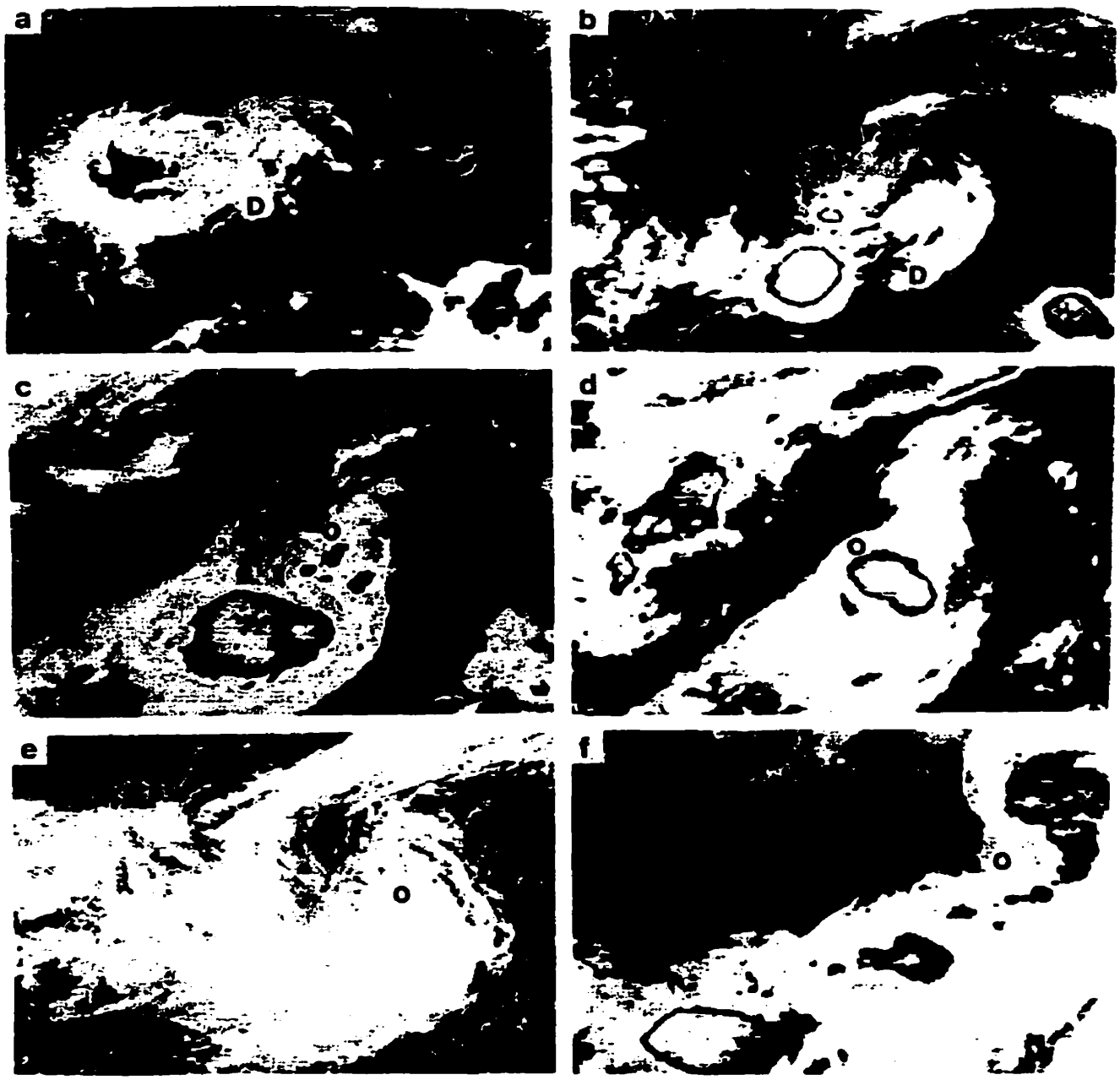

Fig. 2.3 *GOES-1* visible and infrared satellite imagery for (a) 1200 UTC 20, (b) 0001 UTC 21, (c) 1200 UTC 21, (d) 0001 UTC 22, (e) 1230 UTC 22, and (f) 0001 UTC 23 July 1977. Letters "D" and "o" denote the distribution of a line convection along a cold outflow boundary and the location of the surface cyclone center from the BS81 analysis, respectively.

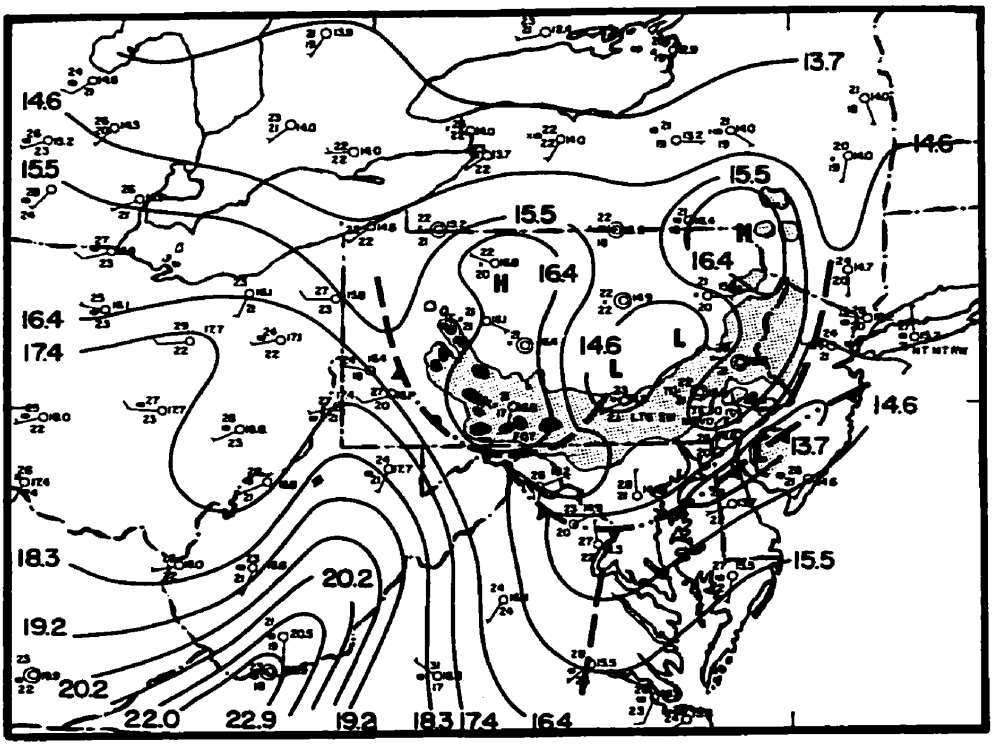

Fig. 2.4 Surface analysis for 0600 UTC 20 July 1977 (adapted from H78). Frontal symbols alternated with double dots indicate moist-downdraft outflow boundaries. The light shading denotes the level 1 radar echoes and the dark shading denotes level 3 (or greater) radar echoes. A full wind barb is 5 m s^{-1}.

Figures 2.1 and 2.5 compare, respectively, the tracks and central pressures of the simulated and observed surface mesolows. Because of the absence of significant signals during the system's dissipation stage, the central value and position of the surface low at 21/00-36 could not be identified from the BS81 analysis. Even so, it is still possible to see that the surface pressure center as well as the midlevel mesovortex moved first southeastward under the influence of anticyclonic flow associated with the subtropical high (see Fig. 2.2a), and then an abrupt changeover to northeastward displacement occurred after 22/00-60. One can also see that the system's forward movement slowed after it moved offshore, (i.e., <4 m s^{-1} vs. 6–8 m s^{-1} during the previous 24 h), and it accelerated to a speed of more than 9 m s^{-1} as the system rapidly deepened. Note that the oceanic cyclogenesis occurs at the south periphery of the trough/vortex (or "dissipated" low) at 22/00-60, thus causing a "jump" in the positions of the surface lows between the 48 h and 60 h simulations. In general, the model reproduces well the basic track of the surface mesolows, particularly the directional change, although the dissipated low is simulated to move a little faster and the "new" low slower than the observed (see Fig. 2.1). Likewise, the model reproduces well the dissipation rate of the "old" low after the Johnstown flooding episodes and the deepening of the "new" mesolow shortly after 21/12-48 (Fig. 2.5). At the end of the 84 h integration, the model-simulated cyclone is identical in intensity to the observed but its center departs about 200 km from the analyzed (Fig. 2.1 and 2.5). The difference in position, as will be shown, is mainly due to the use of

different parameters to define the cyclone center in the BS81 analysis and the simulation. The results are very encouraging since the simulation of convectively generated mesoscale circulation out to 84 h greatly exceeds the predictability limits indicated by traditional predictability concepts (see Anthes and Baumhefner 1984; Stull 1985).

Our analysis of the cyclogenesis events begins by examining closely how well the model reproduces mesoscale and larger-scale circulation in a sub-domain framework. As mentioned previously, the surface pressure perturbations weaken rapidly as the MCC dissipates. At 20/12-24, both the simulation and BS81's analysis show only a weak surface trough near the east coast in association with the dissipating MCC (see Fig. 9 in BS81 and Fig. 2.6 herein). Although remnant showers and thunderstorms continued in the lee of the Appalachians (see BS81 and Fig. 2.3a), the model convection over the region has disappeared during the late night hours. However, the model reproduces a line of remnant convection ahead of the surface trough, which, to be shown in section 2.5, results from convectively generated cold outflow interacting with conditionally unstable environment ahead. The line continues to propagate eastward, in a density current fashion, during the next 12 h, as indicated by the letter " D" in Figs. 2.3a, 2.3b, 2.6, and 2.7b. The simulated pressure perturbations associated with the convective line can also be inferred from surface wind reports in the BS81 analysis (see Fig. 2.7a).

At 21/00-36, the satellite imagery shows much less cloudiness associated with the dissipated MCC, and arc-shaped shallow cloudiness to the south that occurred

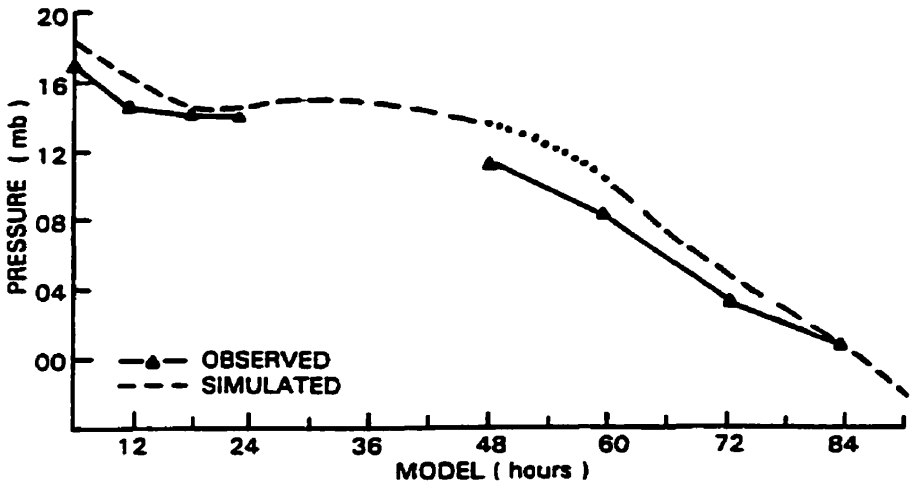

Fig. 2.5 Comparison of the observed (solid) and simulated (dashed) central pressures of the surface cyclone as a function of the model integration time. Dotted portion of the pressure trace indicates the dissipation of the previous mesolow and the formation of a new mesolow.

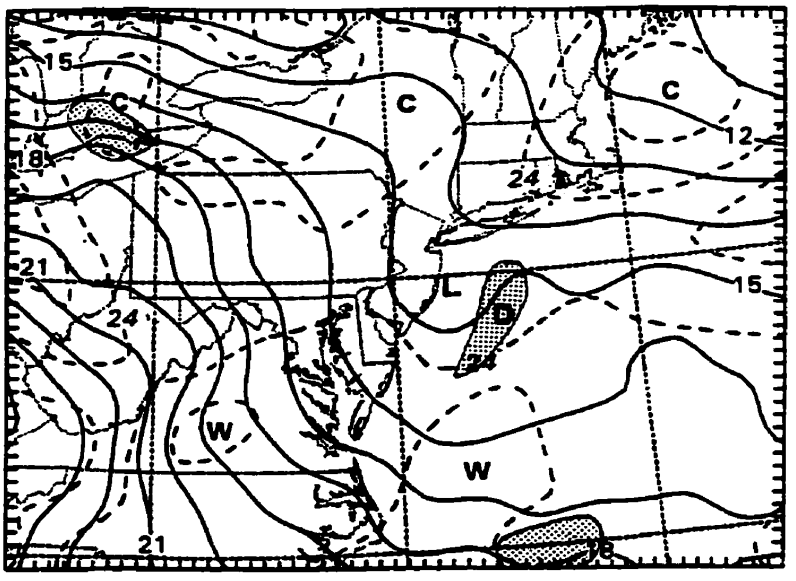

Fig. 2.6. Analysis of sea level pressure (solid, every 1 hPa) and surface temperature (dashed, every 2°C) over a fine-mesh subdomain from 24 h integration (20/12-24). Shading denotes the area of active model convection at the hour. Letter "D" denotes the distribution of a line convection along a cold outflow boundary.

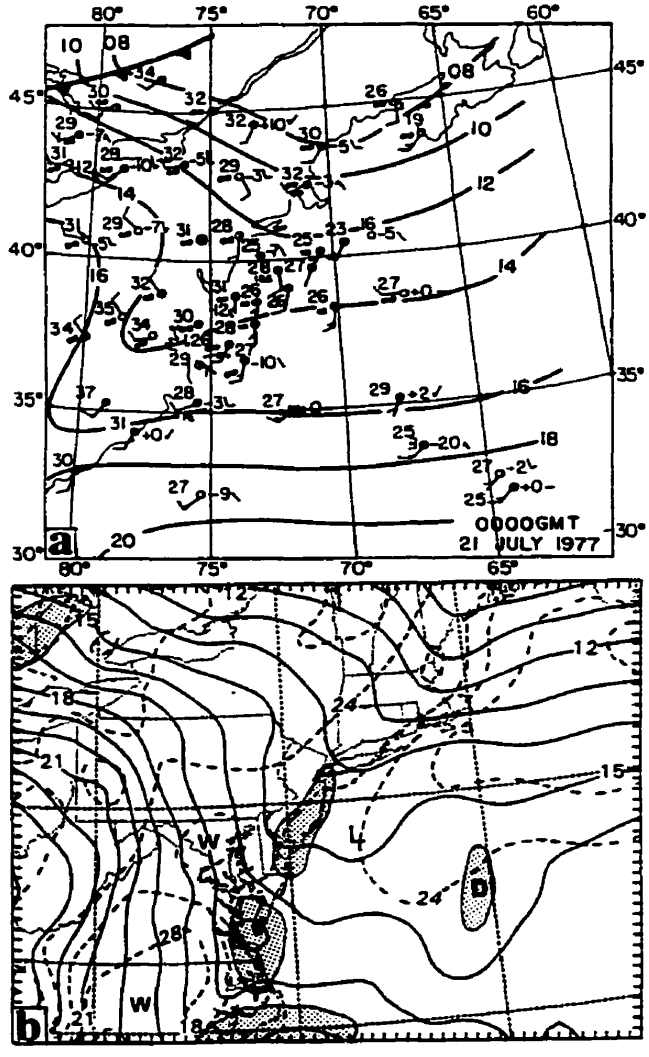

Fig. 2.7 (a) Surface analysis for 0000 UTC 21 July 1977 (adapted from BS81). Sea level pressure is contoured at every 2 hPa. A full wind barb is 5 m s^{-1}. (b) As in Fig. 2.6 but from 36 h integration (21/00-36).

along the outflow boundary of the system (see Fig. 2.3b). Meanwhile, both the BS81 analysis and the 36 h integration display the continued weakening of the convectively generated surface pressure perturbations; their pertinent signals are almost indiscernible at this time (Fig. 2.7). Of importance is that an intense convective system emerged at the southern periphery of the dissipated MCC, that is, near the North Carolina coast. Interestingly, the model also captures the development of such a convective system at nearly the right time and right location. As will be shown in section 2.5, this new MCS is triggered as a consequence of the mesovortex circulation interacting with the land-ocean thermal contrasts during the early afternoon hours. For a similar reason, the model appears to reproduce a few isolated deep convection off the Virginia coast. It can be seen from Figs. 2.3b-f that this new MCS expanded rapidly as it drifted eastward over the warm ocean surface (Fig. 2.2b). Later it became the dominant cloud system contributing to the deepening of the surface cyclone. For the sake of subsequent discussions, the dissipated and newly formed MCSs will be hereafter referred to as the continental and oceanic(or convective band) storms, respectively, although the latter could be regarded as the revival of the previously dissipated MCC.

Although the model reproduces most of the significant meteorological features, there are several notable deficiencies. For example, the model appears to have overproduced the intensity of the subtropical high by 2-4 hPa, as compared to the H78 and BS81 analyses. As a result, the low-level winds over the region tend to be overpredicted (cf. Figs. 2.8a and 2.8c). The simulated intensity of the subtropical

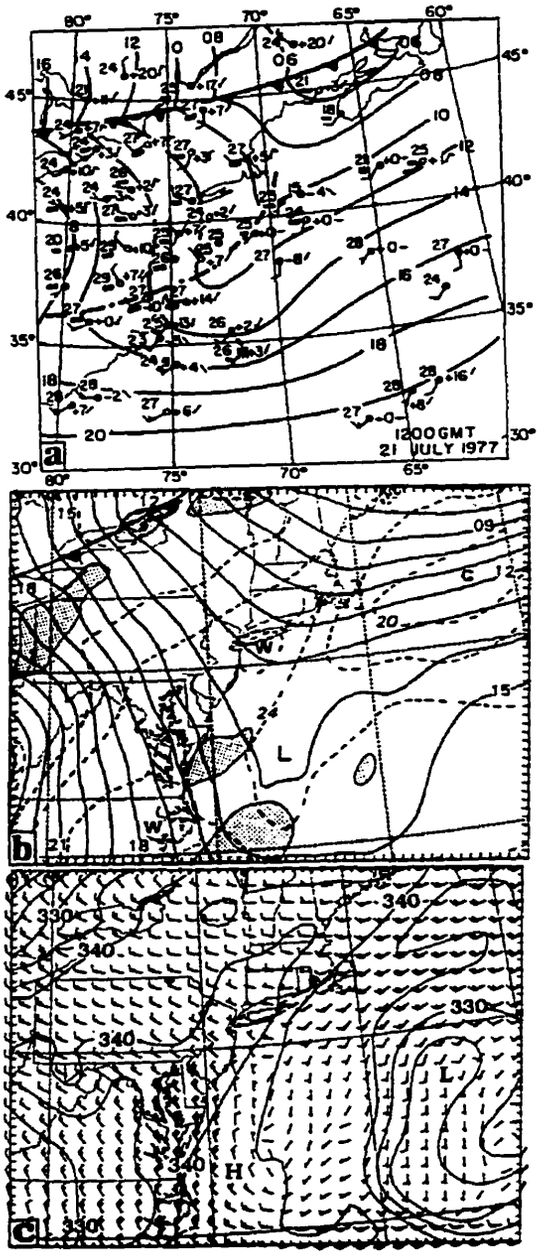

Fig. 2.8 (a) Surface analysis for 1200 UTC 21 July 1977 (adapted from BS81). Sea level pressure is contoured at every 2 hPa. (b) As in Fig. 2.6 but from 48 h integration. (21/12-48). The frontal position is specified according to θ_e at 900 hPa (see text). (c) Analysis of surface winds and 900 hPa θ_e (solid) at 5-K intervals from 48 h integration. Winds plotted according to convention with each pennant, full barb, and half barb denoting 25, 5, and 2.5 m s^{-1}, respectively.

high is in better agreement with the analyzed when the Garand radiation scheme was turned off, like that shown in ZF86, suggesting that this overproduction results partly from excessive long-wave cooling in the free atmosphere. The generation of an anomalously strong subtropical high appears to have pushed the surface trough (or midlevel mesovortex) a little too far to the southeast at 21/12-48 and 22/00-60, as compared to the BS81 analysis (see Fig. 2.1).

The oceanic storm continued to expand and intensify at night, and by 21/12-48, it developed into an MCC type of system (see Fig. 2.3c). Very encouragingly, the model reproduces reasonably well the continued expansion of the new convective system during the evening hours (Fig. 2.8). Evidently, the MCS of this size begins to exert an important influence on the subsequent evolution of the surface pressure perturbations. However, its influence is still not visible in the BS81 analysis. This may be attributable to the relatively poor density of observations offshore. In contrast, the 48 h integration shows a sign of consolidation of the surface pressure perturbations into a deeper mesotrough as the system moves southeastward to lower latitudes under the anticyclonic influence (Fig. 2.8b). Meanwhile, the southwesterly flow ahead of the trough helps transport tropical high-θ_e air into the region for subsequent convective development. Thus, this period may be considered as the onset of the surface cyclonic development.

Also at this time, a large-scale cold front, located about 600-700 km to the northwest of the trough, rapidly approaches. The model appears to reproduce well some isolated convective systems along the cold front (cf. Figs. 2.3c and 2.8b). It

should be mention that a moist isentrope (i.e.,θ_e) of 335 K at 900 hPa in conjunction with surface winds is used to determine the position of the cold front. This definition differs from that used in BS81's surface analysis. As will be seen later, this definition provides a better description of the frontal position, particularly the continuity of the frontal evolution, as the cold front moves over the warm ocean surface. This is because θ_e is a conserved variable in an inviscid, pesudoadiabatic flow.

At 22/00-60, the BS81 analysis shows the generation of a closed surface mesolow or cyclone[4] just slightly to the northwest of the oceanic storm (cf. Figs. 2.9a and 2.3d). (The cloud shields to the north seen in Figs. 2.3d were still associated with the dissipated MCC.) It is promising that the model captures reasonably well the timing and the location of the surface intensification, *even after 60 h into the integration* (see Fig. 2.9b); the difference in position from the BS81 analyzed is about 150 km too far to the southeast. The model also reproduces an area of weak-gradient mass to the north of the mesolow, as a result of the continued weakening of the low-level circulation associated with the trough/vortex system. In other words, the surface mesolow develops *at the sough periphery of rather than directly from the previous surface mesotrough or vortex*, which is consistent with the "jump" in the positions of the surface lows between the 48 and 60 h simulations (see Fig. 2.1). The model-simulated MCS intensifies and expands into an elongated convective band[5]

[4] Note that the "cyclone" or "mesolow" is used here to denote closed wind circulation or isobars, which is distinguished from oceanic storm and convective band.

[5] In general, the model-produced convective distribution should be verified against radar observations, particularly after extensive anvil clouds developed. Unfortunately, radar observations for the present study were not available. Thus, we can verify only the simulated convective development against the satellite imagery.

that is hugging the surface mesolow (cf. Figs. 2.9b and 2.3d). Furthermore, surface pressure gradients as well as surface winds along the oceanic storm have strengthened substantially during the previous 12h (cf. Figs. 2.8c and 2.9c).

It is important to notice that all the above scenarios occur as the mesoscale disturbance moves to the *warm Gulf Stream water* (see Fig. 2.2b), where the air-sea temperature differences (in the lowest 15-m layer) range from −1.5°C at its ambient to about −3°C beneath the convective band (due to downdraft cooling) at 22/00-60. Figure 2.10 shows the relative magnitudes of surface sensible and latent heat fluxes at this incipient stage. It is seen that large positive fluxes occur in the vicinity of the storm, more pronounced along the intensifying southwesterly flow with an average Bowen ratio of 0.2. The sensible heat flux has a magnitude similar to that found by Black and Holland (1995) in Tropical Cyclone Kerry (1979), whereas the latent heat flux is only one-third to one-quarter of that in Kerry (1979). Because of the parameterized moist downdraft effects, a zone of enhanced sensible heat flux coincides with the convective band or intense surface flow, but it is not the case with the latent heat flux (due to near-saturated downdrafts conditions). Several TOGA COARE[6] analyses have also found the increased sea-air thermal fluxes in the vicinity of MCSs due to the presence of anomalously cool, dry, and windy downdraft currents in the PBL (see Parsons et al. 1994; Mapes and Houze 1995). Thus, the result suggests that strong surface winds will enhance (i) the upward transfer of heat and moisture fluxes from the warm water surface, (ii) the transport of high-θ_e air in the

[6] The Tropical Ocean Global Atmosphere program's Coupled Ocean-Atmosphere Response Experiment (See Webster and Lukas 1992)

PBL along the southwesterly jetlike flow into the region having lower θ_e aloft. These processes, enhanced by the convectively induced grid-scale transport, appear to play an important role in generating a low-level high-θ_e tongue along the convective band, which in turn tends to destabilize atmospheric columns, especially near the leading portion of the tongue, thereby assisting the further organization of the oceanic storm along the surface jetlike flow (Figs. 2.9b,c).

After 22/00-60, the surface cyclone spins up rapidly and overpowers the low-level circulation associated with the trough/vortex system. By 22/12-72, its central pressure has deepened from 1008 to 1003 hPa, that is , 5 hPa in 12 h (see Fig. 2.11a). It is evident that the model reproduces closely the intensity and location of the surface mesolow at this time (cf. Figs. 2.11a,b). Similarly, the model reproduces well the continued expansion of the oceanic storm to the south and southeast of the surface mesolow (cf. Figs. 2.3e and 2.11b), as well as the cloud activity along the cold front. The simulated pressure trough in the wake of the storm conforms to the reported surface pressure falls in the BS81 Analysis. We will see in Chapter 3 that this represents part of the contribution of the vortex/trough system to the cyclogenesis, as the weak-gradient air mass is wrapped around cyclonically (cf. Figs. 2.9b,c and 2.11b,c). Rapid intensification of the surface flow also takes place during the 24 h period. For example, the southerly surface winds ahead of the cyclone, which were never more than 5 m s^{-1} at 48 h, increase to more than 15m s^{-1} by 72h (cf. Figs. 2.8c and 2.11c). As a result of the deepening, a closed cyclonic circulation formed ahead of the cold front, with enhanced northward transport of high-θ_e air and more intense

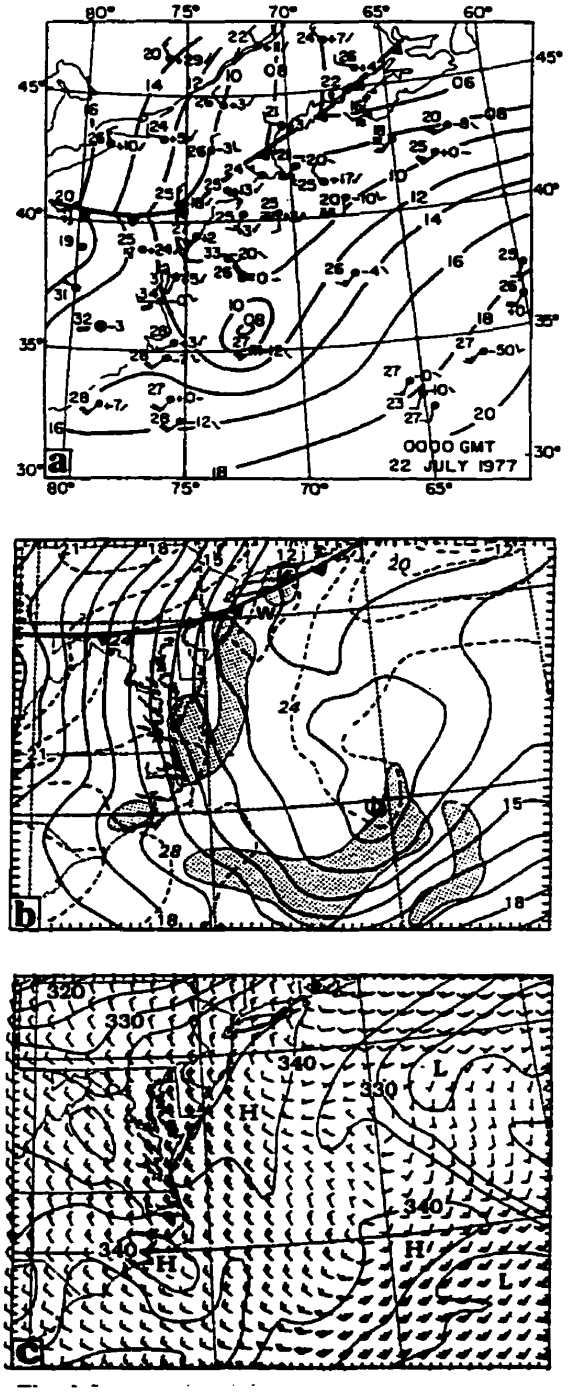

Fig. 2.9 As in Fig. 2.8 but for 0000 UTC 22 July 1977 and 60 h integration (i.e., at 22/00-60).

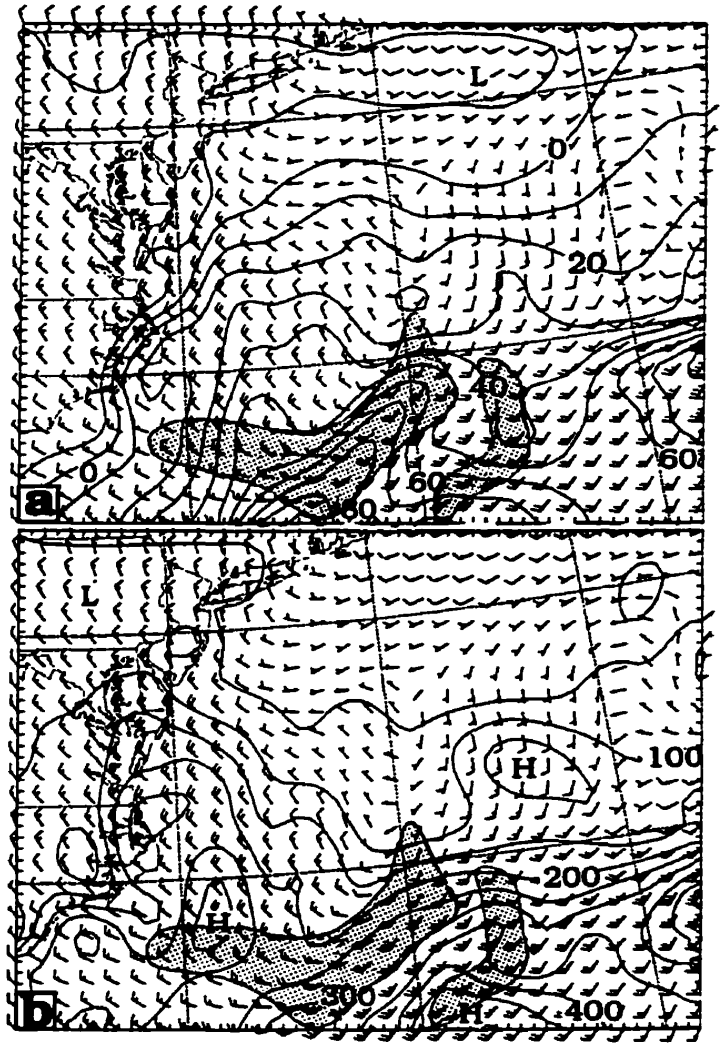

Fig. 2.10 Simulated surface (a) sensible heat flux at intervals of 10 W m^{-2} and (b) latent heat flux at intervals of 50 W m^{-2}, superposed with surface winds at 22/00-60. A full barb is 5 m s^{-1}. Shading denotes the distribution of the oceanic storm (see Fig. 2.9).

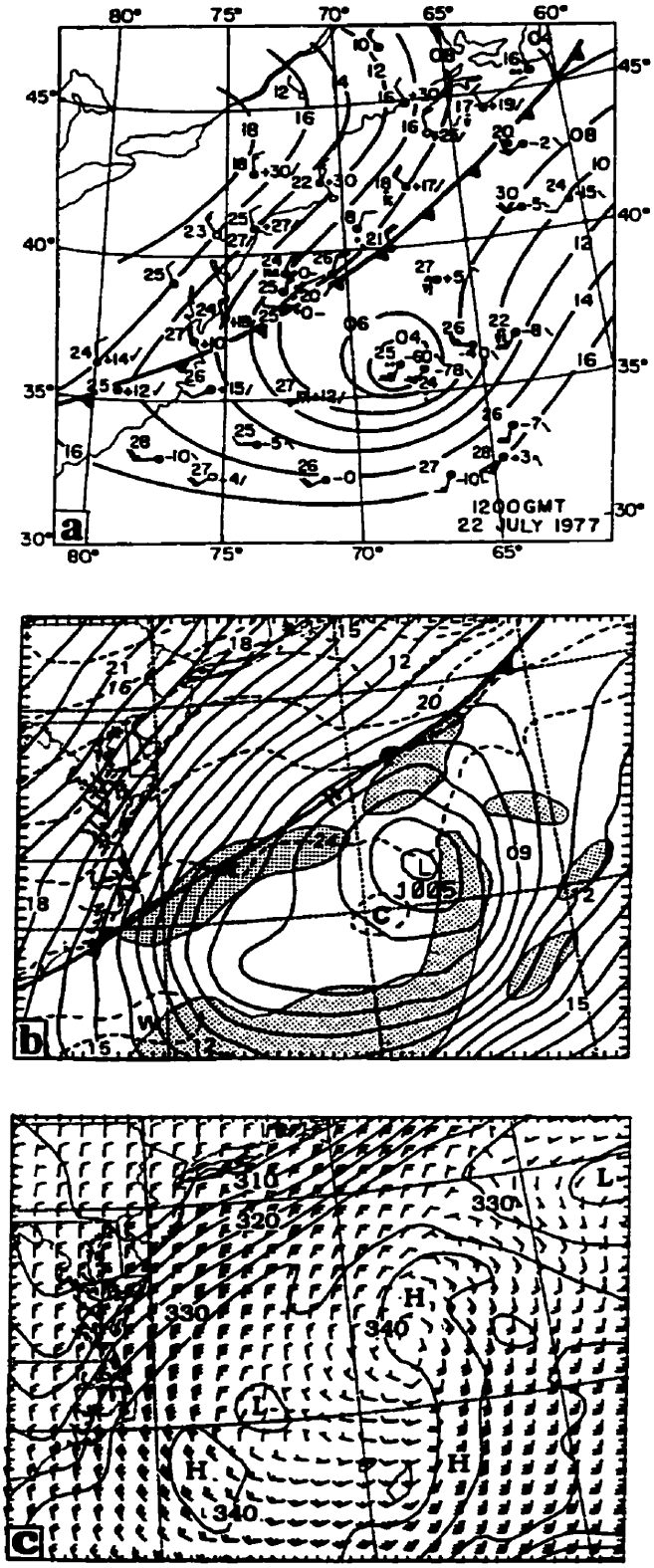

Fig. 2.11 As in Fig. 2.8 but for 1200 UTC 22 July 1977 and 72 h integration (22/12-72).

convective activity occurring in its southwest-to-southerly currents. Note the accelerations of surface flow as air parcels move from the land to water surfaces and the presence of strong θ_e gradients behind the cold front (see Fig. 2.9c and 2.11c). The model appears to underpredict the southwestern portion of the surface trough over the continent(cf. Figs. 2.11a-c).

Of particular interest is that the weakest flow and little convective activity occur near the center of the simulated cyclone (see Fig. 2.11b,c). The simulated light winds at the cyclone center are consistent with those observed during the incipient stages of tropical cyclones (see Zehr 1992). An upper-air sounding, taken at the model cyclone center (See Fig. 2.12), shows a near -saturated conditions in the lowest 50 hPa and a deep dry atmosphere aloft. This suggests that the air near the cyclone center has been descending (or descended), which is qualitatively in agreement with that which occurred in tropical storms.(Anthes, 1982). (The near-saturated but dry-adiabatic boundary layer, which results from the parameterized surface fluxes and advection of heat and moisture, suggests the necessity to include a shallow convection scheme to remove the local conditional instability.) However, one may note from the BS81 analysis that stronger winds (>12 m s^{-1}) were placed near the cyclone center (Fig. 2.11a). The different wind speeds from the BS81 analysis could be again attributed to the lack of high-resolution observations, particularly over this region, which is far offshore. It is also possible that the observed intense winds result from convective-scale motions, as suggested by another strong ageostrophic wind report to the east of the low (see Fig. 2.11a).

By 23/00-84, The surface mesolow has deepened another 4 hPa to 1001 hPa (see Fig. 2.13a). Meanwhile, surface winds at some distance to the southeast of the cyclone center have increased to over 20 m s^{-1}, thus reaching "tropical storm" intensity (see BS81; Gray 1979; Burpee 1986). It is encouraging that the model reproduces very well the intensity and location of the surface cyclone. The error in the position of the surface mesolow is less than 200 km. This error is very small, considering that this is the 84th hour simulation of an MCS in a weak-gradient environment. It should be noted, however, that the center of the surface mesolow differs from that of the surface wind circulation (cf. Figs. 2.13b,c). The latter has frequently been used by mesoscale analysts to place the center of a surface low when reliable surface pressure observations were lacking, like in the present case (see Fig. 2.13a). Thus, the error in position is negligible when the closed wind circulation is compared to the BS81 analysis. In fact, as will be shown in Chapter 3, the surface mesolow tends to be driven by a vorticity center(i.e., the wind field). Similarly, the model reproduces the larger-scale pressure pattern as well as the surface temperature distribution both ahead of and behind the surface front. Because of the cyclonic development, the northern portion of the surface front exhibits overrunning of high-θ_e air, which is characteristic of warm-frontal circulation (Figs. 2.11 an 2.13). One may note, nonetheless, that the BS81 analysis shows the merging of the cold front with the surface cyclone and associated broad trough to the southwest, whereas our 900 hPa θ_e analysis still indicates separation of the two systems at this hour. On the other hand, the two analyses would be consistent when the frontal positions are all specified along the axes of the broad troughs. We believe that our analysis provides a

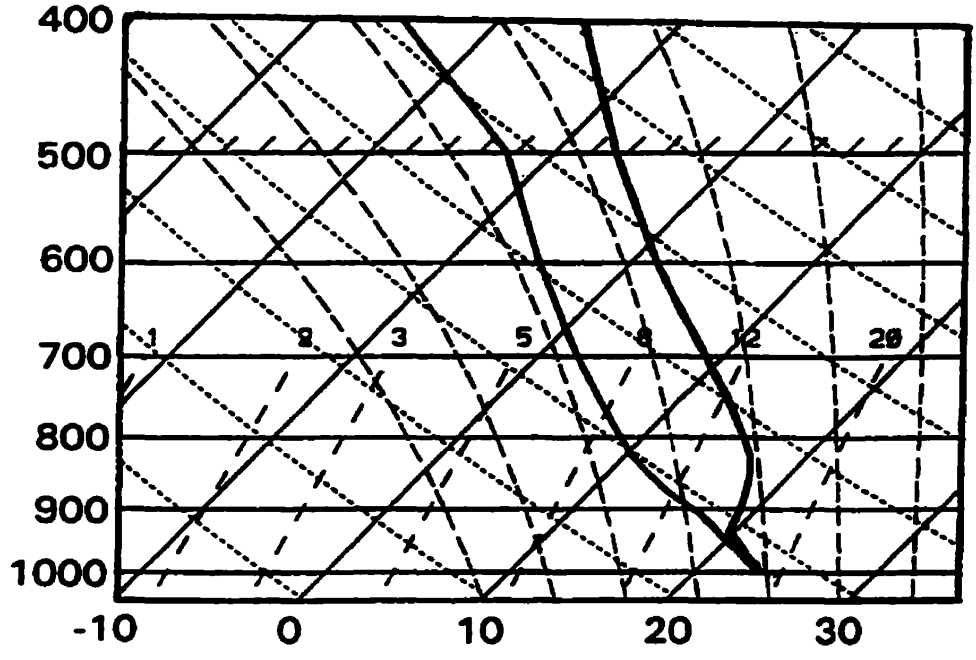

Fig. 2.12 Simulated upper-air sounding taken at the surface cyclone center at 22/12-72.

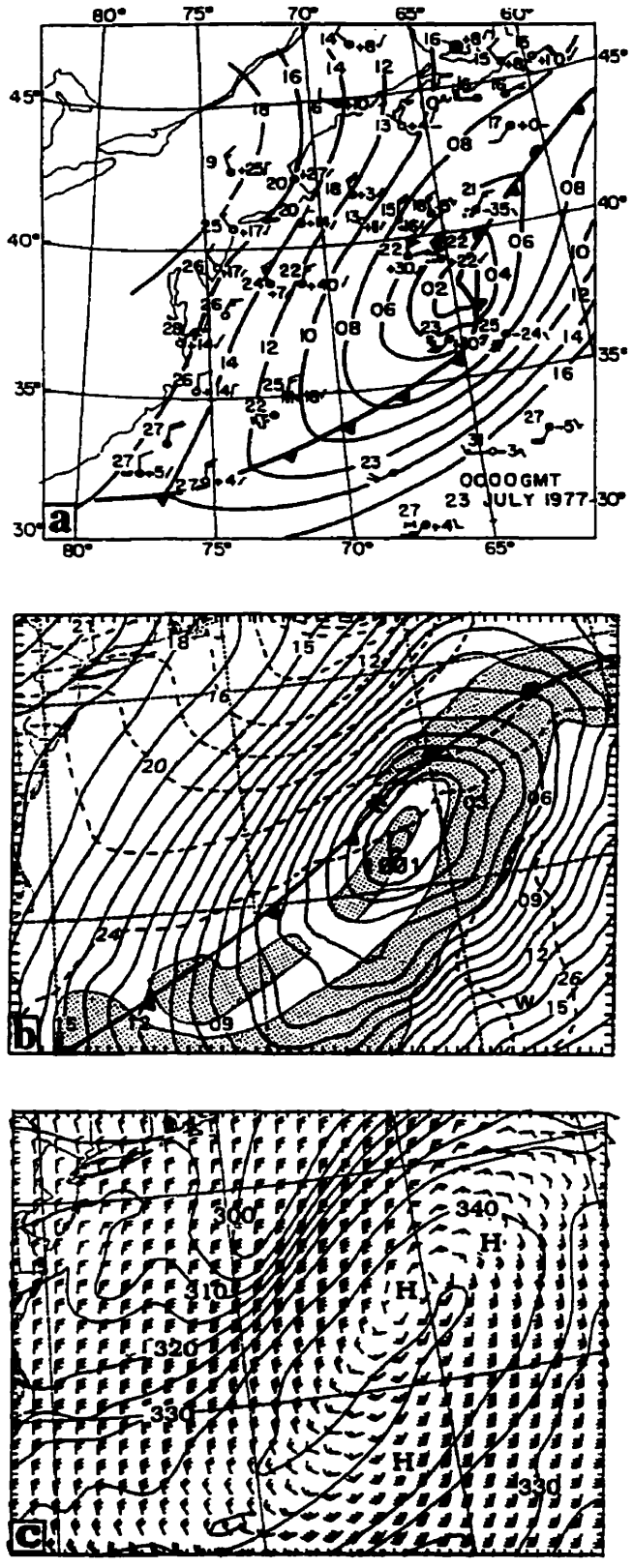

Fig. 2.13 As in Fig. 2.8 but for 0000 UTC 23 July 1977 and 84 h integration (23/00-84).

better depiction of the frontal position, since (i) there is a clear sign of strong θ_e gradients behind the front; and (ii) the broad trough ahead of the front is linked to the midlevel trough/vortex rather than the large-scale baroclinic trough, and it has been enhanced markedly by the development of the oceanic storm during the previous 24 h (see Figs. 2.9b, 2.11b, 2.13b, and 2.14).

It is also encouraging that the model reproduces the observed southerly and northerly surface jetlike flows with winds greater than 20 m s^{-1} symmetric about the cyclone center (see Fig. 2.13c). Associated with the two jetlike flows are the high- and low-θ_e tongues from different energy source regions. It is important to note from Figs. 2.9c, 2.11c, 2.13c how the high-θ_e air, resulted from the air-sea interaction (Emanuel 1986; Rotunno and Emanuel 1987), wraps around toward the cyclone center during the 24 h period. Because the high-θ_e tongue is closely related the convective development with intense upward motion (cf. Figs. 2.11b, c and 2.13b, c), its wrapping-around tends to occur in a slantwise fashion[7]. A similar wrapping-around scenario has also been noted by Ryan et al. (1992) in their analysis of a wide rainband associated with a developing tropical cyclone. In the present case, it can also be inferred from the low-level spiral cloudiness in the satellite imagery (e.g., Fig. 2.3e). By 23/00-84, the leading portion of the high-θ_e tongue has entered into the northerly return flow ahead of the cold front, thus forming a "comma-shaped" high-θ_e tongue.

[7] Note that the cyclonic-slantwise wrapping which is more significant along the convective band, is described herein in a volume-averaged sense due to the collective effects of deep convection (.i.e., upward motion) coupled with the cyclonic flow. In reality, air parcels embedded in (meso-γ-scale) convective updrafts or downdrafts tends to move more vertically than horizontally. Thus, this concept differs from that in a typical baroclinic system in which weak, stable ascent often occurs along frontal zones

This appearance of the tropical high-θ_e air in the northerly return flow further suggests that the frontal and the cyclone systems have not been merged at this stage. Likewise, the model simulates well the basic pattern of deep convection, particularly the "comma" head to the northeast of the cyclone (cf. Figs. 2.3f and 2.13b). A comparison of the satellite imagery with the BS81 analysis reveals that the cyclone center (i.e., the point, "o," in Fig. 2.3f) was located to the southwest of the "comma: head, that is , the region with low-level stratiform clouds. This further reveals the development of descending (or weak vertical) motion over the cyclone center, at least in the middle to upper troposphere, and provides an indirect validation of the sounding given in Fig. 2.12. The simulated cyclone center is also situated to the southwest of the "comma" head.

At this point, one may argue that the distributions of surface pressure and wind fields, as well as convective development relative to the cyclone, are no different than those in typical extratropical (baroclinically driven) cyclones. First, we have shown that the present cyclone develops in a weak-gradient, prefrontal environment(see Figs. 2.2 and 2.18). Second, we will see in Chapter 3 (Figs. 3.4-6) that the cyclone exhibits in the vertical little tilt and even negative wind shears above 950 hPa. Third, to examine whether or not the large-scale forcing would have any contribution to the cyclogenesis, a sensitivity simulation was conducted in which both the grid-scale latent heat release and the convective schemes were turned off *after the first 24 h integration* (experiment NLH), while keeping all the other model features identical to the control simulation (experiment CTL). In the absence of convective

forcing (see Fig. 2.14), an 84 h integration produces a large-scale frontal trough, superposed with the perturbation associated with the vortex/trough to the south due to the anticyclonic influence of the subtropical high. The minimum pressure of 1015 hPa is almost the same as that left behind by the previous MCSs at 20/12-24 (cf. Figs. 2.6 and 2.14); it is about 14 hPa weaker than the control simulated (cf. Figs. 2.13b and 2.14). Meanwhile, the simulated maritime boundary layer ahead of the front is a little colder than that in experiment CTL. These results reveal clearly that the large-scale baroclinic forcing makes small contributions to the deepening of the oceanic cyclone, and the genesis occurs primarily as a consequence of the convective forcing associated with the oceanic storm.

At the end of the 90 h control integration, that is , at 23/06-90, the surface cyclone experienced a further deepening to 998 hPa (Fig. 2.15). It continues to deepen thereafter as it propagates rapidly northeastward. After another 6 h, however, the cyclone center is displaced outside of the fine-mesh domain; so the integration for the purpose of the present study is terminated at this hour. This time appears to mark the merging of the surface front with the cyclone, since the θ_e pattern (not shown) becomes more linear with its peak values distributed along the major pressure trough axis. This merging gives rise to the analysis of a new surface front along the pressure trough that is mostly generated by deep convection along the oceanic storm. Thus, the large-scale baroclinic forcing begins to have more significant influence on the evolution of the oceanic storm hereafter.

The importance of the convective forcing during the previous 42 h (i.e., from 21/12-48 to 23/06-90) can be further seen by inspection the distribution and amount

of the model-produced rainfall with respect to the track of the surface cyclone. Figure 2.16 shows that the model produces widespread precipitation over most of the ocean area within the sub-domain, with considerable rainfall (>125mm) occurring to the south and much less to the north of the cyclone's track. This pattern is consistent with the continued development of deep convection south of 35°N and the weak frontal cloud activity (cf. Figs. 2.3c-f and 2.16). Of special interest is that in spite of the continued convective development, little stratiform precipitation is generated along the path of the oceanic storm. The stratiform rainfall that occurred to the north of the track is relatively small (<15mm) and associated with the lifting of high-θ_e air in the return flow along the "warm front." This result is in significant contrast to that which occurred within the continental MCSs, in which a substantial amount of stratiform precipitation (with a point maximum of 75mm) is produced (e.g., see Fig. 13 in Zhang et al. 1988b). This difference in the rainfall amount could be attributed to the different large-scale environments in which these two storms are embedded. Specifically, the continental MCSs are initiated in a near-saturated environment that was produced by the repeated formation of deep convection as the meso-α-scale short-wave trough and associated MCSs propagated from South Dakota toward Pennsylvania during a 3-day period (see BS81). By comparison, the oceanic storm develops in an environment under the long-period influence of the subtropical high so that the middle to upper troposphere are extremely dry. The maintenance of the

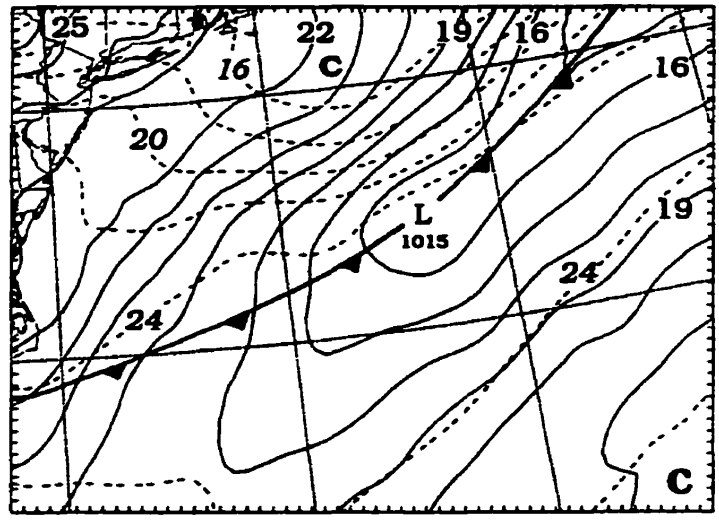

Fig. 2.14 As in Fig. 2.6 but for 84 h integration of experiment NLH (no latent heating).

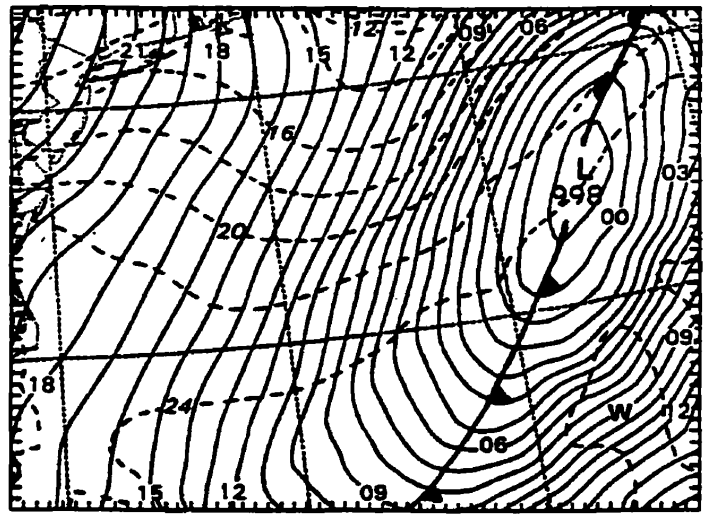

Fig. 2.15 As in Fig. 2.6 but from 90 h integration (23/06-90).

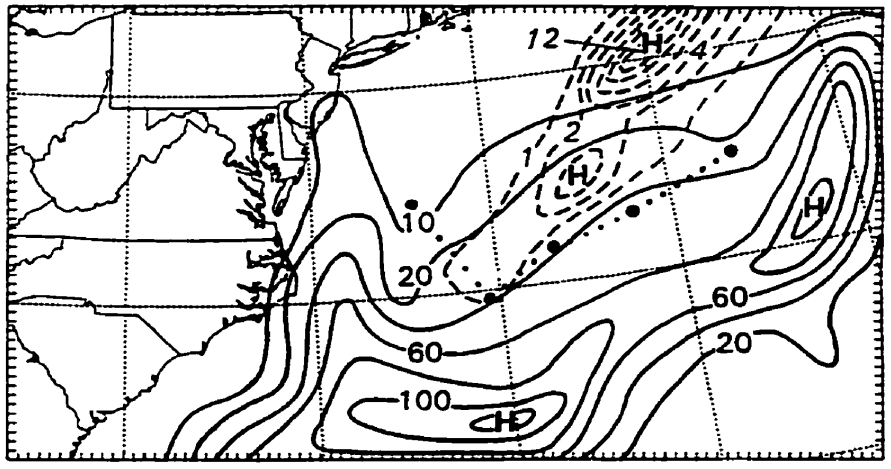

Fig. 2.16 The model-produced 42 h accumulated rainfall (mm) between 1200 UTC 21 and 0600 UTC 23 July 1977. Solid (dashed) lines are for convective (grid-scale) rainfall at intervals of 20 mm (2 mm) for the amounts larger than 20 mm (2 mm). Dotted line denotes the track of the surface cyclone center (see Fig. 2.1).

oceanic storm is primarily determined by the convective destabilization processes associated with the upward transfer of sensible and latent fluxes over the warm ocean, and their interactions with convectively generated circulation.

2.4 Evolution of midlevel flows

As shown by BS81, ZF86, and ZF87, the development of the continental MCSs is always accompanied by a midlevel meso-α-scale short-wave trough and its associated balanced vortex. This trough/vortex system also plays an important role in the organization of the oceanic storm, as will be discussed in the next section. In addition, a subtropical high to the south and a polar cold front from the north (see Fig. 2.2) appear to determine the movement of the cyclone/storm system. Thus, it is desirable to examine the structures and evolution of these larger-scale circulation in relation to the cyclogenesis over the ocean. For this purpose, Fig. 2.17 shows the evolution of the mesovortex, as represented by relative vorticity and wind vectors at 700 hPa, from 24, 60, and 84 h integration, whereas Fig. 2.18 displays the corresponding large-scale circulation. These three periods are chosen since they represent roughly the dissipated stage of the continental MCSs, and the incipient and mature stages of the oceanic cyclone/storm system.

The midlevel flow at 20/12-24 exhibits a closed vortex circulation with concentrated cyclonic vorticity at the end of the continental MCC's life cycle (Fig. 2.17a). An examination of the mass field reveals that this vortex is more or less in gradient balance with a midlevel short-wave trough (cf. Figs. 2.17a and 2.18a). Similar scenarios also occurred at the early stages of tropical cyclogenesis during

TEXMEX in which midlevel vortex circulation were collocated with the axes of easterly waves (see Emanuel et al. 1993). A comparison between Figs. 2.18a and 2.2a shows that the trough/vortex system has intensified appreciably as a result of the convective development over land. The low-level warm advection, though reduced considerably, still persists to the rear of the vortex/trough system. In contrast, the subtropical high has weakened slightly in intensity and shrunk in area coverage. Even so, the vortex/trough system is still embedded in the anticyclonic flow associated with the high. Thus, the vortex system tends to propagate southeastward into a tropical-like environment, that is, with much weaker gradients (see Figs. 2.6-2.9). In the meantime, the developing baroclinic wave with strong thermal gradients is fast approaching from the northwest.

At 22/00-60, that is, 42 h after the dissipation of the continental MCC, the mesovortex is still well maintained in the absence of other convective forcing(Fig. 2.17b); but its intensity has weakened somewhat due partly to the application of numerical diffusion and partly to the influence of (weak) larger-scale deformational flow. These diffusive effects result in an area expansion of the vortex circulation (cf. Figs. 2.17a,b). Fritsch et al. (1994) have also noted an increase of the vortex scale after each life cycle of the MCS they analyzed. It is of interest to note that the surface cyclogenesis occurs at 150-180 km to the southeast of the vortex center (see Fig. 2.1 and cf. Figs. 2.9b and 2.17b), a feature that has been observed during TEXMEX(Emanuel et al. 1993). The tracks of the two systems tend to depart further hereafter (see Fig. 2.1). It is also of interest to note that as the vortex/trough system

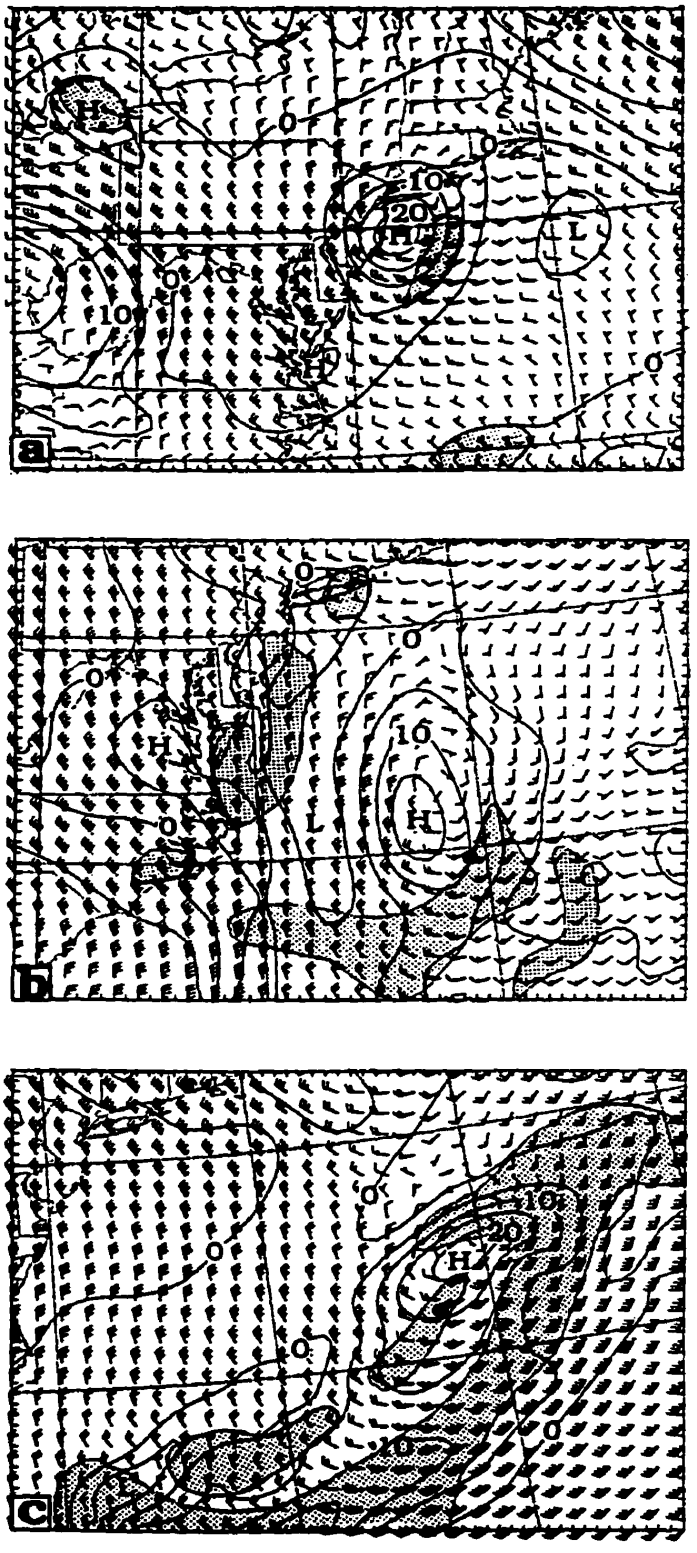

Fig. 2.17 Horizontal maps of simulated 700-hPa winds plotted at every other grid point and vertical relative vorticity at intervals of 5×10^{-5} s^{-1} at (a) 20/12-24, (b) 22/00-60, and (c) 23/00-84. A full wind barb is 5 m s^{-1}. Solid circle denotes the surface cyclone center. Shading shows the precipitation distribution of the oceanic storm.

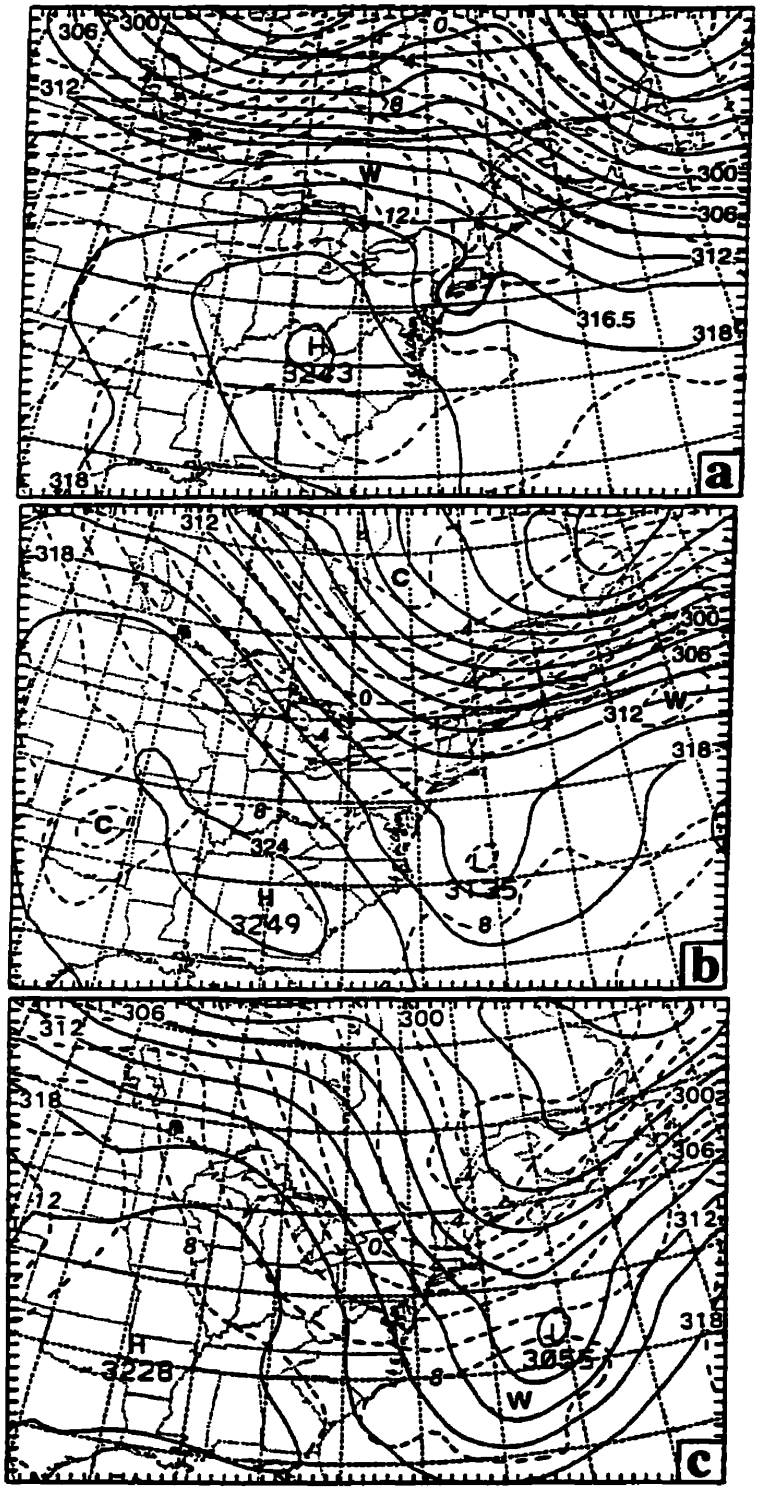

Fig. 2.18 As in Fig. 2.2 but from the simulations at (a) 20/12-24, (b) 22/00-60, and (c) 23/00-84.

moves southeastward, surface pressure gradients to the southeast are intensifying with time, as mentioned before, whereas they are weakening right beneath the midlevel vortex (cf. Figs. 2.17b, 2.7b, 2.8b, and 2.9b). While dispersion of warm air away from the vortex columns could account for the continued weakening of the surface trough, we may consider the process given below as an alternative explanation for the phenomenon. Just imagine what would happen with surface isobars when a vertically coherent lower-pressure column is forced to move away from the eastwardly propagation baroclinic system to the north into the slowly evolving subtropical high to the southeast (see Figs. 2.2 and 2.18). This will cause an increase in the surface pressure gradient and thus the surface flow ahead, but a decrease in them in the wake. This scenario appears to reflect the important characteristics of the weak-gradient flows and the vertically coherent thermal structure of the vortex/trough system during its southeastward movement. The weak surface pressure gradients could clearly provide a favorable condition for the organization of cyclonic flow when cyclonic vorticity is locally generated or advected into the region. This is because little pressure gradient force will be imposed on the parcels changing directions along their trajectories.

During the previous 36 h period, there have been some important changes in the large-scale circulation. Specifically, the areal coverage of the subtropical high has decreased substantially as it drifts westward to the south of the approaching baroclinic wave (Fig. 2.18b). These evolutionary features of the subtropical high conform well to the NMC analysis (not shown). By comparison, the short-wave trough propagates

southeastward to lower latitudes, but with little change in intensity. More significantly, the trough axis has shifted from its southwest-northeast orientation to south-north, so the vortex system looks like it is attached to the large-scale trough to the north instead of being superposed on the subtropical ridge at earlier times (cf. Figs. 2.2a and 2.18b). This shift appears to explain why the storm change its direction of movement from southeastward to northeastward around 22/00-60 (see Fig. 2.1). It is evident that the mesovortex, after moving to the warm Gulf Stream water, is embedded in an environment with the thermal gradient much weaker than that which ever occurred before (cf. Fig. 2.2a and 2.18a, b). This indicates that the ensuing surface cyclogenesis takes place in a more barotropic environment with weak thermal advection or weak influence, if at all, from the baroclinic wave to the north, even at 850 hPa (not shown). This can be further seen from the propagation of a warm tongue (or thermal ridge) to the north of the vortex, that is advected through by the westerly flow from eastern Ontario at 20/12-24 to the south of Newfoundland at this hour, as indicated by the letter, "W," in Figs. 2.18a,b.

By 23/00-84, the short-wave trough has deepened 80 m during the previous 24 h period (see Fig. 2.18c). Associated with the mass deficit is the amplification of the midlevel mesovortex (as a result of the vortex stretching and advection, see Fig. 2.17c). Furthermore, the southwesterly wind speeds ahead of the trough axis have more than doubled, and the influence of the intense flow has spread over a much greater area in the southeastern quadrant due to the continued convective development. Of particular importance is that the vortex center is always located in

the wake of the continental and oceanic storms (see Figs. 3-5 in ZF87 and Figs. 2.17a-c herein). This region appears to be a favorable location for the maintenance of a vortex, since the convective storms behave like an "obstacle" to its environmental flows such that the vortex could be protected from being rapidly sheared off. It should be pointed out that this convection-vortex juxtaposition differs from the warm-core vortex/MCSs case of July 1982 documented by Fritsch et al. (1994), in which deep convection repeatedly developed near the vortex center, rather than at the edge of vortex circulation. The vertical structure of the vortex circulation will be presented in Chapter 3.

2.5 Initiation and organization of the oceanic storm

In this section, we attempt to clarify how the oceanic storm is initiated near the North Carolina coast around 21/00-36 and then organized at 22/00-60 as the convectively generated perturbations move offshore (see Figs. 2.3, 2.7-2.9). To isolate the roles of the mesoscale perturbations in initiating and organizing the oceanic storm , we feel it more appropriate to examine mesoscale flow structures without the influence of diabatic heating (after first 24 h integration), that is, through the analysis of experiment NLH. Without deep convection, the model atmospheric circulation will be dominated by the large-scale flows and mesoscale disturbances left behind by the dissipated MCC (e.g., cold outflows, surface pressure perturbations, and the vortex/trough) interacting with topography, land-ocean contrasts, and surface fluxes.

Figure 2.19 shows the distribution of sea level pressure, temperature, horizontal flow, and divergence at σ=0.873 from 24 h NLH integration. At the end of the continental MCC's life cycle, we see a pool of cold air centered over New Jersey, which tilts downward toward the surface trough (Fig. 2.19a). Associated with the cold pool is an area of divergence, surrounded by a broad cyclonic flow with weak convergence. As will be shown in Chapter 3, this broad cyclonic flow/cold pool is part of the mesovortex circulation. The convective line, "D," shown in Fig. 2.6, occurs just slightly behind the leading edge of the cold pool as a result of the lifting of high-θ_e air ahead. Over the land, the leading cold air has propagated rapidly into central North Carolina at the lee side of the Appalachians. This portion of cold outflow does not cause any development of new convection during the morning hours in spite of a favorable convergence zone behind the leading edge (Fig. 2.19b). This is consistent with the analyses of H78 (see Fig. 2.4) and BS81 (see their Fig. 9), since this region is conditionally stable (Fig. 2.19a) and since the major dynamic forcing (i.e., organized mass convergence) is still associated with the midlevel short-wave trough/vortex (cf. Figs. 2.18a and 2.19b). It should be noted, though, that the divergence/convergence patterns in the vicinity of the Appalachians have been influenced by the topography, such as the divergence zone over West Virginia and part of the convergence downstream; but the orographic effects are relatively small offshore.

At 21/00-36, the main cold pool and the associated divergence have moved offshore (see Fig. 2.20). In contrast, the portion of cold downdraft air mass over the

land diminishes rapidly as the daytime PBL develops, and after a diurnal cycle a warm pocket appears in the lee of the Appalachians. Obviously, the continental warm air now begins to overrun the maritime cold pool in the presence of the meso-α-scale cyclonic flow, namely, potential temperature θ tilts upward along the current. This results in favorable convergence and upward lifting over the coastal region. Since this region is also distributed with conditional instability, the convective development should occur as expected (cf. Figs. 2.20b and 2.7b). On the other hand, the favorable convergence at the southern periphery of the cold pool/vortex persists during the previous 12h(see Figs. 2.19b and 2.20b) While deep convection fails to develop over the convergence zone, the continuous upward lifting of high-θ_e air in the maritime boundary layer may help condition the prestorm environment for the subsequent eastward expansion of the new convection. It follows that the new convective system at the North Carolina coast, shown in Fig. 2.3b, is initiated at the southern periphery of the mesovortex as a consequence of the cyclonic circulation interacting with the land-ocean thermal contrasts during the afternoon hours. When the surface diurnal heating cycle was turned off after the 24 h integration, the model was unable to reproduce deep convection along the coast at 21/00-36 (not shown).

The organization of the new convection into the oceanic storm certainly depend on whether or not there are (i) a continued supply of convective available potential energy (CAPE) and (ii) a mesoscale forcing mechanism to persistently focus the CAPE such that the centralized convective heating, interacting with the surface fluxes over the warm Gulf Stream water, can result in a highly organized MCS. As

mentioned previously, surface pressure gradients and winds ahead of the trough axis in experiment CTL intensify rapidly as the mesovortex moves southeastward under the influence of the subtropical high (cf. Figs. 2.6-2.9 and 2.17-2.18). Similar scenarios occur more or less in experiment NLH (cf. Figs. 2.19a 2.20a, and 2.21a), except that the model is unable to reproduce a surface mesolow and very weak pressure gradients beneath the vortex (due to the presence of vertically less coherent thermal structures). Nonetheless, a favorable and persistent mesoscale forcing is evident ahead of the trough axis , even in the absence of deep convection (see Figs. 2.19-2.21). The significance of the trough/vortex in organizing the oceanic storm can be further seen by comparing Figs. 2.21a,b and 2.9b, which show that the southwest-northeast elongated boundary layer convergence and conditionally unstable zone in experiment NLH resembles so well the distribution of the simulated convective band at 22/00-60.

The next issue is the source of high θ_e air and its transport into the region of release. As shown in Fig. 2.21, the low-level jetlike flow, resulting from the increased pressure gradients, generates a warm tongue in the southwesterly flow due partly to the upward sensible heat flux from the warm water, and partly to the warm advection from the heated PBL over the land (cf. Figs. 2.20a and 2.21a) and from the lower latitudes where ample high-θ_e air is available. Note that the large-scale warm advection decreases rapidly with height and it almost vanishes at 700 hPa(see Fig. 2.18b). Since the ambient winds exhibit negative vertical shear above 950 hPa (see Fig. 3.4 in Chapter 3), this thermal structure due to differential thermal advection and

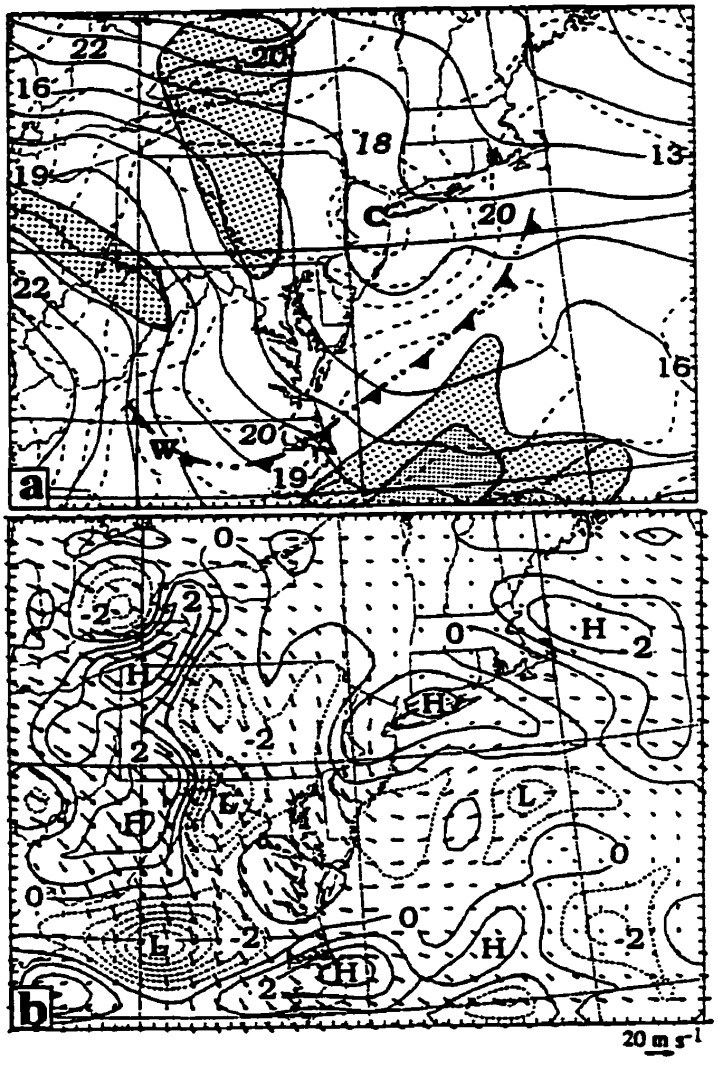

Fig. 2.19 (a) Sea level pressure (solid, every 1 hPa), superposed with temperature (dashed, every 1°C) at $\sigma = 0.873$ (i.e., about 85 hPa above the surface) from 24 h integration of experiment NLH. Letters "W," and "C," denote warm air and cold air, respectively. Frontal symbols alternated with double dots indicate cold outflow boundaries. Coarse (dense) shading shows the distribution of $\Delta\theta_e$ between $\sigma = 0.647$ and 0.929 (roughly with $\Delta p = 265$ hPa), i.e., less than -20 (-25) K. (b) Horizontal divergence (positive/solid, negative/dashed) at $\sigma = 0.873$ at intervals of 10^{-5} s^{-1}, superposed with wind vectors.

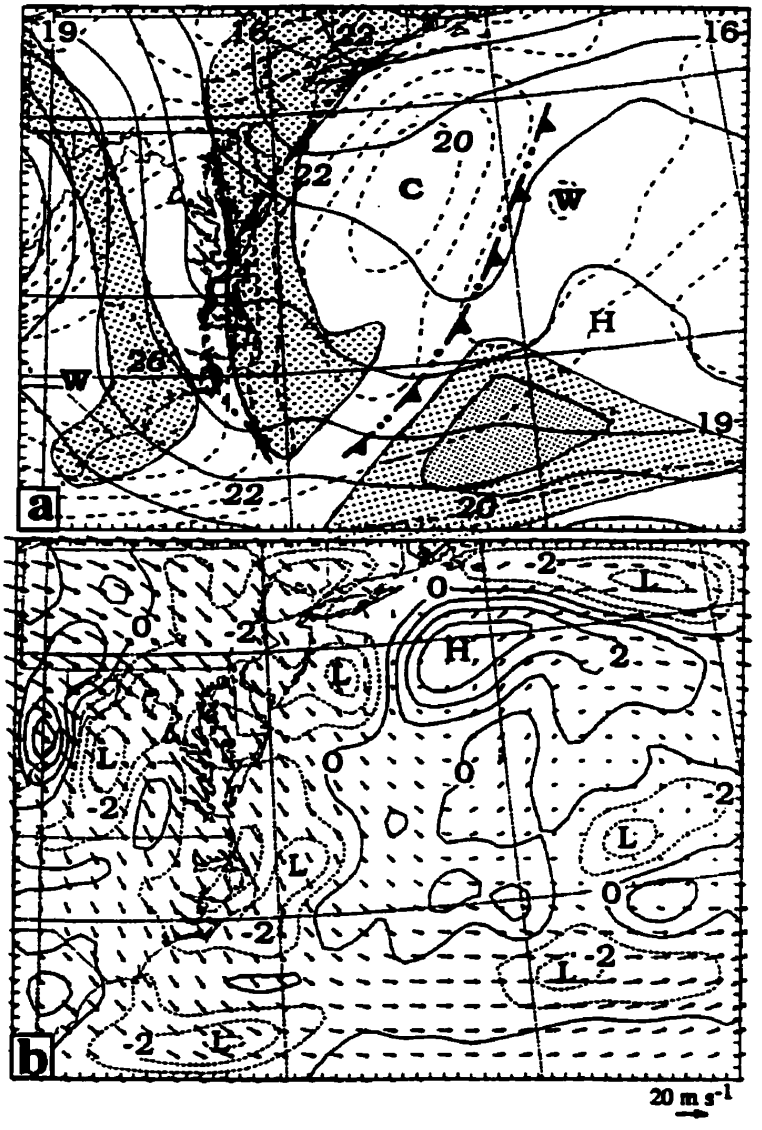

Fig. 2.20 As in Fig. 2.19 but at $\sigma = 0.929$ (about 60 hPa above the surface) from 36 h integration of experiment NLH.

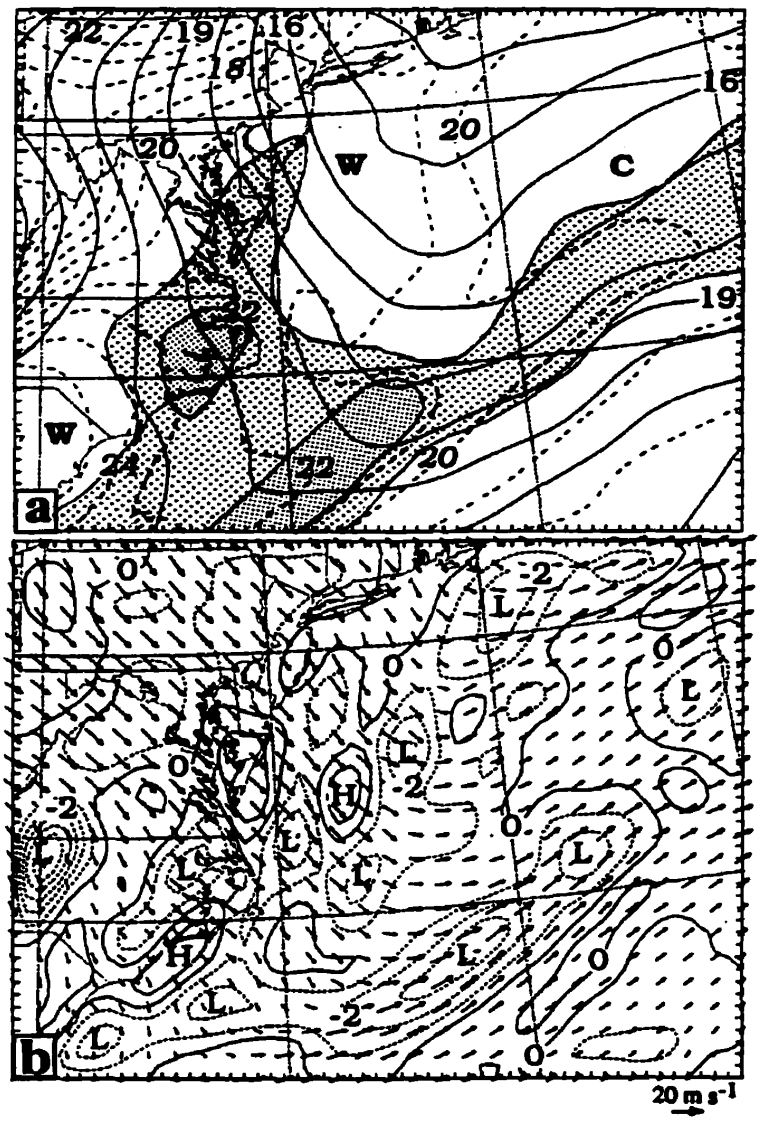

Fig. 2.21 As in Fig. 2.19 but at $\sigma = 0.929$ (about 60 hPa above the surface) from 60 h integration NLH.

surface fluxes tends to destabilize atmospheric columns along the way. This is evidenced from Fig. 2.21a, which displays an extensive area of conditional instability in the southwesterly flow. This trend persists at least for the subsequent 30 h (not shown). Therefore, we may state that the persistent forcing from the inertially stable trough/vortex system, the low-level warm advection over the mid-Atlantic states and the steady CAPE supply (through upward surface fluxes) from the tropic ocean account for the continued development and organization of the oceanic storm (see Figs. 2.6-2.9), and determine the predictability of the storm/cyclone system beyond 2.5 days. It is evident that when deep convective effects are included, the CAPE supply from the tropic ocean will be more pronounced. This will be shown in the context of heat budgets in Chapter 3. It should be noted, though, that the weak surface drag is also an important parameter in assisting the convective development through generation of stronger surface cyclonic flows and enhanced surface fluxes. The above statement is confirmed by a sensitivity simulation, in which the ocean surface characteristics are replaced by typical land conditions. In this simulation the model reproduces reasonably well the continued convective development but fails to generate the surface cyclone (not shown).

2.6 Summary and conclusions

In this chapter, a 90 h real-data simulation has been carried out. Comparison of the simulation results with BS81 and satellite observations demonstrated the capabilities of the model in reproducing much of the meso-β -scale structure and evolution of the long-lived MCSs out to 90 h. These include (i) the dissipation of the

MCC and the weakening of the surface mesolow to a mesotrough as they move away from the state of Pennsylvania; (ii) the timing and location of the initiation of a new MCS at 36 h integration and the genesis of a surface mesolow at the south periphery of the previous trough/vortex system over the warm Gulf Stream water after 60 h into the integration; (iii) the subsequent track and deepening of the surface cyclone; (iv) the orientation and area coverage of the oceanic storm with respect to the surface cyclone; (v) the development of tropical-storm-like surface winds; (vi) the maintenance of the mesovortex/trough system; (vii) the westward retreat and weakening of a subtropical high, and (viii) the propagation of a large-scale cold front and a midlevel baroclinic wave in relation to the oceanic storm/cyclone system.

It is found that the new MCS is initiated at the southern periphery of the mesovortex at 21/00-36, after the vortex/cold-pool moved offshore and interacted with the land-ocean thermal boundaries during the afternoon hours. Meanwhile, as the surface trough advances toward the warm Gulf Stream water at lower latitudes under the influence of the subtropical high, it weakens but the pressure gradients ahead of the trough axis and the associated southwesterly flow intensify with time. The intensifying flow helps to enhance the mesoscale convergence in the PBL and organize the deep convection into the oceanic storm at the southern periphery of the previously dissipated MCC. Furthermore, the intensifying flow tends to (i) "pump" up sensible and latent heat fluxes from the warm ocean surface, and (ii) transport the tropical higher-θ_e air in a cyclonic-slantwise fashion into the region having lower-θ_e aloft, so as to produce further conditional instability, enhanced deep convection and

increased cyclonic deepening. These processes, enhanced by mesoscale ascent, appear to be responsible for the wrapping-around of high-θ_e air and the development of "comma-shaped" deep convection during the mature stage of the storm. The mesovortex plays an important part in assisting the initiation and organization of the oceanic storm and its associated flow structures.

The roles of deep convection versus large-scale forcing in the oceanic cyclogenesis have been investigated. It is shown that the oceanic cyclone/storm system develops within a prefrontal, near-barotropic environment. The subtropical high helps steer the propagation of the vortex/trough system prior to 22/00-60, whereas the large-scale baroclinic wave to the north plays a role in determining the movement of the cyclone/storm system and its intensity near the end of the 90 h integration. In the absence of deep convection, an 84 h sensitivity simulation produces only a surface trough with its minimum pressure being nearly the same as that left behind by the previous MCSs at 20/12-24. It is found that cyclogenesis begins between 21/12-48 and 22/00-60 at 150-180 km to the southeast of the vortex/trough, with the surface mesolow hugged by the oceanic storm. The oceanic cyclone, once initiated, spins up rapidly and overpowers the low-level portion of the vortex/trough circulation to deepen 14 hPa in 24h. The genesis is shown to be driven entirely by the parameterized deep convection along the oceanic storm with little contribution from grid-scale precipitation. Therefore, we may conclude that the oceanic cyclogenesis in the present case is *induced by the continental MCS/vortex system at its southern periphery*, after it moved into the warm Gulf Stream water, and

then it is ***driven by deep convection associated with the oceanic storm*** in the southwest-to-southerly flow of tropical high-θ_e air.

Chapter 3

Oceanic cyclogenesis as induced by a mesoscale convective system moving offshore: genesis and thermodynamic transformation

3.1 Introduction

Based on the simulation presented in Chapter 2, we wish to address two key issues to the understanding of oceanic cyclogenesis as induced by an MCS and then driven by deep convection. They are (i) What mechanisms are responsible for the transformation of an MCS with a deep cold pool in the lower troposphere into an intense mesocyclone that is characterized by a deep warm-cored structure? and (ii) What processes determine the amplification of lower-level cyclonic vorticity in tropical storms in relation to the convectively generated midlevel mesovortex from the previously dissipated MCS?

To our knowledge, the above two issues have not been properly addressed in the previous studies owing to the limited observations over vast data-void oceans (see the recent review by Zehr 1992). For example, Davidson et al. (1990) and Mapes and Houze (1993) suggested that the transformation of MCSs into tropical storms may occur when some portion of cyclonic vorticity associated with the midlevel mesovortex descends to the surface and then amplifies through vortex stretching in the presence of intensifying low-level inflows along convective bands. However, in

their analyses of cases of tropical cyclogenesis during TEXMEX, Emanuel et al. (1993) found the concentration of low-level high cyclonic vorticity in lines or arcs along gust fronts far away from the location of the midlevel mesovortex with a cold core in the lower troposphere. They proposed a conceptual model with the low-level cold pool near the vortex core being reheated and moistened by surface fluxes over the warm ocean to generate a warm-core anomaly and new convection near the circulation center.

The organization of this chapter is as follows. The next section documents the evolution of cyclonic vorticity associated with the oceanic cyclone/storm system. In section 3.3, the characteristics of the vertical structures associated with the long-lived MCS at different stages of its life-cycle are examined. The vorticity, potential temperature and equivalent potential temperature budget calculations are given in sections 3.4 and 3.5. Summary and concluding remarks are given in section 3.6.

3.2 Evolution of low-level cyclonic vorticity

In this section, we use the control simulation presented in Chapter 2 to diagnose the horizontal structures and evolution of the cyclonic vorticity associated with the oceanic cyclone/storm system, and in the next section we examine the relationships between the cyclone's vorticity and the midlevel mesovortex generated by the continental MCSs. For the convenience of later discussions, some selected surface maps of the MCS/cyclone development are given in Fig. 3.1, which are taken from 24-, 60-, 72-, and 84 h simulations, valid at 1200 UTC 20, 0000 and 1200 UTC 22, and 0000 UTC 23 July 1977 (henceforth 20/12-24, 22/00-60, 22/12-72, and

23/00-84), respectively. These four periods are chosen since they represent roughly the dissipated stage of the continental MCC, and the incipient, intensifying and mature stages of the oceanic cyclone/storm (or convective band).

Figures 3.2a-f show the 6 h evolution of vertical relative vorticity, superposed with (ground relative) wind vectors, at 950 hPa from 60 to 90 h integration during which time more rapid deepening occurs (see Fig. 3.1). The 950 hPa level is presented because this is roughly the level at which the flow intensity and vorticity production in the cyclone/storm system are maximized. At 22/00-60, the 950 hPa mesoscale flow is generally similar to but stronger than that at the surface (cf. Fig. 2.9c in Chapter 2 and Fig. 3.2a herein), showing a broad cyclonic circulation associated with the mesovortex/trough superposed on the westerly flow. A localized vorticity center, as marked by a cross in Fig. 3.2a, appears at the central portion of the weak-flow region to the north of the surface mesolow, which represents the intensity of the mesovortex in the lower troposphere (i.e., the surface mesotrough). Of our concern here is the development of two concentrated vorticity (V) bands each with a width of 120-180 km (based on their greater than f magnitudes): one distributed parallel to but lagged slightly behind the convective band with its peak value close to the surface mesolow (at 150-180 km to the south of the midlevel mesovortex) and the other originating from the northeastern portion of the surface front. Because of their relations to the convective band and the large-scale front, these two V-bands could be regarded as being convectively and baroclinically driven, respectively, although the latter is persistently enhanced by deep convection ahead of the front. It

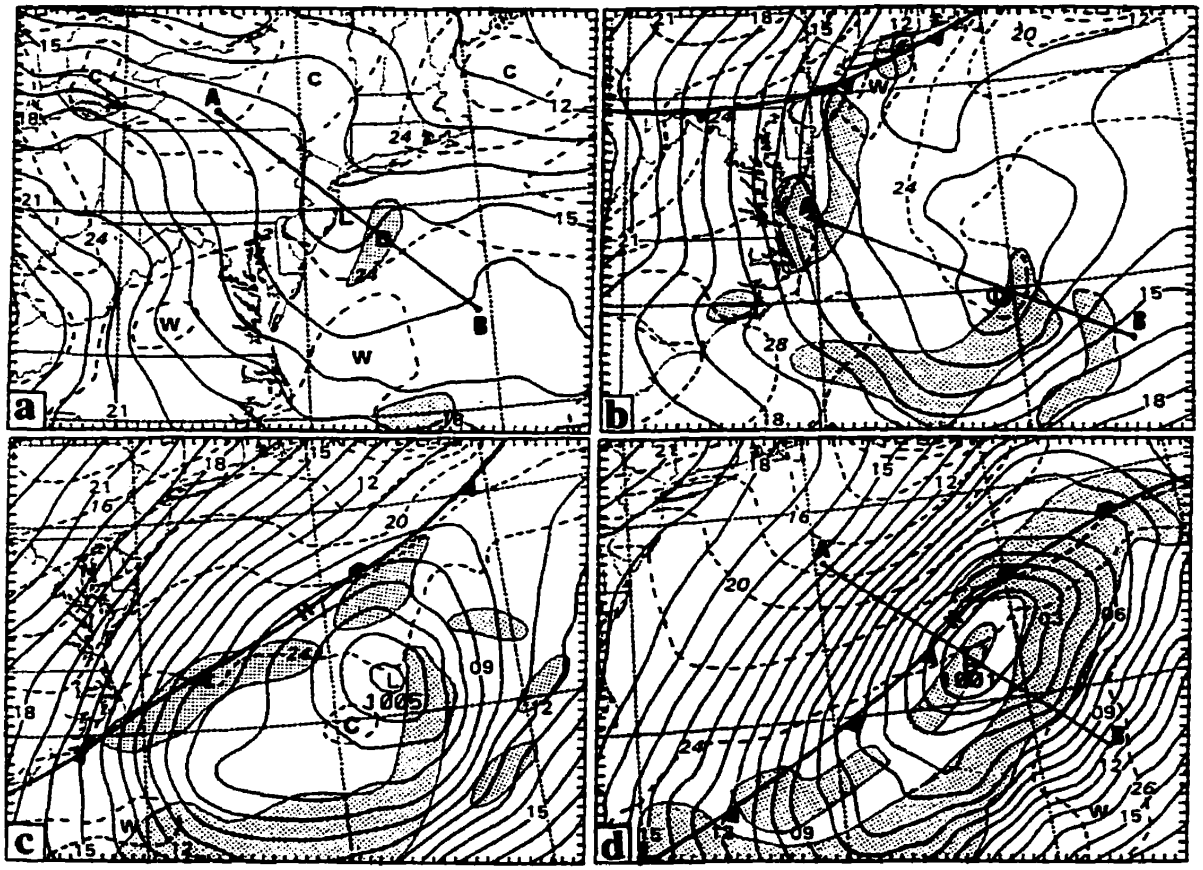

Fig. 3.1 Simulated sea level pressure (solid, every 1 hPa), labeled as an excess over 1000 hPa, e.g., 06--1006 hPa, and surface temperature (dashed, every 2°C) at (a) 20/12-24; (b) 22/00-60; (c) 22/12-72; and (d) 23/00-84. Lines *AB* indicate location of cross sections used in subsequent figures. shadings denote the area of simulated deep convection. The intervals marked on the frame are mesh grids (25 km for fine mesh; similarly in the rest of figures). Letters "L," "W," "C," denote the centers of the surface cyclone, warm and cold air, respectively.

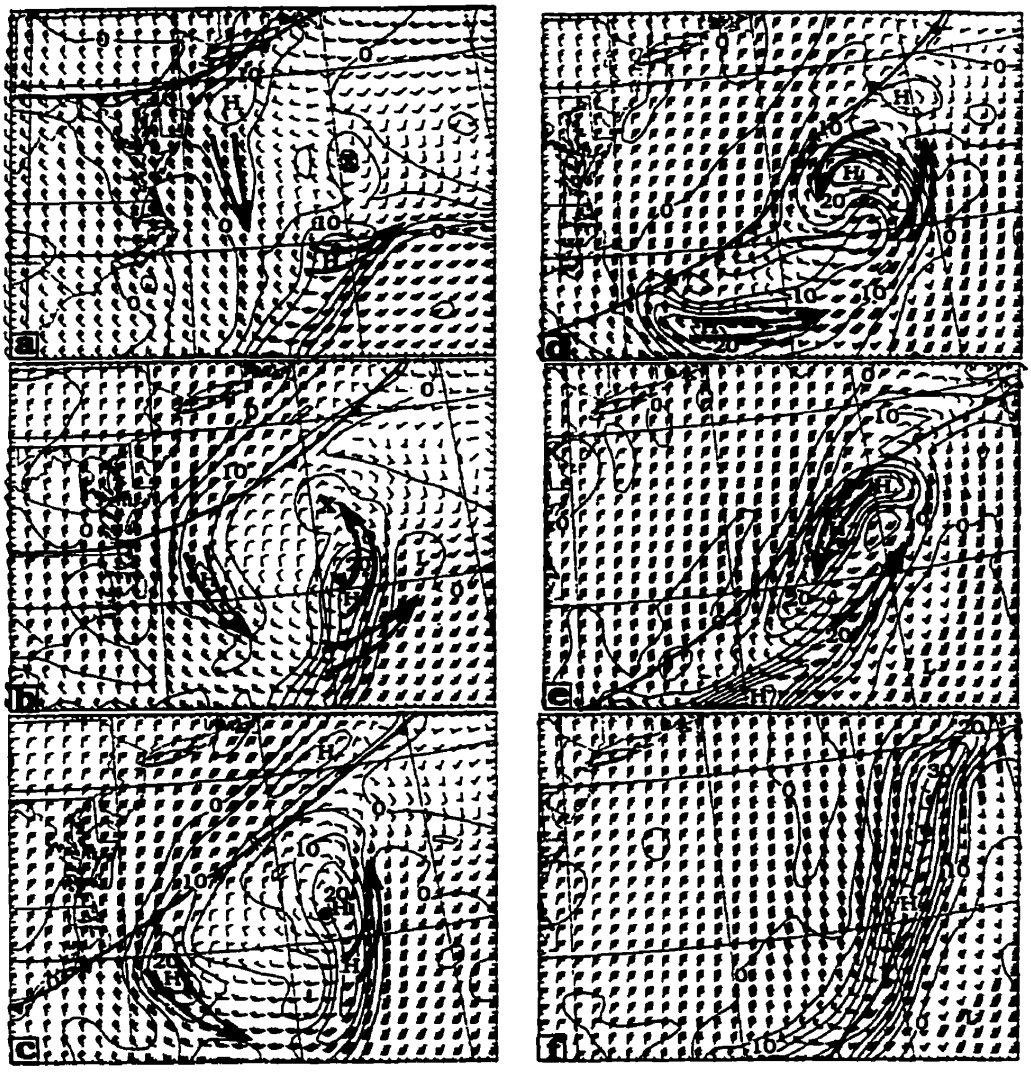

Fig. 3.2 Horizontal maps of vertical relative vorticity at 950 at intervals of 5×10^{-5} s^{-1} superposed with horizontal winds plotted at every other grid point at (a) 22/00-60, (b) 22/06-66, (c) 22/12-72, (d) 22/18-78, (e) 23/00-84, and (f) 23/06-90. Winds plotted according to convention with each pennant, full barb, and half barb denoting 25, 5, and 2.5 m s^{-1}, respectively. Large arrows indicate the direction of propagation of the vorticity centers. Solid circle denotes the center of the surface cyclone. The surface frontal position, based on the evolution of θ_e, is given (see Chapter 2). The symbol "X" shows the part of relative vorticity associated with the mesovortex.

is evident that the baroclinic *V*-band consists mostly of shear vorticity, whereas the convective *V*-band contains both shear and curvature vorticity associated with the convectively enhanced broad surface trough (cf. Figs. 3.2a and 3.1b). Such high *V*-bands have also been observed during TEXMEX in association with gust fronts at some distance from midlevel mesovortices (see Emanuel et al. 1993). We will see below that these two *V*-bands tend to wrap around into the cyclone center in a slantwise fashion similar to the high-θ_e tongue presented in Chapter 2 (see Figs. 2.11c and 2.13c therein), as indicated by large arrows in Figs. 3.2a-f, and they appear to determine the evolution and intensification of the surface cyclone.

Six hours later (i.e., at 22/06-66), the larger-scale background flow becomes better organized (Fig. 3.2b) as the surface cyclone deepens. The two *V*-bands are also amplifying as they are displaced cyclonically toward the cyclone center where weak flows are prevailing (cf. Figs. 3.1b and 3.2a,b). A closed wind circulation with increased curvature vorticity begins to form near the center. Of interest is that *the developing cyclone absorbs gradually and overpowers the lower-level circulation of the mesovortex* as the convective *V*-band propagates into the weak-flow region (cf. Figs. 3.2a-c). Vorticity budgets, as shown in Fig. 3.8, reveal that stretching due to convergence in the planetary boundary layer (PBL) contributes the most to the amplification of the two *V*-bands. Hence, the cyclonic vorticity is primarily generated through vortex stretching along the *V*-bands, and then advected cyclonically toward the cyclone center in a slantwise fashion, causing the intensification of the cyclone.

By 22/12-72, an organized mesovortex has formed at 950 hPa as the surface cyclone becomes well developed ahead of the large-scale cold front (cf. Figs. 3.1c and 3.2c). Over the vortex center, the relative vorticity, which was less than $0.5f$ 12 h earlier, has tripled to more than $2f$. Meanwhile, the cyclonic vorticity in the storm's northwestern quadrant has increased. Of particular importance is the development of a "comma-shaped" vorticity structure, in which the "comma" head contains mostly curvature vorticity while its tail consists of shear vorticity. This "comma" head forms as the local vorticity maximum moves into the weak-flow area (cf. Figs. 3.1b,c and 3.2b,c). These vortex features, including the associated wind, pressure and precipitation structures, are very similar to the comma vortex described by Tuleya and Kurihara (1984) in their simulation of tropical cyclogenesis. Their results also show that the comma vortex forms as a consequence of the vortex stretching along a convective band and advection into the cyclone center. This suggests that the continued deep convection along the oceanic storm is crucial in the formation of the comma vortex and the deepening of the surface cyclone (cf. Figs. 3.2 and 3.3). In other words, *the vortex/cyclone system deepens as the convectively generated shear vorticity (through stretching) is advected inward and converted to curvature vorticity,* at least during the cyclone's incipient stages. The significant advective effects are understandable, when considering the relatively weak vertical motion or convergence near the cyclone center (see Figs. 3.4 and 3.5).

At 22/18-78, the main portion of the baroclinic *V*-band has moved into the convective band ahead of the cold front. It has traveled at a speed of 10-12 m s^{-1}

during the previous 18 h, which is about 65% of the average wind speed at the local vorticity center (Fig. 3.2d). The merging of this *V*-band into the convective *V*-band leaves behind very weak cyclonic vorticity along the southwest-northeast-oriented cold front, consistent with the analysis of little wind shift across the surface front by BS81. By comparison, the major portion of the convective *V*-band has been wrapped around into the circulation (but not the low pressure) center with much less vorticity left in the tail of the comma vortex. As a result, an intense cyclonic circulation with strong winds develops in the vicinity of the vortex center (cf. Figs. 3.2a-d). Note that the wrapping-around of the two *V*-bands as well as the high-θ_e tongue appears to "block" the large-scale flow and distort the frontal zone. For example, the flow behind the cold front changes its direction from north-north-westerly at 60 h to near-northerly at 66 h, northeasterly at 72 h, and north-northeasterly at 78 h (see Figs. 3.2a-d). This blocking appears to help explain why the surface cold front slows after it moved over the ocean.

By 23/00-84, the cyclonic wrapping-around has advected the leading portion of the convective *V*-band into the northerly flow, as occurred with the 900 hPa high-θ_e tongue (cf. Fig. 2.13c in Chapter 2 and Fig. 3.2e herein). It is apparent that the wrapping-around of both the *V*-bands and the high-θ_e air is highly asymmetric, and it occurs slightly faster than the propagation of deep convection along the low-level jetlike current. In contrast, the baroclinic *V*-band has moved completely into the southwesterly flow and merged with the convective *V*-band , resulting in the rapid growth of cyclonic vorticity along the oceanic storm; its peak intensity has increased

to over 4*f*. Note that this portion of *V*-band coincides with the broad trough ahead of the cold front, whereas the concentrated vorticity in the northerly flow (>3*f*) corresponds to the "oval-shaped" surface isobars with its peak located slightly ahead of the surface mesolow (cf. Figs. 3.2e and 3.1d). Note also that the closed wind circulation always leads the surface mesolow (see Fig. 3.2a-e), indicating *the important role of the vorticity concentration in driving the propagation and intensification of the oceanic cyclone.* Of interest is that the intense vorticity concentration in the northerly flow tends to be sheared away as the frontal circulation begins to dominate the cyclone's flow structure (cf. Figs. 3.2d-f). In fact, the lateral dimension of the peak vorticity zone has already decreased and more curvature vorticity has been converted to shear vorticity during the previous 6 h (cf. Figs. 3.2d,e). Hence, the comma vortex begins to transform into a linear vortex band hereafter.

At the end of the 90 h integration, the cold front has merged with the surface cyclone, causing the collapse of the wrapping-around process and the development of an elongated *V*-band that consists mostly of shear vorticity (see Fig. 3.2f). It is clear that this intense cyclonic vorticity is the result of convective and baroclinic (vorticity) interaction associated with the convective band and the large-scale front over a period of 36 h. Hereafter, the large-scale baroclinic forcing begins to influence the evolution of the oceanic storm. Nonetheless, the intense south-to-southwesterly surface jet, with speeds greater than 30 m s^{-1}, is seen closely related to the development of the convective band.

To quantify the relative significance of the convective versus baroclinic forcing in generating the vorticity structures presented above, a sensitivity simulation is performed in which both the grid-scale latent heat release and the convective schemes are gradually turned off after the first 24 h integration (experiment NLH). It is obvious from Fig. 3.3 that the model produces a band of cyclonic(shear) vorticity associated with the low-level southwesterly jet at 22/00-60; but its magnitude is at most 40% of that along the convective *V*-band in the control run (cf. Figs. 3.2a and 3.3a). Since the low-level winds and horizontal shears in the vicinity of the dissipated MCSs at 20/12-24 are weak and since this *V*-band coincides well with the south-west-northeast elongated convergence zone offshore (cf. Figs. 2.19-21 in Chapter 2 and Fig. 3.3a herein), we may state that the stretching of planetary vorticity ***during the previous 36 h*** accounts for the generation of such a low-level *V*-band. Because of the continued weakening of the mesovortex circulation in the absence of diabatic heating, its lower-level residue vorticity could not be maintained as in the control run (cf. Figs. 3.2a, 3.3a, and 3.4a,b). Otherwise, stretching of the vortex's residue vorticity would also make some but secondary contribution to the *V*-band. After another 24 h integration, that is, at 23/00-84, the intensity of the *V*-band has increased slightly due to the continued stretching production (of absolute vorticity) against dissipative destruction, but with no sign of a closed circulation or a comma-shaped vorticity pattern. This is consistent with the simulation of a surface frontal trough at the end of the 84 h integration (see Fig. 2.14 in Chapter 2). Furthermore, the magnitude and area coverage of the *V*-band are much smaller than those associated with the control-

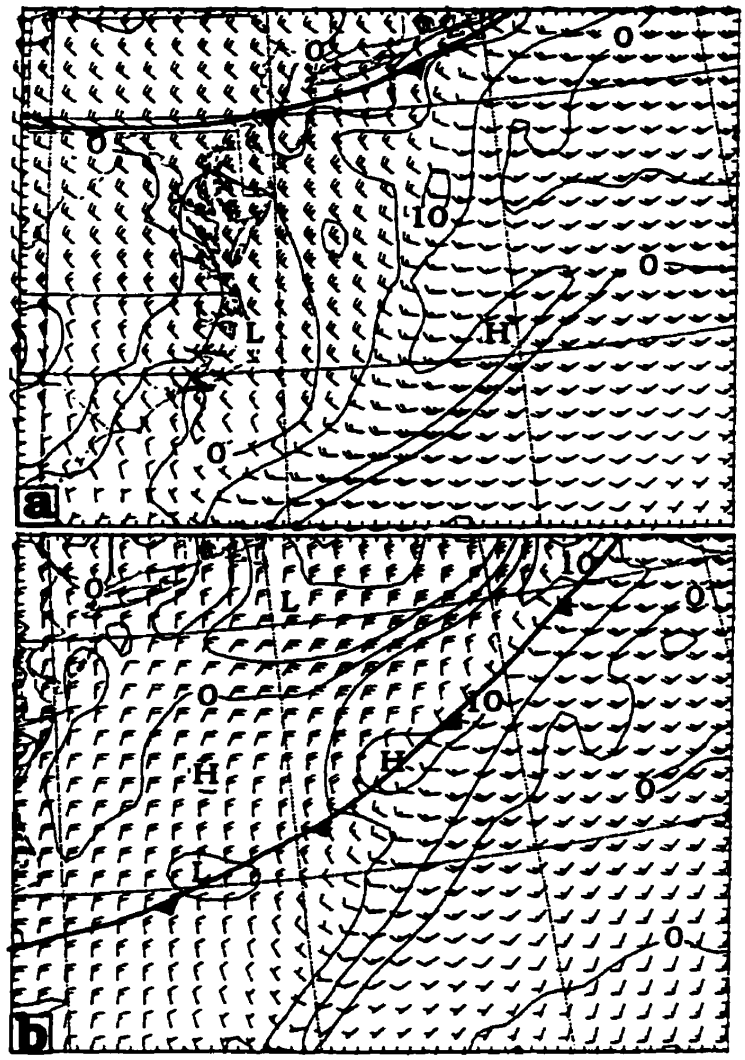

Fig. 3.3 As in Fig. 3.2 but from experiment NLH (i.e., no latent heating) at (a) 22/00-60 and (b) 23/00-84.

simulated. All this reinforces the previous conclusion that the intense vorticity concentration near the cyclone center and their wrapping-around features are mainly a consequence of the convective development along the oceanic storm.

3.3 Vertical structures

To gain insight into the aforementioned low-level wrapping-around processes in relation to the midlevel mesovortex, Figs. 3.4a-c show vertical cross sections of relative vorticity and horizontal winds through the center of the surface mesolow at the three important life-cycle stages, that is, the dissipation of the continental MCS and the incipient and mature stages of the oceanic storm. Figures 3.5a-c present the corresponding height and temperature deviations as well as vertical motion. All deviations are obtained by deducting their pressure-level averages in the cross section. One can see from Figs. 3.4a and 3.5a that the continental MCSs leave behind a deep and vertically coherent mesovortex up to 450 hPa at 20/12-24. This deep circulation is associated with a deep layer of lower heights (i.e., the short-wave trough). It is apparent that this short-wave trough, with the maximum intensity occurring near 650 hPa, is characterized by a warm core ($> 2°C$) above 650 hPa and a cold anomaly ($< -2°C$) below (see Fig. 3.5a). As shown in ZF86, Zhang et al. (1988), and Zhang (1989), these vertical thermal anomalies are produced by parameterized and grid-scale heating aloft and moist downdrafts and evaporative cooling below within the continental MCSs. Such a vertical thermal structure has been observed at the early stages of tropical cyclogenesis during TEXMEX (see Emanuel et al. 1993; Lopez et al. 1993; Bister and Emanuel 1997) and it is also of typical to continental MCSs near

the end of their life cycle (BS81; Fritsch et al. 1994). *Because of the cold (warm) anomaly in the lower (upper) portion of the mesovortex, the magnitude of short-wave trough decreases toward the surface (upward), leading to a much weaker surface pressure trough* (cf. Figs. 3.5a and 3.1a), as has been noted during TEXMEX. It follows that *mesovortices tend to be better maintained at the interface between the warm anomaly above and cold pool below.* Such a vertical thermal/vorticity juxtaposition could also be expected from balanced flow considerations. It should be pointed out that these convectively generated vortex structures differ markedly from those in cold-core extratropical cyclones, which exhibit considerable vertical tilt in their developing stages.

It is important to notice the distribution of vertical motion with respect to the vortex circulation, although it is very weak everywhere at this stage. Specifically, the mesovortex is generally accompanied by upward motion ahead, though influenced by the dissipated MCS at this hour, and descending motion behind (Fig. 3.5a). This upward motion, which is more evident later in the lower levels, persists in the southwesterly flow of the vortex circulation even in the absence of diabatic heating (see Figs. 2.19-21 in Chapter 2). This forcing provides a favorable condition for the later initiation and organization of deep convection (e.g., see Fig. 3.5b). It is also important to notice that the vortex is embedded in an environment with very weak vertical shear except in the lowest 100 hPa (Fig. 3.4a,b); the strongest flow (<15 m s^{-1}) occurs near 700 hPa behind the vortex. As discussed in Chapter 2, such an environment is favorable for the maintenance of a midlevel mesovortex.

At 22/00-60, although the magnitude of the midlevel mesovortex has decreased by about 20% compared to that 36 h earlier, little change has taken place with its vertical structure, expect in the lowest 100 hPa where the cyclonic vorticity near the center has decreased notably (see Fig. 3.4b). It should be noted, however, that these changes in intensity are mainly caused by the vertical cross section that is taken through the center of the surface mesolow rather than of the mesovortex (see their different tracks given in Fig. 2.1 of Chapter 2). This result is remarkable, since the long-lived vortex circulation helps explain why certain MCSs, like those analyzed by Wetzel et al. (1983) and Fritsch et al. (1994), could sustain or undergo multiple developments when organized larger-scale energy supplies are available. Of particular relevance at this stage is the formation of a pronounced low-level *V*-band at the southeast periphery of the midlevel vortex/trough, a feature that has been observed during TEXMEX (Emanuel et al. 1993). As previously mentioned, this *V*-band is convectively generated along the oceanic storm (as marked by "CONV" in Figs. 3.4, 3.5, and 3.7), and it is this *V*-band that wraps around to contribute to the subsequent amplification of the surface cyclone. It is worthwhile noting that this convectively generated vorticity profile differs considerably from that which occurred with its continental counterpart. That is, the continental vortex occupies a deep layer in the vertical with its maximum intensity occurring between 800 and 700 hPa (see ZF87 and Fig. 3.4a), whereas the oceanic V-band is only confined in the lowest 200 hPa with its peak near 950 hPa. Since vortex stretching is the primary vorticity forcing in both cases, this difference appears to reflect different environments in which they are

generated. Specifically, the continental vortex develops in the trailing stratiform region of the MCC at the base of the midlevel short-wave trough with considerable preexisting curvature vorticity, whereas the oceanic *V*-band forms along the convective band along the *low-level southwesterly jet*, thus having maximum shear vorticity close to the ocean surface. Furthermore, the maximum convergence, determining the cyclonic vorticity production, occurs at a higher level in the continental MCC (often near the melting level, see Houze 1989) than that along the present convective band (cf. Figs. 9, 10 in ZF87 and Figs. 3.5b, 3.6 herein). In the oceanic case, more intense convergence or vortex stretching develops in the lowest 100 hPa and decreases abruptly upward (Fig. 3.6a), which is consistent with the low-level concentration of cyclonic vorticity (Fig. 3.6b). Such a vertical profile appears to be attributable to the development of weaker convectively generated downdrafts and the presence of weaker frictional dissipation in the maritime boundary layer.

At this incipient stage of the surface redevelopment, height deviations also exhibit somewhat different vertical structures from those that occurred 36 h earlier. Specifically, there is an increase in height gradients in the lower levels (i.e., below 850 hPa) but a decrease of the gradients aloft ahead of the vortex (Fig. 3.5b). This is in agreement with the tightening of the surface isobars (cf. Figs. 3.1a,b) and the development of the low-level southwesterly jet and the convective *V*-band (see Figs. 3.2a,b and 3.4b). Similar changes in height gradients also take place to the rear of the system. This suggests that *the vertical thermal couplet should be considered as a basic element of the vortex/trough system* in the presence of little vertical shear.

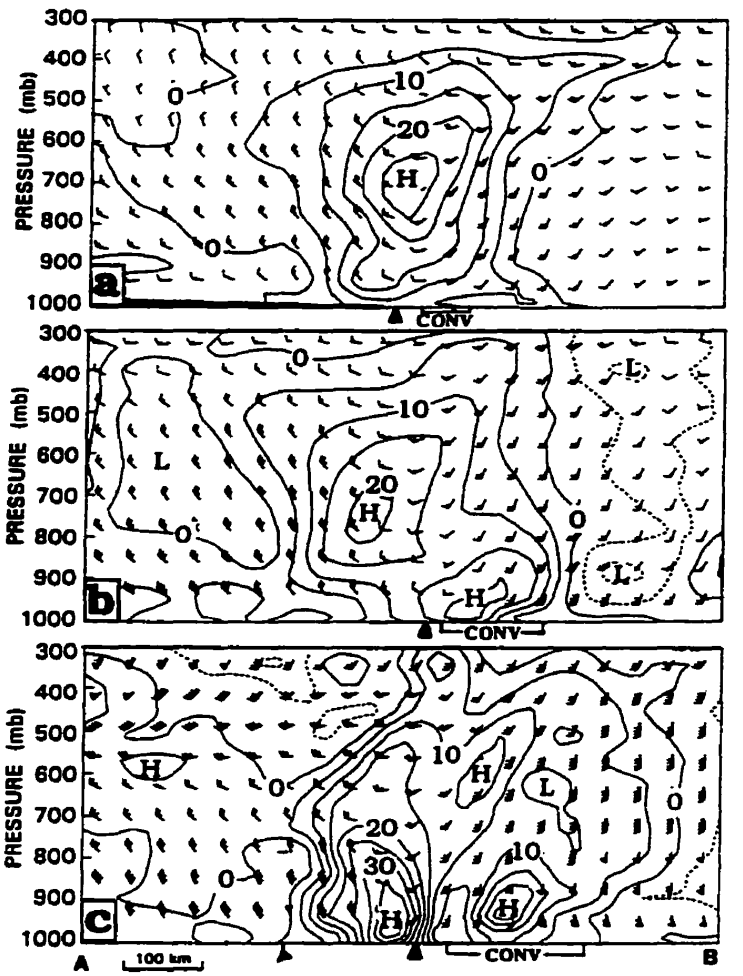

Fig. 3.4 Vertical cross sections of vertical relative vorticity at intervals of 5×10^{-5} s^{-1} and horizontal winds (see Fig. 3.2 for plotting convention) at (a) 20/12-24, (b) 22/00-60, and (c) 23/00-84, which are taken along line *AB* as given in Figs. 3.1a, 3.1b, and 3.1d, respectively, with a length scale of 800 km. Symbols along the abscissa show locations of the cold front, the surface cyclone center (▲) and the convective forcing region (CONV).

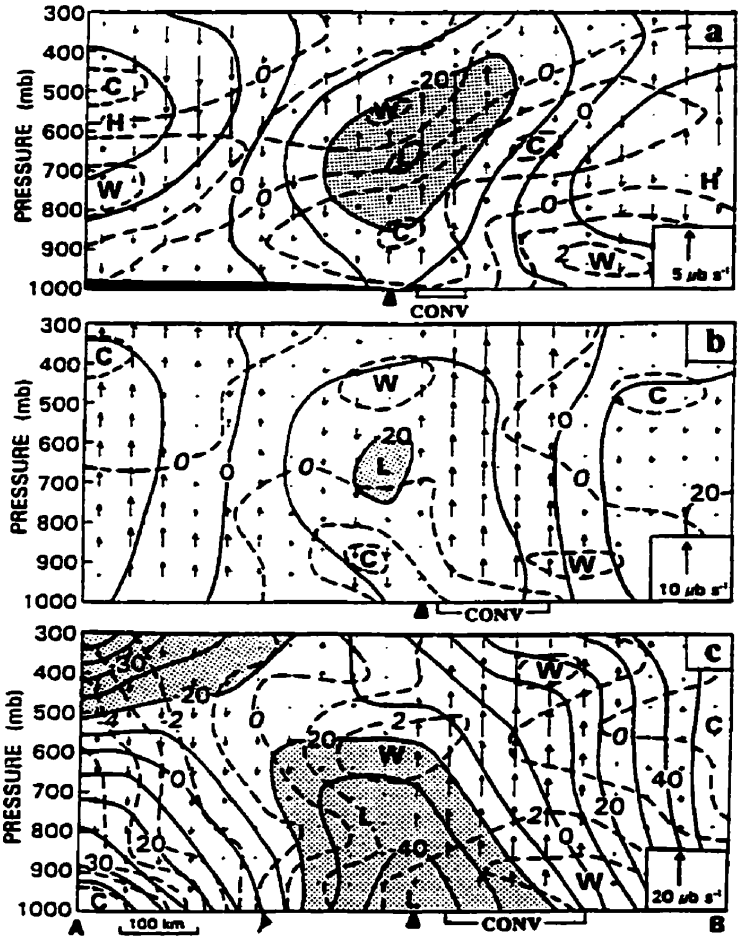

Fig. 3.5 As in Fig. 3.4 but for deviation heights (solid, every 10 m) and deviation temperature (dashed, every 1°C), superposed with vertical motion. Shadings denote negative height anomalies less than -20 m. Symbols along the abscissa give locations of the cold front, the surface cyclone center (▲) and the convective forcing region (CONV).

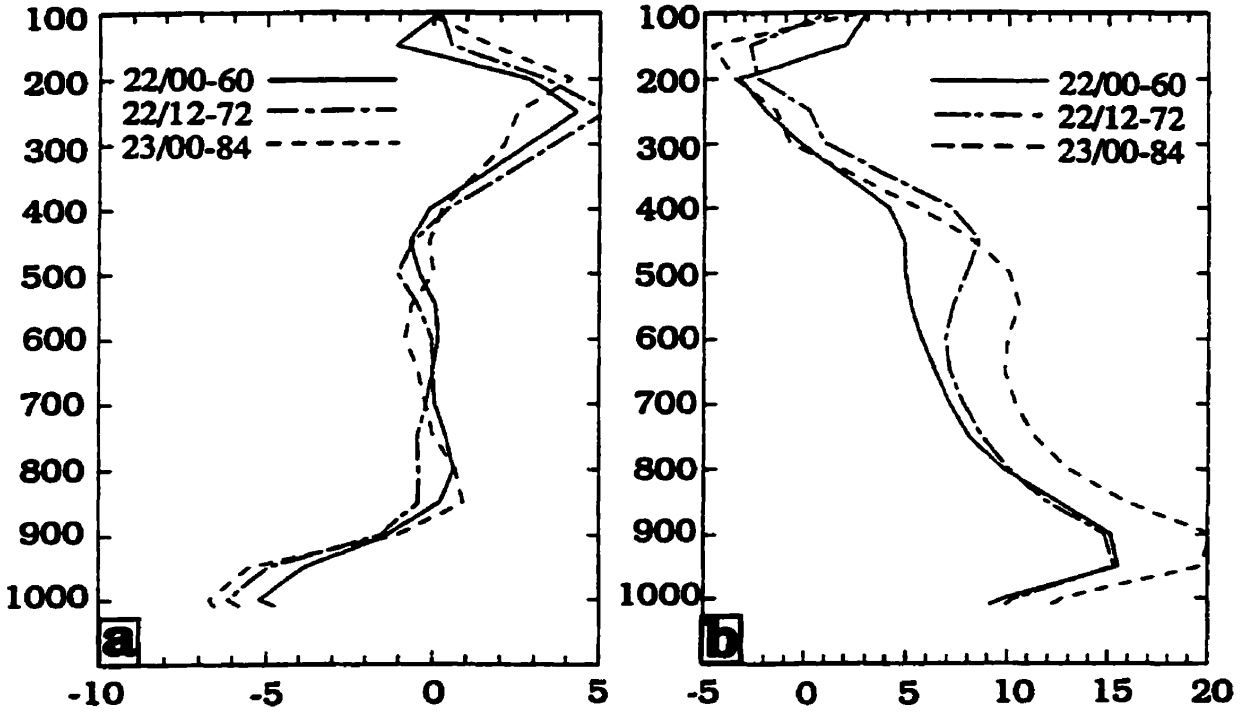

Fig. 3.6 Vertical composite profiles of (a) divergence (10^{-5} s^{-1}) relative vorticity (10^{-5} s^{-1}) that are obtained by averaging them along the vorticity axis of the convective axis of the convective band with a lateral scale of 150 km at 22/00-60 (solid), 22/12-72 (dot-dashed), and 23/00-84 (dashed).

Moreover, the maintenance of the low-level cold anomaly in the present case does not require further evaporation of rainwater from the MCS as hypothesized by Emanuel et al. (1993).

A vertical cross section of relative humidity and equivalent potential temperature θ_e , given in Fig. 3.7a, shows the presence of relatively higher-θ_e and moister columns along the convective band (CONV) in the southwesterly portion of the vortex flow. This mid- to upper- level moistening is achieved by the parameterized detrainment in the Kain and Fritsch (1990, 1994; hereafter KF) convective scheme and mesoscale ascent, whereas at the lower levels, a θ_e ridge is produced along the convective band as a result of the upward transfer of surface fluxes and vertical advection. It has been illustrated in Chapter 2 that this low-level θ_e anomaly tends to wrap around in a slantwise fashion into the cyclone center, causing conditional instability in the vicinity of the convective band. Of significance is that the mesovortex has always been accompanied by a midlevel high θ_e anomaly, just like its pertinent cyclonic vorticity structure (cf. Fig. 11 in ZF87 and Figs. 3.5a,b herein). As discussed by ZF87, this is due partly to the inertial stability of the vortex, which produces resistance to radial transport of energy, and partly to the weak-sheared environment, which slows down the transport of energy away from the vortex columns. The two factors are essentially responsible for the maintenance of the vortex circulation's in a vertically coherent manner.

At the cyclone's mature stage, that is, 23/00-84, both the height gradients and horizontal winds have experienced considerable increases, especially at lower levels

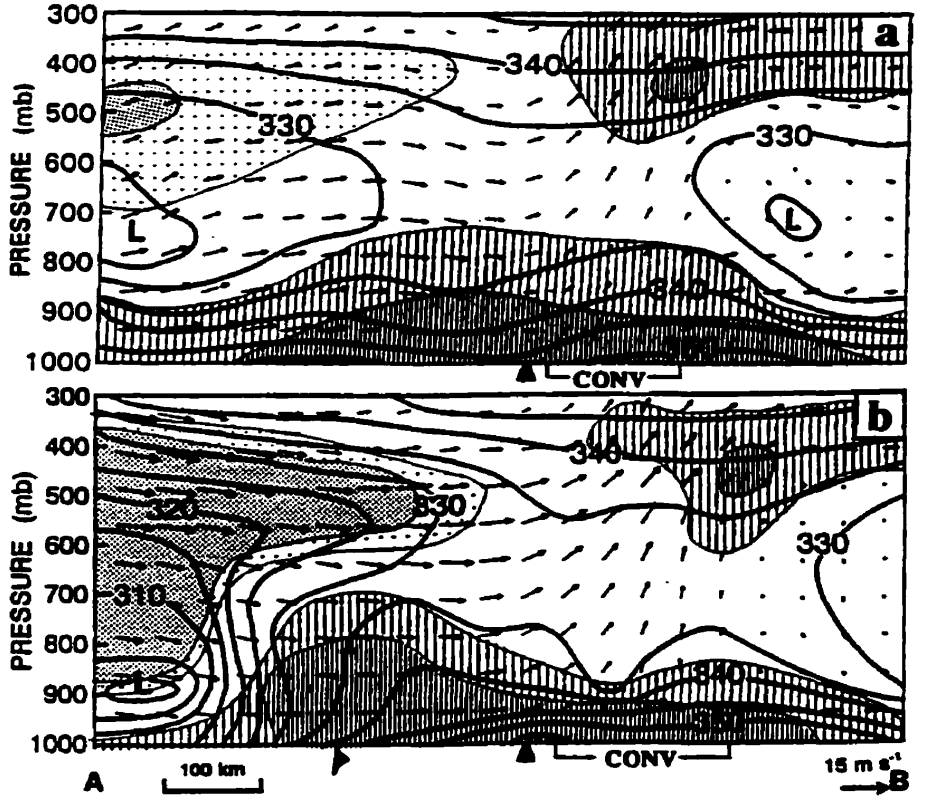

Fig. 3.7 As in Figs. 3.4b,c but for equivalent potential temperature θ_e at intervals of 5 K, superposed with along-plane flow vectors. Only the scale of the horizontal speed is given. Wide (narrow) hatching denotes areas with RH>70%(80%), whereas coarse (dense) shading denotes areas with RH< 40%(30%). Symbols along the abscissa give locations of the cold front, the surface cyclone center (▲), and the convective forcing region (CONV).

(Figs. 3.4c and 3.5c). Likewise, stronger mesoscale ascent(~20 μb s^{-1}) and cyclonic vorticity have developed along the convective band. Vertical composite divergence and vorticity profiles also exhibit the continued amplification (see Figs. 3.6a, b), but with more significant changes taking place in the lowest 200 hPa. Of particular interest is the development of a concentrated *V*-band up to 700 hPa in the vicinity of the cyclone center, with its maximum magnitude exceeding 40×10^{-5} s^{-1}. The lower-level concentration of intense cyclonic vorticity, like that shown in Fig. 3.6b, is also a typical feature of tropical cyclones (Frank 1977; Davidson et al. 1990). However, the precise dynamic mechanism responsible for such a vorticity concentration still remains elusive. Based on their Doppler radar analysis and Davidson et al.'s (1990) dataset, Mapes and Houze (1993) suggested that this intense vorticity could be generated as the midlevel mesovortex descends to the surface and then amplifies in the presence of intensifying low-level inflows. We have shown in section 3.2 that this low-level intense vorticity forms at the southern periphery of the midlevel mesovortex as a consequence of the slantwise wrapping around of shear vorticity that is generated along the convective band, and then converted to curvature vorticity. This discrepancy is likely due to their datasets that are either too coarse to resolve the convectively generated vorticity structures along rainbands using the Australian tropical analysis in Davidson et al. (1990; 1.25° latitude-longitude grid) or too limited to cover both the vortex and rainband circulation's using airborne Doppler radar observations in Mapes and Houze (1993). Thus, our result clearly suggests that obtaining a reasonable description of individual rainbands and their collective effects

on tropical cyclogenesis with high-resolution observations or numerical simulations is instrumental in understanding different processes that are responsible for oceanic or tropical cyclogenesis.

The relationship between the low-level vorticity amplification and the midlevel mesovortex can be inferred from Figs. 3.4b,c and 3.5b,c. It is seen that ascending motion always dominates the southwesterly portion of the vortex circulation where the convective *V*-band intensifies, whereas weak vertical motion occurs elsewhere. Thus, the mesovortex makes little direct contribution, that is, through vertical advection, to the generation of the intense vorticity at 950 hPa. Moreover, the low and midlevel vorticity anomalies remain as two separate entities until the surface cyclone enters the mature stage and overpowers completely the mesovortex circulation (Figs. 3.4b,c). Of course, it by no means indicates that the mesovortex has little impact on the development of the vorticity band. In fact, the vortex circulation provides a favorable condition for the deepening of the cyclone, at least, *the necessary cyclonic vorticity to stretch in the presence of convergence in the PBL*. This could be seen from Figs. 3.2-5, which shows that the convective *V*-band amplifies within a broad cyclonic circulation. The more important role of the mesovortex has been shown in Chapter 2 to assist the initiation and organization of deep convection along the oceanic storm. In this respect, the oceanic cyclogenesis should be regarded as induced by the mesovortex/MCS system through the stretching of its residue cyclonic vorticity and the organization of deep convection in the right environments (e.g., ahead of the trough axis, the land-ocean contrasts, the warm Gulf

Stream water, and tropical energy supply). Once it is established, the cyclone tends to overpower the vortex circulation, at least in the lower troposphere. On the other hand, deep convection along the oceanic storm helps intensify the midlevel mesovortex (see Figs. 2.17b, c in Chapter 2 and Fig. 3.6b herein) mainly through vortex stretching in the ascending flow, as will be seen in the next section. Without it, experiment NLH shows the continued weakening of the vortex under the influence of numerical diffusion and (weak) larger-scale deformation (e.g., see Fig. 3.3).

Similar to the deep vorticity concentration, a deep θ_e ridge (up to 700 hPa) is generated to the northwest of the cyclone, that is, in the cyclonic northerly flow (cf. 2.13c in Chapter 2 and 3.7b herein). It is apparent that this θ_e ridge results from the slantwise wrapping-around of the high-θ_e air generated along the convective band, as shown in Chapter 2, since θ_e is a conserved variable in an inviscid, pseudoadiabatic flow and since little upward motion occurs in the cyclonic northerly flow. (The θ_e trough between the two ridges corresponds to a lower-θ_e slot embraced by the high-θ_e tongue in Fig. 3.13c of Chapter 2.) In addition, the wrapping-around process produces a deep "wall-like" θ_e structure behind the cold front, which is again an indication of the blocking effect of the cyclone on the movement of the frontal system. For a similar reason, the low-level cyclonic flow transports ambient warmer air into the vicinity of the cyclone, thereby *eliminating the cold anomaly in the lower portion of the troposphere* (cf. Figs. 3.5a-c and 3.7b); see section 3.5 for the depiction of horizontal thermal advection. (A wall-like deviation thermal profile is also evident to the rear of the system.) As a result, the surface cyclone is now situated beneath a

deep column of relatively warmer air, causing the greatest pressure drop *at the surface* (see Fig. 3.5c). In the present case, the transformation takes 24 h as the lower troposphere is gradually warmed and the midlevel mesolow becomes less distinct in shape. The large-scale flow, including the baroclinic trough/cold front and a subtropical high, appears to play a role in steering the propagation of the oceanic storm/cyclone system, as discussed in Chapter 2. It is also evident that the cyclone will continue to deepen as long as more high-θ_e air can be transported into the system and more deep convection develops.

3.4 Vorticity budgets

After seeing in the preceding two sections the kinematic structures and evolution of cyclonic vorticity associated with the oceanic cyclone/storm system, it is desirable to examine quantitatively what dynamic processes are responsible for the spinup of the cyclone's vorticity. This is done in this section by computing the three-dimensional vorticity budget using the dynamically consistent model dataset. The vorticity equation in isobaric coordinates is

$$\frac{\partial \zeta}{\partial t} = -\mathbf{V}\cdot\nabla\eta - \omega\frac{\partial \zeta}{\partial p} - \eta\nabla\cdot\mathbf{V} - \mathbf{k}\cdot\left(\frac{\partial \mathbf{V}}{\partial p}\times\nabla\omega\right) + \mathbf{k}\cdot\left(\nabla\times\frac{\partial \mathbf{F}}{\partial t}\right), \tag{3.1}$$

where ζ is the vertical component of relative vorticity, $\partial/\partial t$ is the local tendency, $\mathbf{V}$ is the horizontal wind vector, η is the absolute vorticity, $\omega = dp/dt$, and $\mathbf{F}$ denotes the effects of boundary layer friction and numerical diffusion on horizontal momentum.

The intensity changes of a cyclone can be described by its vorticity changes that are determined by the terms on the rhs of Eq. (3.1). They are, respectively, the horizontal advection of absolute vorticity, the vertical vorticity advection, the generation of vorticity through vertical vortex stretching, the generation of vorticity through tilting horizontally oriented vorticity into the vertical by nonuniform vertical motion, and the frictional effects due to numerical diffusion and the boundary layer flux divergence. The last three terms represent the sources and sinks of relative vorticity. All terms, including the vorticity tendency, are then computed using the instantaneous model output of all the terms in the momentum equations. Thus, little residue will appear in the present budget calculations after excluding the effect of numerical diffusion.

Figure 3.8 shows the contributions of stretching and horizontal advection to the local vorticity tendencies at 950 hPa at 22/00-60 over a sub-domain that is smaller than that used in Figs. 3.1-3.3. The contributions due to other terms in Eq. (3.1) will be presented for 23-00-84, since they are extremely small at earlier development stages. One can see that vortex stretching exhibits marked cyclonic production along the convective band where convectively induced convergence and vorticity are maximized (cf. Figs. 3.2a and 3.8b). There is also a center of moderate cyclonic stretching tendency associated with the baroclinic *V*-band. In contrast, the effect of horizontal advection[8] depends on the magnitudes of cross-vorticity contour flow and vorticity gradients along the cyclonic flow. Thus, the horizontal advection always shows a couplet of cyclonic-anticyclonic contributions (cyclonic ahead of and

[8] Note that the north-south advection of planetary vorticity, that is βv, accounts for less than 2.5% of the local vorticity changes associated with the baroclinic and convective V-bands, where $\beta \approx 1.8 \times 10^{-11}$ m^{-1} s^{-1}

anticyclonic behind the local absolute vorticity maximum along the current). Since the flow is skewed more along the *V*-bands, the cyclonic vorticity advection is much smaller in magnitude than its anticyclonic component behind except at their leading edges. The net result is that a marked cyclonic production occurs along the convective band mainly due to vortex stretching and a cyclonic reduction behind it as a result of the displacement of the *V*-bands (Fig. 3.8a). Of importance to note is the net vorticity increase at the leading edge of the convective *V*-band, which is consistent with the subsequent formation of a comma head over the region (cf. Figs. 3.2a-c and 3.8a). This net vorticity increase is seen to result primarily from the northeastward advection of cyclonic vorticity along the convective *V*-band (cf. Figs. 3.8a,c and 3.2a-c). Some minor discrepancies exist outside the convective region (Fig. 3.8a), which are attributable to the vertical transport of cyclonic vorticity (not show).

At 22/12-72, the formation of the comma vortex causes significant alterations in the cyclonic flow (cf. Figs. 3.1b, c and 3.2a-c). Specifically, the weak-flow air mass has been wrapped around to the wake of the convective band and the flow directions have changed from southwesterly to near-southerly along the band and from northwesterly to westerly behind it (cf. Figs. 3.8a and 3.9a). By comparison, the stretching contribution is always robust as the cyclone deepens; its magnitude almost doubles during the previous 12 h along both the convective and baroclinic *V*-bands (Fig. 3.9b). As before, the net effect is to increase cyclonic vorticity along the *V*-band and decrease it behind (Fig. 3.9a). It is of interest that weak vorticity or little vorticity generation occurs along the west-east-oriented trailing portion of the oceanic

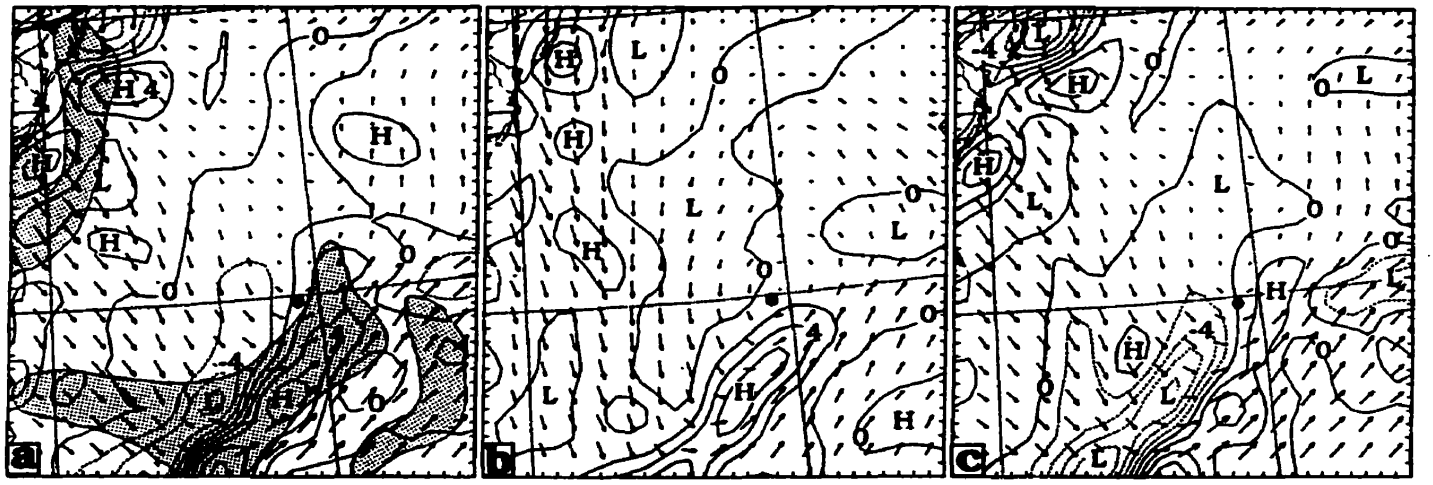

Fig. 3.8 Horizontal maps of the relative vorticity budget at intervals of 2×10^{-5} s^{-1} h^{-1} at 950 hPa from 60-h simulation (i.e., 22/00-60): (a) local vorticity tendency ($\partial\zeta/\partial t$); (b) vortex stretching ($-\eta\nabla \cdot \mathbf{V}$); and (c) horizontal advection ($-\mathbf{V} \cdot \nabla\eta$). superposed are wind vectors at 950 hPa plotted at every other point (1 grid length represents 14 m s^{-1}) except for (b) in which system-relative winds are plotted. Solid (dashed) lines are positive (negative) tendencies. Solid circle denotes the surface cyclone center. The surface frontal position and the convective distribution, as shaded, are given in (a).

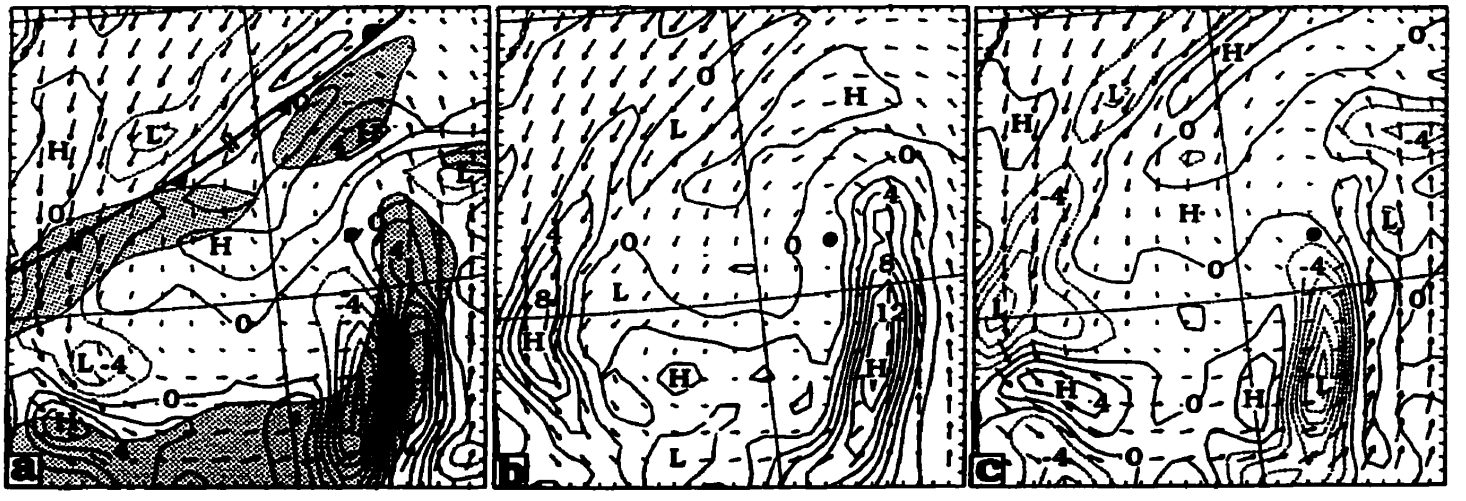

Fig. 3.9 As in Fig. 3.8 but for 22/12-72, superposed with vectors at 950 hPa plotted at every other point (1 grid length represents 16 m s^{-1}) except for (b) in which system-relative winds are plotted.

storm in spite of the widespread convective development (Fig. 3.8a and 3.9a). This is because this trailing convective portion is initiated at the outer edge of anticyclonic flow associated with a subtropical high (see Fig. 3.2), which is an unfavorable region for cyclonic amplification.

Figure 3.10 presents contributions from all rhs terms in Eq. (3.1) to the net vorticity tendencies at 23/00-84. Again, the net vorticity changes are dominated by cyclonic production along the convective band through vortex stretching(cf. Figs. 3.10a, b), and by cyclonic depletion through horizontal advection except over the leading portion of the *V*-band where the large cyclonic vorticity tendency is mainly associated with vorticity advection by northerly winds (cf. Figs. 3.2e and 3.10d). It should be noted that while the stretching production determines the amplification of cyclonic vorticity, the horizontal advection plays a role in transporting the necessary cyclonic vorticity to the leading portion or ahead of the *V*-bands for vortex stretching in the presence of intense convergence, thereby causing the wrapping-around of cyclonic vorticity. This advection-stretching interplay appears to help explain why the peak cyclonic vorticity always tend to occur at the leading edge of the *V*-band (see Figs. 3.2a-d). without the horizontal vorticity advection, stretching of the planetary vorticity by convectively induced convergence would be too slow a process to account for the rapid vorticity amplification, like that which occurred in the trailing portion of the oceanic storm.

As compared to the stretching contribution, the vorticity production through the tilting of horizontal vorticity is small and less organized (cf. Figs. 3.10b, c), due to

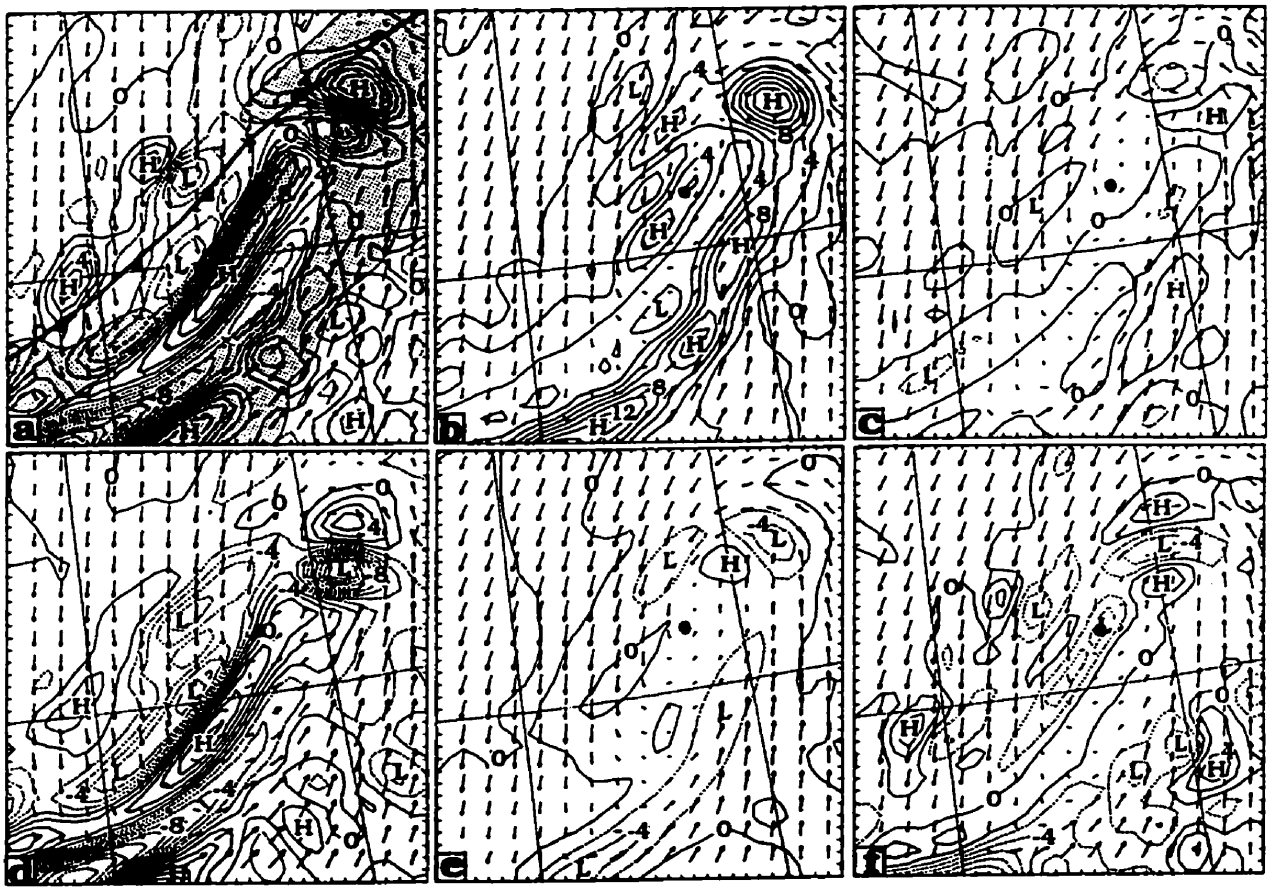

Fig. 3.10 As in Fig. 3.8 but for 23/00-84: (a) local vorticity tendency ($\partial\zeta/\partial t$); (b) vortex stretching ($-\eta\nabla\cdot\mathbf{V}$); (c) tilting of horizontal vorticity ($-\mathbf{k}\cdot\partial\mathbf{V}/\partial p\times\nabla\omega$); (d) horizontal advection ($-\mathbf{V}\cdot\nabla\eta$); (e) vertical advection ($-\omega\partial\zeta/\partial t$); and (f) frictional effects($-\mathbf{k}\cdot\nabla\times\partial\mathbf{F}/\partial t$). Superposed are wind vectors at 950 hPa plotted at every other point (1 grid length represents 20 m s^{-1}) except for (b), (c), (e), and (f) in which system-relative winds are plotted.

the presence of weak vertical motion coupled with weak vertical shear along the convective band (Figs. 3.4 and 3.5). The tilting production at 950 hPa is even smaller in magnitude than the frictional destruction of cyclonic vorticity associated with downward momentum fluxes; but they are opposite in sign (cf. Figs. 3.10c, f). Above 950 hPa, the tilting contribution becomes anticyclonic because of the negative vertical shear, whereas toward the surface the frictional damping increases (not shown). This pronounced frictional damping has also been noted by Tuleya and Kurihara (1984; see their Fig. 11) in their tropical cyclogenesis study. The effect of upward transport over the convective regions is to reduce the cyclonic vorticity at 950 hPa and increase it above, as the system's cyclonic circulation is maximized at the level (Fig. 3.10e). Obviously, this leads to the increased depth of the convective *V*-band as it is wrapped around into the cyclonic northerly flow in a slantwise fashion (see Fig. 3.4c), as previously discussed. In summary, we may state that the convective *V*-band, shown in Figs. 3.2a-f, results initially from the stretching of planetary vorticity plus residue vorticity of the mesovortex, whereas the sustained vorticity growth near the cyclone center occurs as the cyclonic vorticity generated along the *V*-band is advected into the cyclone center and enhanced further through the stretching of absolute vorticity.

To help understand further the vertical structures of vorticity changes in relation to the midlevel vortex discussed in section 3.3, we present in Fig. 3.11 vertical cross sections of the two major vorticity contributors, that is, stretching production and horizontal advection, to the local vorticity changes at 23/00-84. Apparently, the intense vortex stretching occurs only in the lowest 100 hPa with its

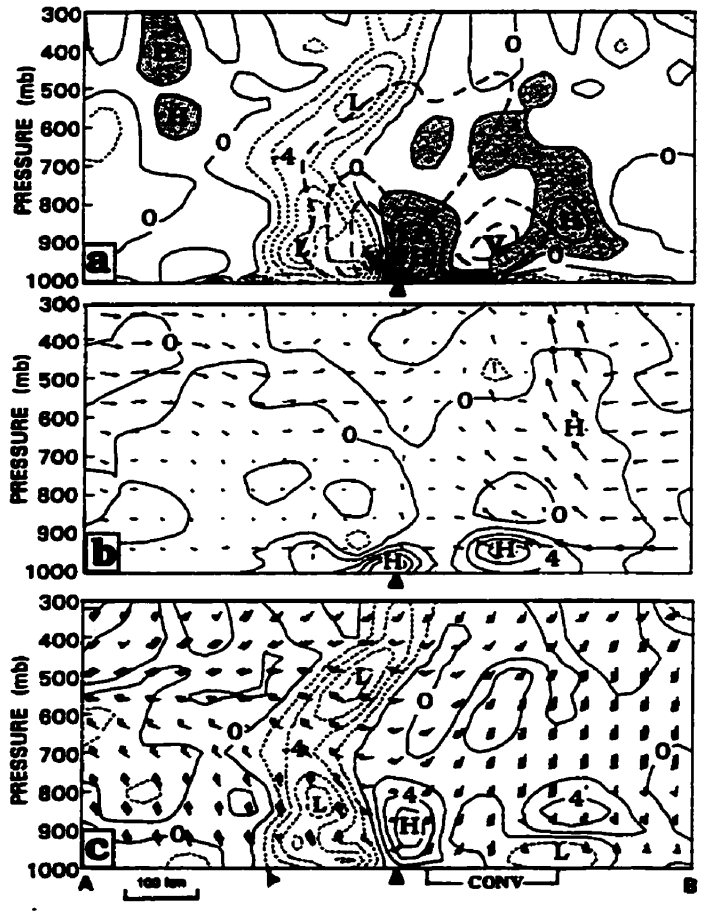

Fig. 3.11 As in Fig. 3.4c but for the relative vorticity budget at intervals of 2×10^{-5} s^{-1} h^{-1} : (a) local vorticity tendency ($\partial\zeta/\partial t$, the growth rates larger than 2×10^{-5} s^{-1} h^{-1} are shaded), superposed with cyclonic vorticity (long-dashed, every 10^{-4} s^{-1}) with the centers denoted by "V," (b) vortex stretching ($-\eta \nabla \cdot \mathbf{V}$), superposed with secondary circulation vectors that are constructed from along-plane flow perturbations (i.e., after deducting a mean flow of 8 m s^{-1}) and vertical motion; and (c) horizontal advection ($-\mathbf{V} \cdot \nabla\eta$), superposed with horizontal winds. Solid (dashed) line are positive (negative) tendencies, Symbols along the abscissa give locations of the cold front, the surface cyclone center (▲) and the convective forcing region (CONV).

maximum production near 950 hPa, where both the absolute vorticity and convergence are peaked (cf. Figs. 3.11b, 3.6, and 3.4c). Higher up, the stretching makes cyclonic, though weak, contribution to the slow intensification of the midlevel mesovortex in the presence of relatively weak convergence associated with convectively generated secondary circulation's (see Figs. 3.6 and 3.11b). The vorticity advection couplets due to the displacement of vorticity centers are also evident in deep layers. Again, the local cyclonic vorticity tendency near the cyclone center, especially above 950 hPa, results primarily from the horizontal advection of cyclonic vorticity from the convective *V*-band where it is generated (cf. Figs. 3.1d and 3.11a, b). this advective effect can be further seen from weak vertical motion and weak convergence in the PBL near the cyclone center(cf. Figs. 3.4b, c and 3.11b), since they indicate that both vortex stretching and tilting of horizontal vorticity are negligible over the region. At 23/00-84, however, the (narrow and shallow) stretching contribution near the center happens to be notable because of the development of a weak convective line ahead of the surface front (cf. Figs. 3.1d, 3.10b, and 3.11b).

3.5. Thermodynamic budgets

In this section, potential temperature θ and equivalent potential temperature θ_e budgets are presented to help gain insight into the thermodynamic processes responsible for the transformation of a low-level cold pool to a warm-cored structure and the wrapping-around of high-θ_e air during the cyclogenesis stages. The prognostic θ equation in isobaric coordinates can be written as

$$\frac{\partial\theta}{\partial t} = -\mathbf{V}\cdot\nabla\theta - \omega\frac{\partial\theta}{\partial p} + \left.\frac{\partial\theta}{\partial t}\right|_{PBL} + \left.\frac{\partial\theta}{\partial t}\right|_{CON} + \left.\frac{\partial\theta}{\partial t}\right|_{COND} + \left.\frac{\partial\theta}{\partial t}\right|_{DIF} . \qquad (3.2)$$

Terms on the rhs of (3.2) are, respectively, the horizontal advection, vertical advection, the contributions due to the PBL, parameterized convection, grid-scale condensation plus cloud-radiation interaction, and all numerical diffusive processes. The last four terms represent the sources and sinks of thermodynamic energy, since θ is a conserved variable in an otherwise inviscid, adiabatic flow.

For the convenience of computing the θ_e budget from the temperature and water vapor tendencies, we use the following linear form of θ_e expression:

$$\theta_e \approx \theta + \frac{L\pi}{c_p} q_v ,$$

and

$$\pi = \left(\frac{1000hPa}{p}\right)^{R/c_p} ,$$

Where q_v is specific humidity and all the other symbols assume their usual meteorological meaning. The prognostic equation for θ_e can be written simply by replacing θ in Eq. (3.2) with θ_e. Like the vorticity budget, all the terms are then calculated using the instantaneous model output of corresponding terms in the temperature and specific humidity tendency equations (see Anthes et al. 1987). Again, there will be little residue involved in the θ and θ_e budget calculations after excluding the effect of numerical diffusion (i.e., $\partial\theta/\partial t)_{DIF}$

To facilitate the subsequent discussion of the θ and θ_e budgets, Fig. 3.12 shows the evolution of the thermal and height structures at 900 hPa where the negative thermal deviation is peaked prior to the cyclogenesis (see Figs. 3.5a, b). It is seen that a cold pool, left behind by the previous MCS, has propagated in pace with the trough/vortex system until 22/00-60. There are a warm tongue in conjunction with the cyclonic flow from the southeastern states eastward around the cold pool, a cold air mass to the southeast, and the rapidly propagating cold front from the northwest. It is of particular importance that the oceanic mesolow, as marked by " L_c," is initiated at the southeast periphery of rather than near the center of the cold pool (also see Figs. 3.2a-c), as also mentioned in Chapter 2. This mesolow corresponds closely to the development of a cyclonic vorticity center along the convective V-band with little evidence of a warm anomaly in the lower troposphere (cf. Figs. 3.2a, 3.5b and 3.12a), suggesting that *it is driven by the convectively generated vorticity field.* Because of this nonconcentric phase difference between the vortex and the new mesolow, the intensifying cyclonic flow, which overpowers quickly the vortex circulation in the lower levels, tends to destroy the cold-pool structure by advecting the associated cold air in its northerly flow into the convective band and the ambient warmer air into the system-- a reflection of the cyclone-convection interaction (see Fig. 3.12b). By 23/00-84, the cold pool has been completely absorbed by or circulated into the convective storm, causing a slight cooling of the warm tongue (cf. Figs. 3.12b, c). As a result, the isotherms become linearly distributed ahead of the cold front, which are in significant contrast to the

original circular pattern of the cold pool (cf. Figs. 3.12a, c). It is apparent that the thermodynamic transformation is primarily driven by the intensifying cyclonic circulation, namely, the organized vorticity field. Note that the convective band is always distributed along the warm (or high-θ_e) tongue (cf. Figs. 3.1 and 3.12), and the cyclone is now seen to draw warmer air from the east to northeast into the system. Evidently, the thermodynamic transformation in the present case, at least above 950 hPa, differs from the hypothesis of Emanuel et al. (1993) that the cold pool is mainly heated through the upward transfer of surface heat and moisture fluxes over warm ocean.

Some selected maps of the θ budget during the thermodynamic transition period, that is, 22/12-72, are presented in Fig. 3.13, which does show the evidence of cold advection into the convective storm in the cyclonic northerly flow and warm advection into the cyclone system from the northeast of the cyclone (cf. Figs. 3.13a, b and 3.12), although they are weak due to the slow transformation. Over the convective region, the diabatic heating and vertical adiabatic cooling dominate the budget but with opposite signs (Figs. 3.13c, d). In general, the θ tendency is determined by subsidence warming immediately to the east of the convective band, horizontal advection associated with the thermal anomalies around the cyclone center (cf. Figs. 3.13b and 3.12b), and the small difference between the convective heating and vertical advection inside the storm. Consequently, it produces net cooling along the north-south-oriented convective region and an elongated zone of net warming along the westerly to southwesterly jet. It is of interest to note that this warming

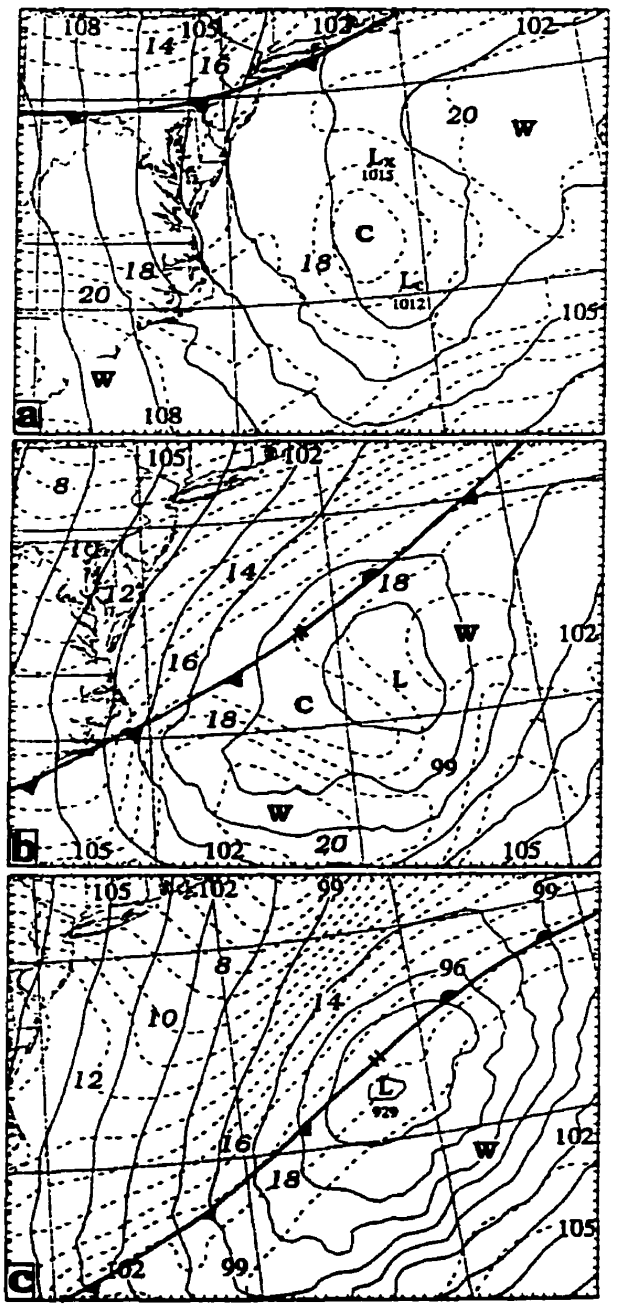

Fig. 3.12 Simulated geopotential height (solid) at intervals of 1.5 dam and temperature (dashed) at intervals 1°C at 900 hPa at (a) 22/00-60, (b) 22/12-72, and (c) 23/00-84. Letters "L_x" and "L_c" in (a) denote the minimum central heights at 900 hPa associated with the vortex/trough and the new mesolow, respectively.

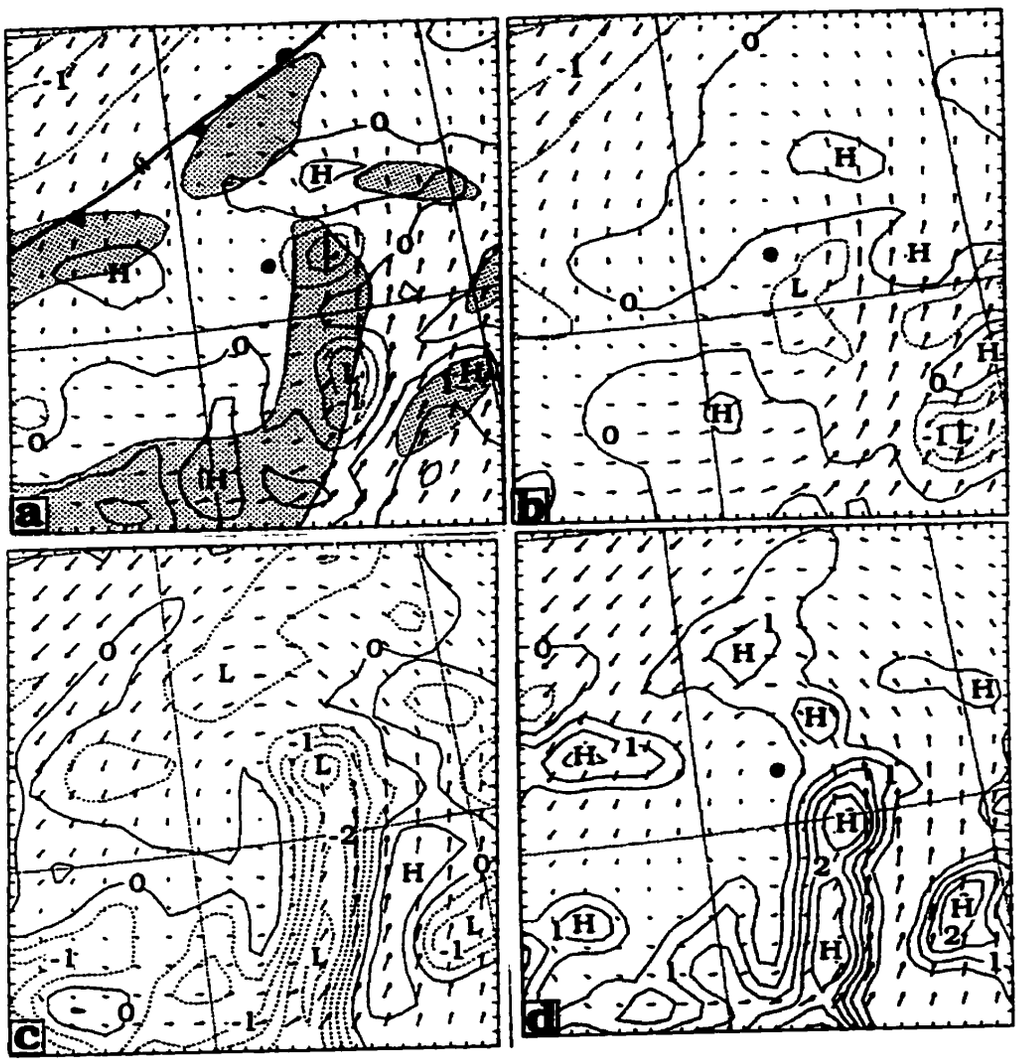

Fig. 3.13 Horizontal maps of the potential temperature (θ) budget at intervals of 0.5°C h^{-1} at 900 hPa from 72 h simulation(22/12-72): (a)the local θ tendency ($\partial\zeta/\partial t$); (b) horizontal advection ($-\mathbf{V}\cdot\nabla\theta$); (c) vertical advection ($-\omega\partial\theta/\partial p$); and (d) parameterized convection ($\partial\theta/\partial t|_{CON}$). Superposed are wind vectors at 900 hPa plotted at every other point (1 grid length represents 18 m s^{-1}) except for (c) and (d) in which system-relative winds are plotted. Solid (dashed) lines are positive (negative) tendencies. Solid cycle denotes the surface cyclone center. The surface frontal position and the convective distribution, as shaded, are given in (a).

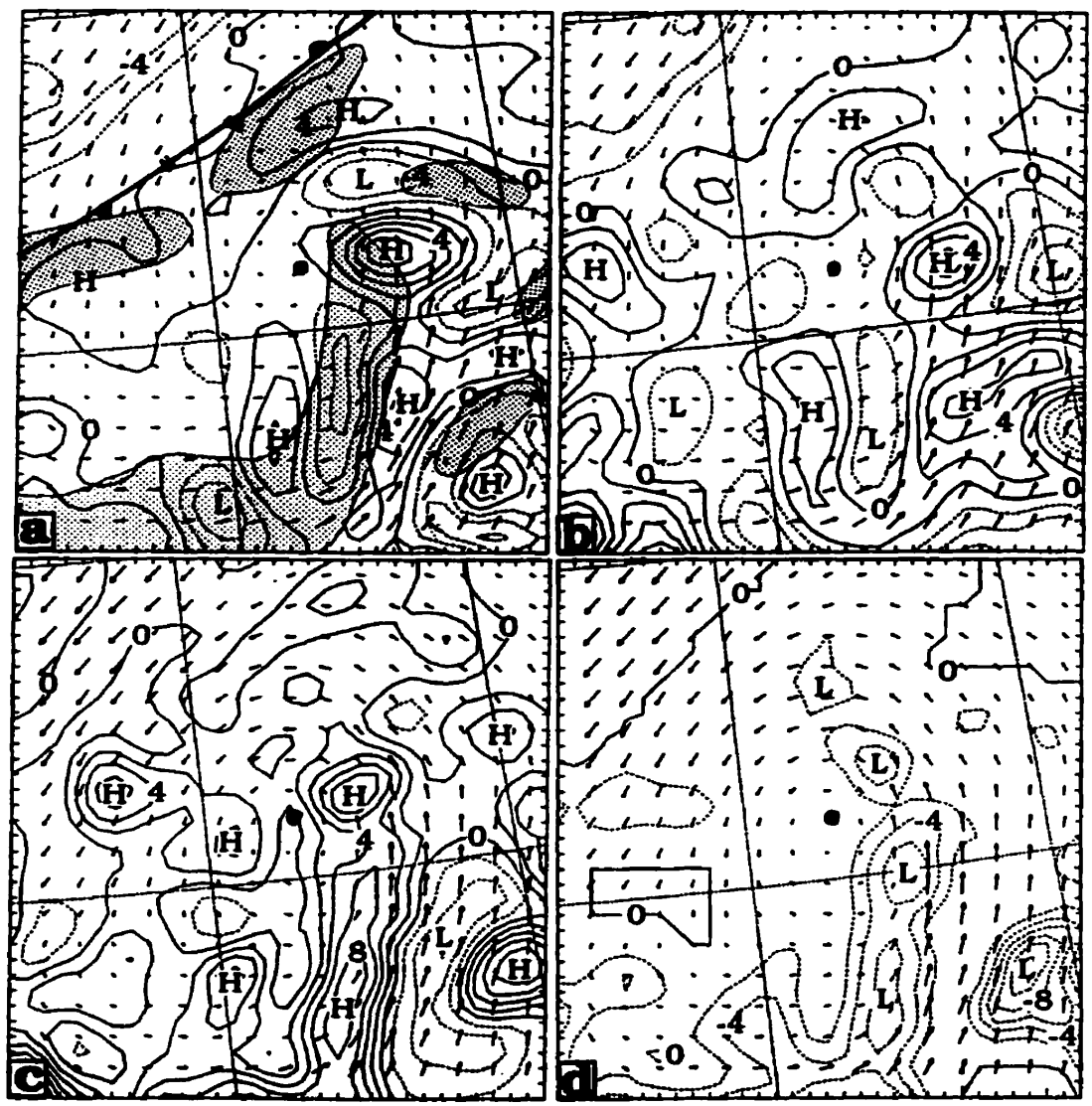

Fig. 3.14 As in Fig. 3.13 but for the equivalent potential temperature θ_e budget at intervals of 2 K h^{-1}.

pattern resembles well the distribution of deep convection at 23/00-84 (cf. Figs. 3.13a and 3.1d). This appears to suggest that the subsidence warming tends to suppress momentarily convective development, but it contributes to the conditioning of the convective environment for the organization of the oceanic storm as the warmer air is advected northeastward by the low-level jet.

Figure 3.14 shows the θ_e budget at 22/12-72 corresponding to the θ budget given in Fig. 3.13. Like in the θ budget, the θ_e tendency inside the convective storm is also dominated by the parameterized convection and vertical advection (Figs. 3.14c, d); but they are opposite in sign to their counterparts due to the inverse sign of θ and θ_e gradients in the vertical. With the θ-budget results in mind, we can see that vertical motion along the convective storm tends to transport moisture upward, whereas the parameterized convection removes it as precipitation reaching the surface. Unlike in the θ budget, however, the horizontal θ_e advection (mainly through moisture) accounts for a large percentage of high θ_e along the low-level jet, as well as the leading edge of the high -θ_e tongue (Fig. 3.14b). Thus, the horizontal θ_e advection plays an important role in vertically destabilizing atmospheric columns, especially at the leading edge, and spreading deep convection along the low-level jet, as mentioned in Chapter 2. The net result is an increase of θ_e along and immediately to the east of the convective band, which is consistent with the generation of a high-θ_e tongue along the low-level jet(cf. Figs. 2.11c and 2.13c in Chapter 2 and Fig. 3.14a herein).

3.6 Summary and conclusions

In this chapter, we examined the meso-β-scale structures of the long-lived MCSs that produced the July 1977 Johnstown flash flood, based on a 90 h real-data simulation. We focused on the evolution of intense cyclonic vorticity and the transformation of a low-level cold pool to warm-core anomaly associated with an oceanic cyclone/storm system. Model diagnosis has been performed to investigate how the oceanic cyclogenesis occurs at the south periphery of the dissipated MCS in relation to the large-scale environment, the convectively generated vortex/trough, and a new convective storm, after the system drifts into the Atlantic Ocean. Then, budgets of relative vorticity, potential temperature θ, and equivalent potential temperature θ_e have been carried out to gain insight into various dynamical and thermodynamic processes leading to the oceanic cyclogenesis.

It is shown that a surface mesotrough at the end of the life cycle of the continental MCC can be related to a midlevel short-wave trough characterized by a warm anomaly above and a cold anomaly below. Associated with the surface to midlevel trough is a deep and vertically coherent mesovortex. The vortex/trough system is shown to be capably *maintained for over 60 h* within a weak-sheared environment, which is the key to the successful prediction of the subsequent oceanic cyclone/storm development. As the vortex/trough moves into the warm Gulf Stream water at lower latitudes, its low-level pressure gradients in the southern quadrant intensify, giving rise to the enhanced mass and moisture convergence in the maritime boundary layer and the development of a new MCS at the southern periphery of the previously dissipated MCC. Then, the new MCS strengthens over the warm ocean

surface. Vertical transfer of surface fluxes from the warm ocean in the presence of intensifying surface winds, overcompensates the convective drying and cooling to generate a low-level high-θ_e tongue along the elongated convective storm. Meanwhile, stretching of the planetary vorticity plus the residue of the vortex's relative vorticity contributes to the formation of a cyclonic (shear) vorticity band along the new MCS. A first closed isobar of the surface cyclone appears at the southern periphery of the trough/vortex, as the shear vorticity is advected northward into a weak-gradient region and then converted to curvature vorticity.

In conclusion, we may state that the midlevel mesovortex, as it moves toward the warm Gulf Stream water, provides the necessary forcing for the initiation and organization of deep convection and the initial concentration of low-level cyclonic vorticity at its southern periphery. On the other hand, the new convective system contributes to the amplification of the low-level cyclonic vorticity through stretching in the presence of intensifying flow. The storm-cyclone interaction then eliminates the low-level cold anomaly, thereby accomplishing the transformation of the continental MCS/vortex system to an intense oceanic cyclone/storm system. It takes 24 h to get the oceanic storm organized and another 24 h to complete the thermodynamic transformation.

Chapter 4

Tropical cyclogenesis as induced by a midlevel mesovortex - an idealized simulation

4.1. Introduction

In the previous chapters, we presented a 90-h real-data simulation (RDS) which successfully reproduces the transformation of a mid-level mesovortex into a tropical storm. However, the RDS shows the presence of a strong cold front that may have influenced significantly the process of tropical cyclogenesis (see Zhang and Bao 1996a). Specifically, during the first 24 h integration, a subtropical high extends from the Atlantic Ocean to the central U.S. A convectively generated mesovortex is located over the northern periphery of the subtropical high and a cold front lies about 1000 km to its north-west. The front has no significant influence on the development of the mesovortex at this stage. During the next 36 hours, the subtropical high over land intensifies and the cold front advances toward the southeast by more than 1000 km. Meanwhile, the dissipating mesovortex moves southeastward into lower latitudes, driven by the strong anticyclonic flow of the high. Thus far, the cold front is involved in the adjustment of the large-scale flow with the subtropical high to provide a strong northwesterly flow to influence the movement of the mesovortex. At 60 h, the cold front lies about 500 km to the northwest of the mesovortex and new

convection is triggered ahead of the vortex. During the next 24 hours, when the distance between the cold front and the mesovortex becomes less than 200 km, the surface low associated with the oceanic storm undergoes rapid deepening and leads to the development of a tropical storm. Although the analysis of the simulation indicates that the baroclinic process associated with the front contributes only indirectly to the formation of the tropical storm, it is still difficult to determine the exact role of the baroclinic process. Moreover, the majority of tropical cyclones occur over an environment which is near barotropic. It is therefore desirable to re-examine the evolution of the mesovortex within an environment which resembles the basic subtropical high structure of the RDS but without the embedded frontal system. Such a scenario may be achieved by constructing an idealized initial condition.

Thus, the objectives of an idealized numerical experiment are to (i) simulate the life cycle of a mesovortex that could eventually lead to the formation of a tropical storm within an idealized barotropic environment; (ii) study the similarities and differences between the RDS and the idealized simulations; and (iii) investigate some processes directly related to the amplification of the vortex and the formation of the warm core associated with the tropical storm not fully revealed in the RDS.

4.2. Model description and initial conditions

4.2.1 Model features

Similar to the RDS, a modified version of the PSU-NCAR three-dimensional, hydrostatic, nested-grid, mesoscale model (Anthes et al, 1987) was used. The

essential features of the model include (i) an explicit moisture scheme containing prognostic equations for cloud water (ice) and rain water (snow) (Hsie et al. 1984; Zhang 1989); (ii) the Blackadar planetary boundary layer (PBL) parameterization scheme (Zhang and Anthes 1982); (iii) the Kain-Fritsch (1990, 1993; hereafter KF) convective parameterization scheme (CPS); (iv) the improved version of the Garand (1983) broadband infrared radiation scheme; and (v) a movable nested-grid procedure providing two-way interaction between the nested domains. In addition, a channel domain configuration, which is necessary to allow long time integration with idealized initial conditions, was added to the modeling system.

The nest-grid scale ratio is 1:3 with fine-mesh length of 25 km and a coarse-mesh length of 75 km. The vertical coordinate is defined as $\sigma = (p-p_t)/(p_s-p_t)$, where p_t is the pressure at the top of the model and p_s is the surface pressure. The dimensions of the coarse and fine meshes in the (x, y, σ) coordinates are 121 x 91 x 19 and 91 x 61 x 19, respectively. Fig. 4.1 shows both the coarse- and fine-mesh domains. From 48 to 54 h, the fine-mesh domain was moved gradually eastward to prevent the simulated system from being too close to the boundary. The dashed frame represents the final position of the fine mesh at the completion of the move.

4.2.2 Initial conditions

A modified version of the initialization package (Fritsch et al 1980; Chen 1990) was used to create analytical initial conditions for this study. First, the thermal structures of the atmosphere at all levels in the height Z-coordinate are specified. The

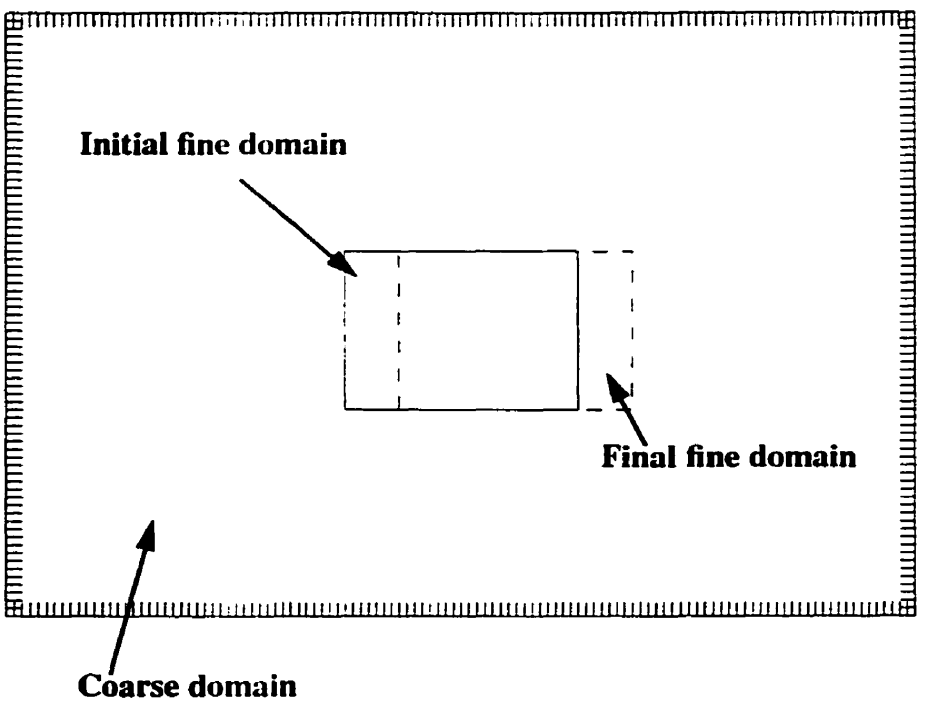

Fig. 4.1 Model domain for the idealized simulation. The dashed frame represents the final position of the mesh at the completion of the move.

pressure at a 'reference level' containing the most important characteristics of the flow pattern are also defined. Second, a three-dimensional moisture field is generated independently, consisting of a mean value and a perturbation value. The mean value is based on climatological condition over eastern U.S. and the west Atlantic Ocean. The perturbation is defined by a high value of relative humidity and resembles the environment favorable for MCS development in the designated area. Third, the surface pressure is calculated from the hydrostatic equation with virtual temperature obtained from the specified T and Q_v. To obtain a balanced wind field for the initial conditions, we first computed the wind using geostrophic approximation. We then calculated the total potential vorticity which was then inverted to obtain the velocity potential and stream function using the method developed by Davis (1992) and used in Huo et al. (1998). Finally, the wind field is recalculated using the velocity potential and stream function. The fields of temperature, the mixing ratio of water vapor and winds were then interpolated onto the σ coordinate.

As mentioned in the Introduction, the initial large-scale flow pattern for this study should resemble the basic structure of a summertime subtropical high over the central and eastern States and the west Atlantic Ocean. No baroclinic systems should be present. In addition, the initial condition should provide a favorable environment where a midlevel mesovortex could be generated.

The initial sea level pressure (SLP) over the coarse mesh domain (Fig. 4.2a) represents the typical pattern of the subtropical high during the summer. The locations of land and ocean are also indicated. The midlevel geopotential height and

temperature fields (Fig. 4.2b) indicate no phase difference between the dynamic field and the thermodynamic field. Therefore, the large-scale flow pattern is near equivalent barotropic with weak vertical wind shear and small horizontal temperature gradient.

The sounding shown in Fig. 4.2c is taken at the location denoted by the symbol "x" in Fig. 4.2a, and is similar to that used in an idealized simulation of extratropical MCSs by Chen (1990). The sounding is representative of the composite pre-MCS environment in the central U.S. at 0000 UTC. The values of the convective available potential energy (CAPE) over this area is between 2000-2500 J/kg.

Considering the time scale of the transformation of a mesovortex into a tropical cyclone, the model should be integrated for at least 72 hours. During the long time integration, it is desirable to maintain a stable large-scale flow configuration to allow the mesovortex to move to the 'right place' at the 'right' time. To achieve this, analysis nudging terms are applied to the large-scale flow during the first 36 hours. Symbolically, the predictive equation for a variable P(s,t) is written as:

$$\frac{\partial P}{\partial t} = F(s,t) + \alpha \cdot W(s,t) \cdot (P_0 - P) \qquad (4.1)$$

where s represents the independent spatial variables and t is time; F denotes all the model advection terms and forcing terms; and P_0 is a reference state for the predictive

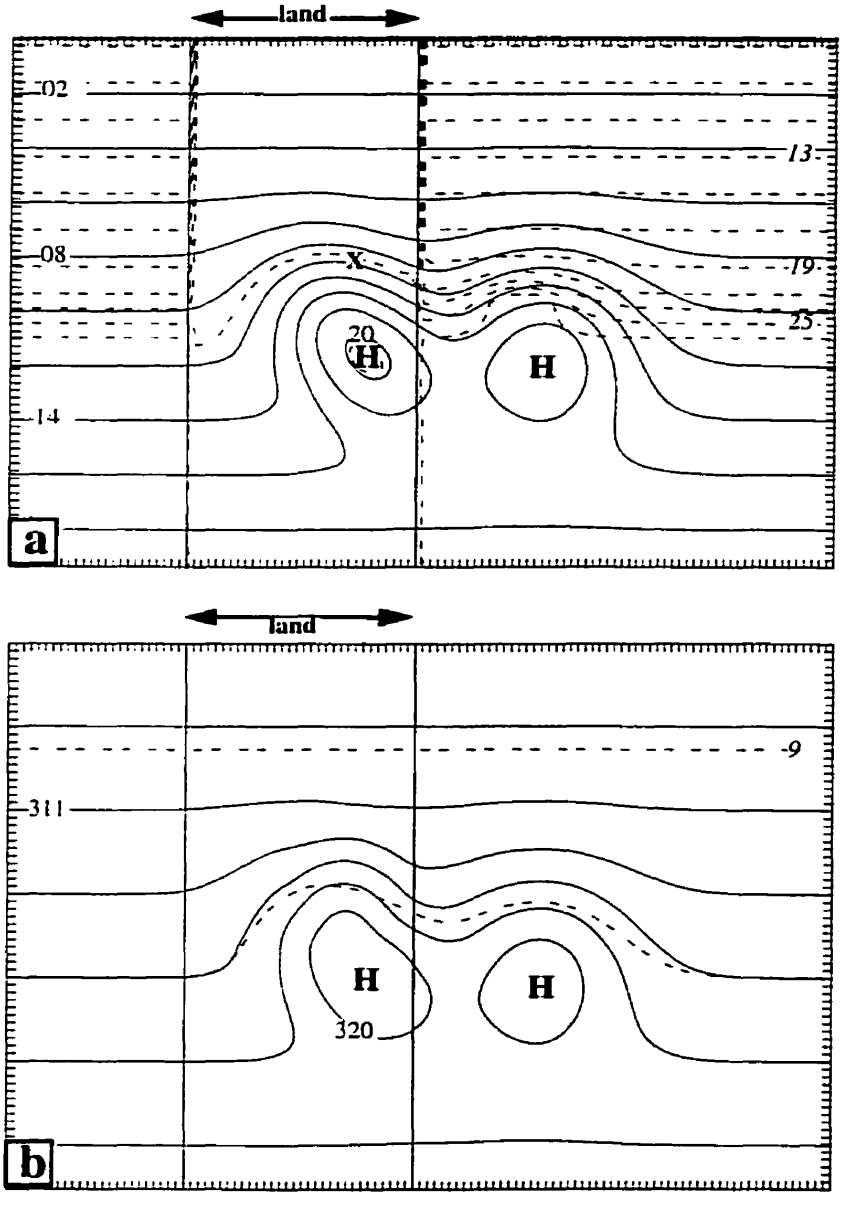

Fig. 4.2 Model initial conditions over the coarse-mesh domain: (a) sea-level pressure (solid) at interval of 2 hPa and sea-surface temperature (dashed) at intervals of 2°C; (b) geopotential height (solid) at intervals of 30 dam and temperature (dashed) at intervals of 1°C at 700 hPa; (c) A sounding taken at the center of the initial convective area, i.e. "X" in (a), with full barb 5 m s^{-1}; and (d) the distribution of weight function used in analysis nudging at intervals of 0.3.

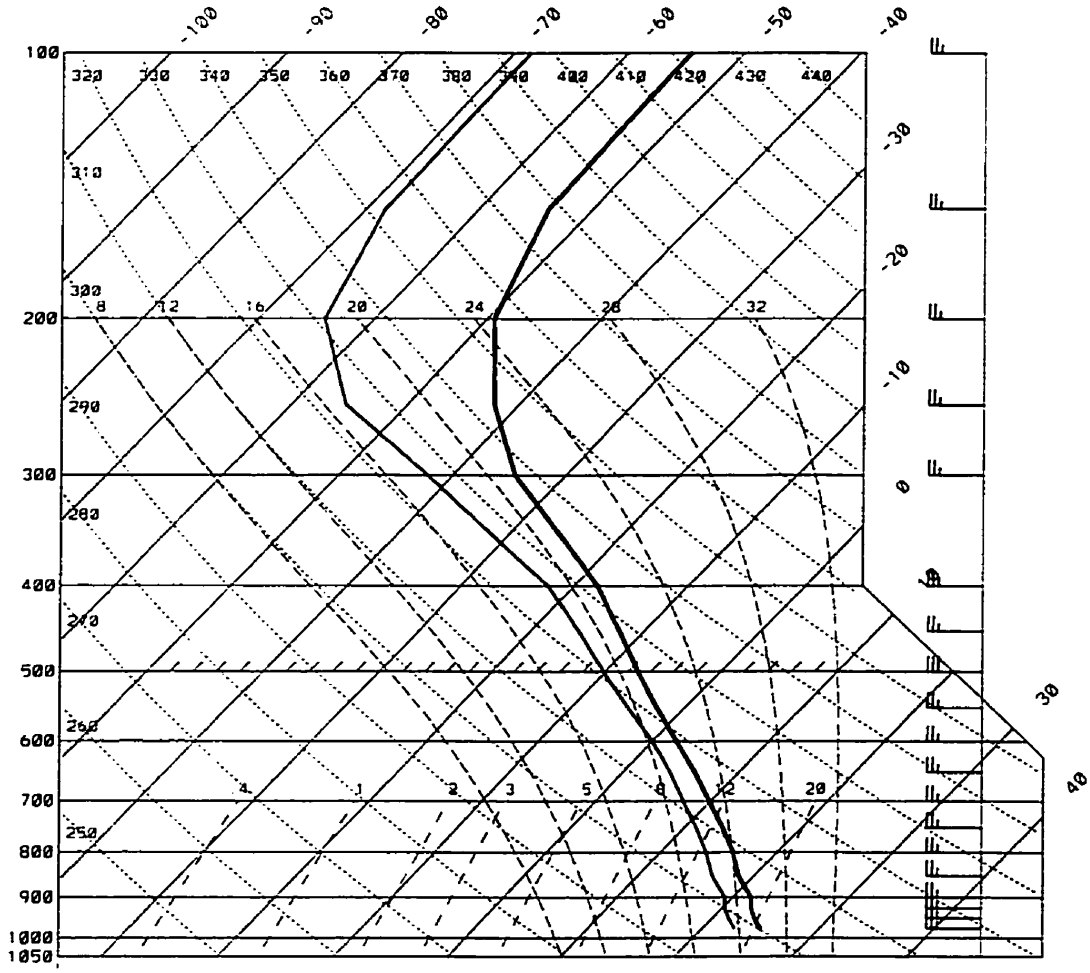

C

Fig. 4.2 (continued)

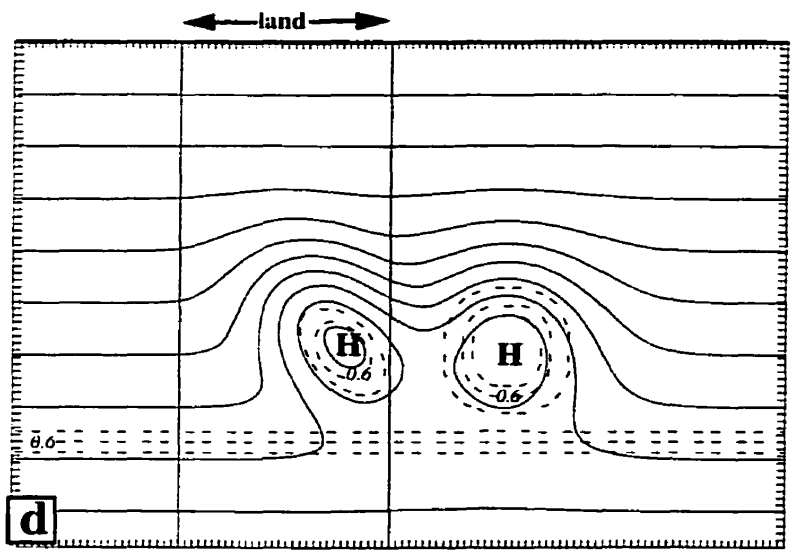

Fig. 4.2 (continued)

variables. The nudging factor α determines the magnitude of the nudging term relative to all other model processes in F. Since it is artificial, it should not be a dominant term in the governing equations. Typically, its magnitude should be compatible to that found in the slowest adjustment process like inertial effects. A reasonable range is from 10^{-4} s^{-1} to 10^{-3} s^{-1}. W is a four-dimensional weighting function for the horizontal, vertical and time weights. Fig. 4.2d shows that the weighting function has a maximum value of 1.0 at the two high centers and decreases to zero in areas where the mesovortex initially formed and moved. Consequently, the nudging term should not have strong impact on the development and evolution of the mesovortex.

4.3. Results

Based on the aforementioned initial conditions, a 72 h integration was performed. The evolution of sea-level pressure (SLP), convective precipitation and grid-scale precipitation, vertical relative vorticity and the development of a warm-core tropical cyclone will be examined in the following sections.

4.3.1 The evolution of SLP

During the first 8 minutes, deep convection was initialed by temperature perturbation of δT=5.0 C° in the K-F CPS within a 200 km x 200 km area. In real situation, such forcing could be caused by either a mid-level short wave trough or by orography. Once convection was triggered, the temperature perturbation was turned off. After 12 hours of persistent convection, the model generates a typical mesovortex

which exhibits a warm core above and a cold pool below. At 24 h, the mesoscale surface trough just moves offshore and all convection over land dissipates (Fig. 4.3a). Note that the convection occurs at small isolated points instead of over a broad area. During the next 10 hours, the system exhibits very little convective activity (Fig. 4.4c). By 36 hr, the meso-trough moves close to the subtropical high. Their interaction leads to the formation of a confluent zone over the warm water. This zone is favorable for the outbreak of new convection because it is associated with large upward fluxes of heat and moisture in the presence of strong surface wind.

Fig. 4.3b indicates a northeast-southwest oriented convection band, which marks the beginning of a new convective phase. The surface system does not show features of rapid deepening until 60 h when the first closed contour in SLP associated with the mesolow appears (Fig. 4.3c). The convective band over the warm water also becomes more organized and develops an eye-like structure. It is believed the strong low-level convergence, driven by convection, increased the surface wind, which in turn enhances the upward surface flux to destabilize the low-level environment. The destabilization may favor the generation of new convection to form a positive feedback process to sustain persistent convection and the rapid development of a tropical storm.

Fig. 4.3d shows that the SLP has deepened 4 mb during the last 12 hours with a rate comparable to that found in the RDS. The vortex circulation tends to wrap around

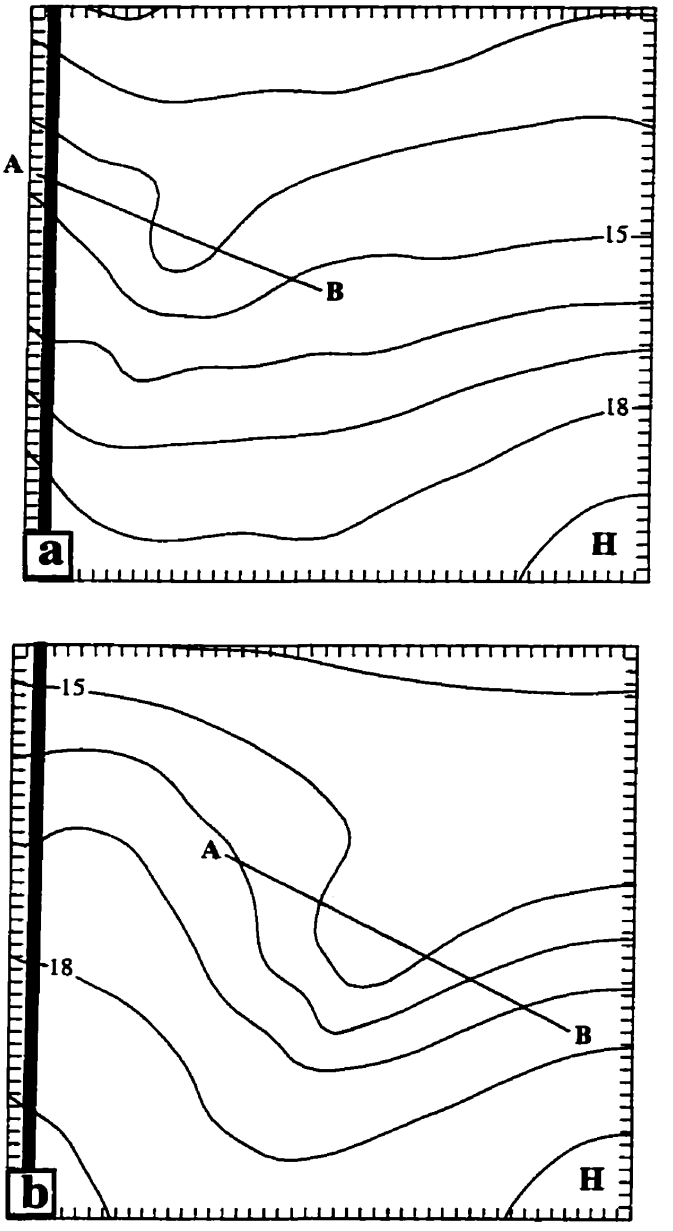

Fig. 4.3 Sea-level pressure (solid, every 1 hPa), superposed with the convective area (shaded) from (a) 24 h; (b) 36 h; (c) 60 h; and (d) 72 h simulation. Line AB represents the location of vertical cross section used in Fig. 4.10. Letters, "H", "L", denote the local maximum and minimum of sea level pressures. The model coastal line is shown by a thick solid line.

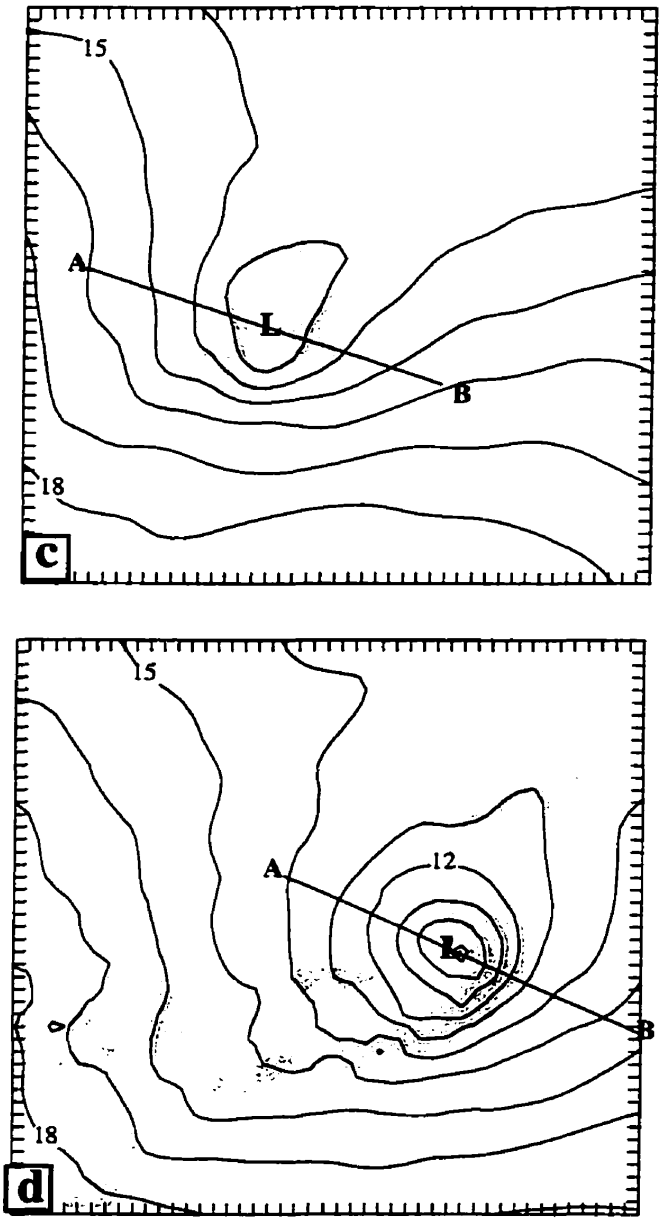

Fig. 4.3 (continued)

the leading portion of the convective band toward the northwest. The maximum surface wind is located to the southeast of the low center. Its value of about 18 m s^{-1} (not shown) marks the end of the genesis stage of a tropical cyclone (Zehr,1992).

4.3.2 Convective and grid-scale precipitation

Following the same methodology as in the RDS, the evolution of deep convective and grid-scale precipitation are examined during the life cycle of the cyclogenesis.

Figs. 4.4a-b show the first 24 h accumulated convective rainfall and grid-scale rainfall. The precipitation occurs mostly over land and is associated with the initial generation of the mesovortex. Both the convective and the grid-scale precipitation indicate two maxima. The one to the north is located over the area where convection initiates during the first 12 hours. Since the initial convection is triggered in a nearly saturated environment, the grid-scale rainfall forms after a couple of hours. The ratio of grid-scale rainfall to the total precipitation is about 50% (Fig. 4.4b), and may be regarded as a reasonable ratio. When the system moves to the coast, new convection is generated as a result of the interaction between the circulation of the mesovortex and the land-sea thermal contrasts during the early afternoon hours. The new convection is responsible for the second precipitation band shown in Figs. 4a,b.

After 24 h, the mesovortex system moves offshore. The system goes through a 10 hours period during which convection is not active. Both the areal coverage and the intensity of the accumulated convective precipitation become very small (Fig.

4.4c), so is the amount of grid-scale rainfall (Fig. 4.4d). The reasons for the negligible amount of convection is attributable to the cold SST which renders the environment less favorable for convection. Also the large scale flow surrounding the mesovortex does not provide favorable forcing until 36 h when the mesovortex moved closer to the subtropical high over the ocean.

After 36 h, new convection breaks out signaling the beginning of the oceanic storm. During the following 36 hours, the convective activity could be divided into two phases. Figs. 4.4e-f show the first phase, from 36 to 54 h, when the convection is distributed along a northeast-southwest oriented band whose location coincides with the aforementioned confluent zone. During this period, convection is just initiated and it gradually intensified. Figs. 4.4g-h indicate that the areal coverage and intensity of the convection increase dramatically during the second phase (from 54 to 72 h) as the tropical storm develops rapidly. It is of interest to note that little grid-scale rainfall is produced during the last 36 hours because the middle to upper troposphere is very dry under the persistent influence of the subtropical high. Therefore, convective forcing alone contributes directly to the spin-up of the tropical storm.

4.3.3 The evolution of midlevel and low-level vorticity

In the RDS, the mid-level mesoscale convective vortex (MCV), which is generated over land, plays an important role in the organization of the oceanic storm.

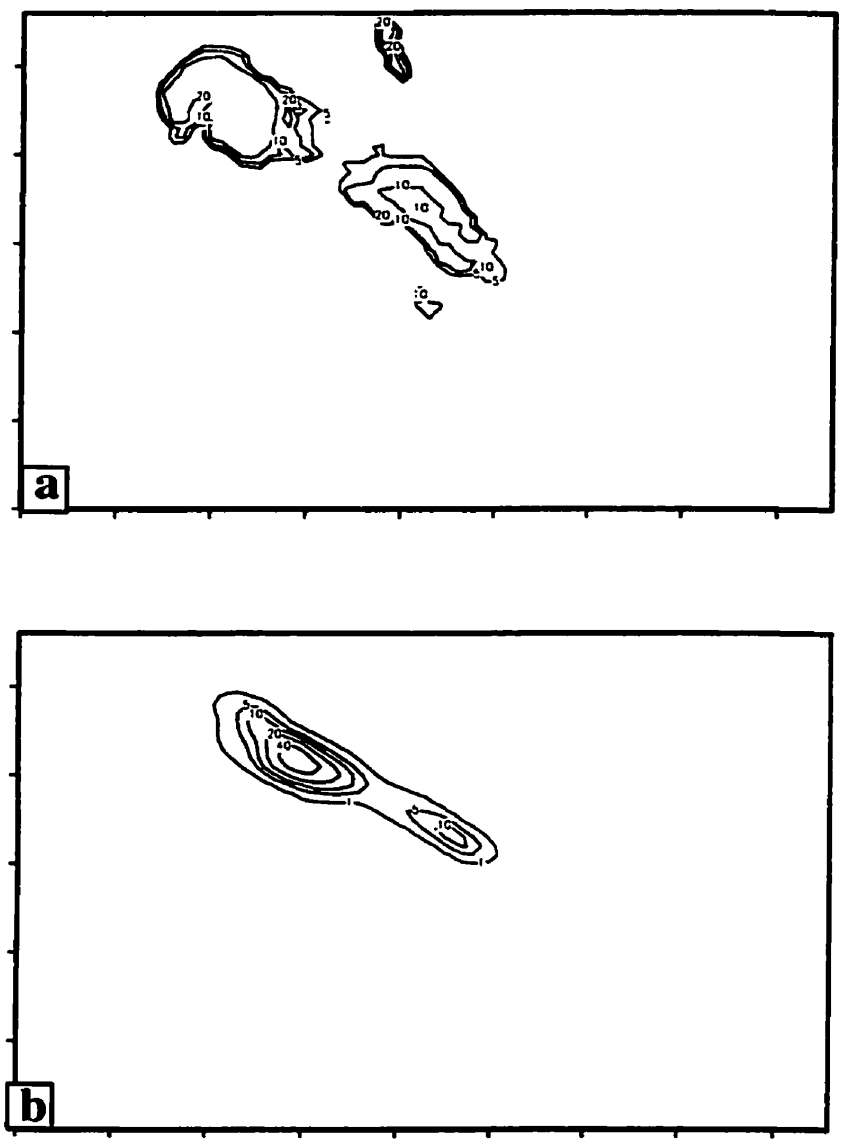

Fig. 4.4 The model-produced accumulated convective (top) panel and grid-scale (bottom panel) rainfall (mm) during (a-b) 0-24 h; (c-d) 24-34 h; (e-f) 34-54 h; (g-h) 54-72 h. The contours for convective rainfall are 5,10,40,80,160,320. The contours for grid-scale rainfall are 1,5,10,40,80,160,320.

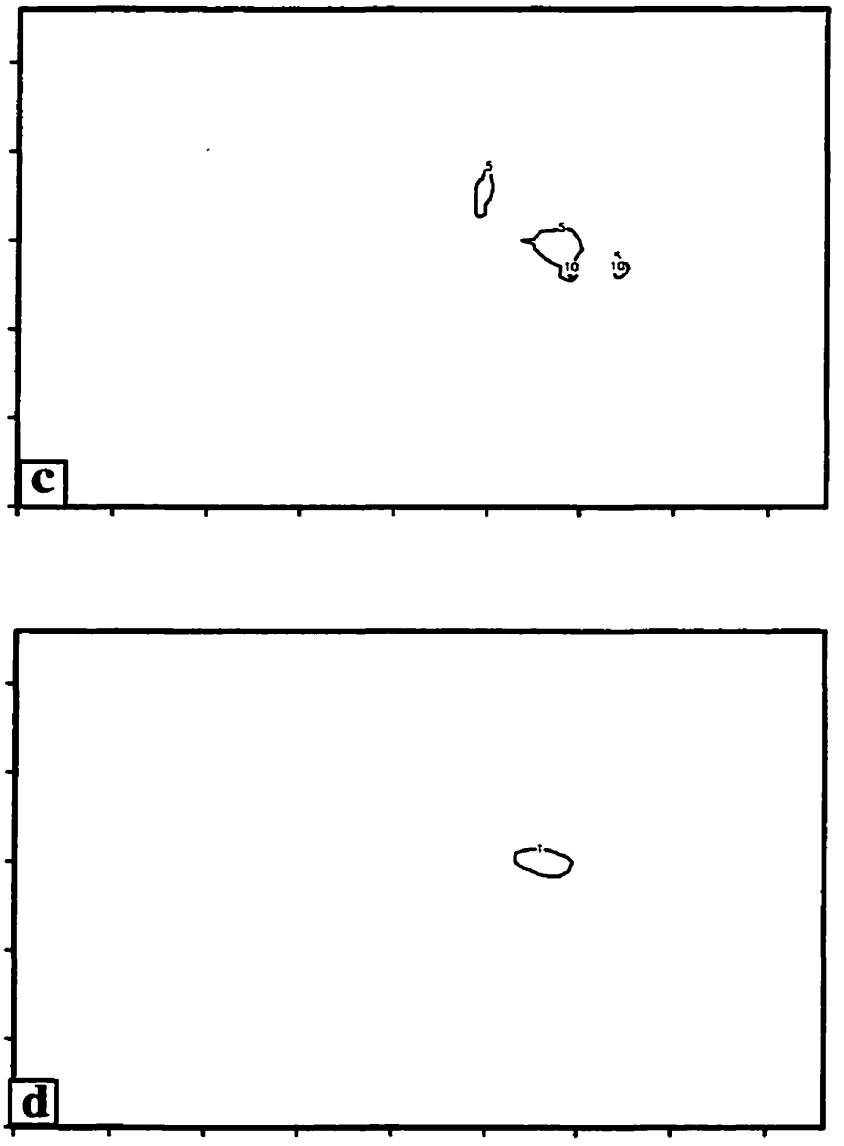

Fig. 4.4 (continued)

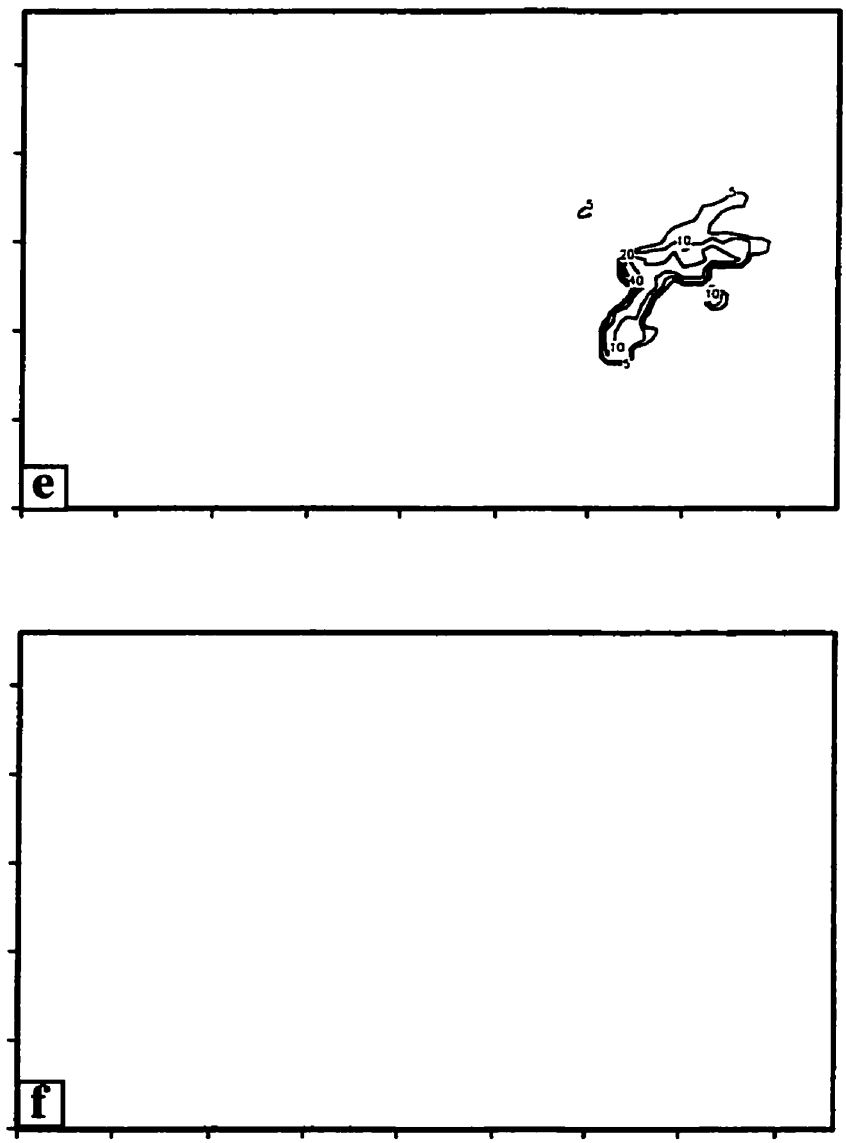

Fig. 4.4 (continued)

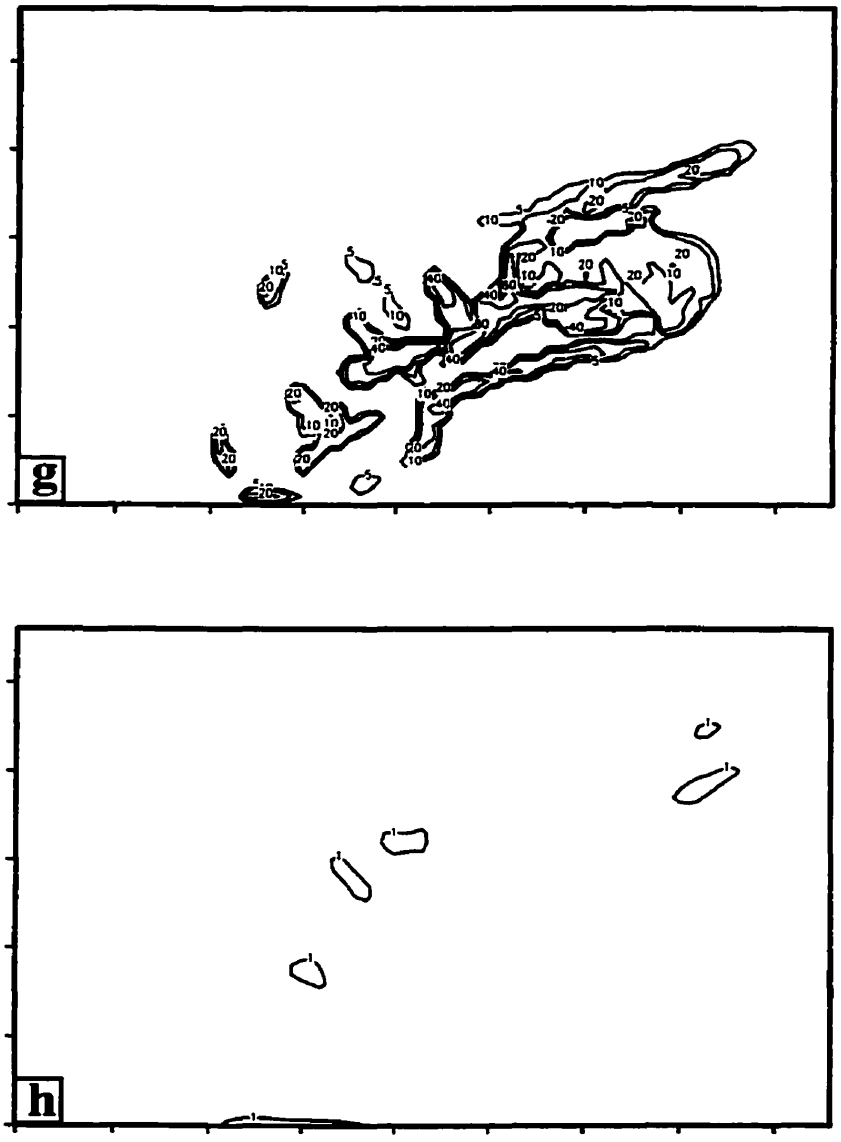

Fig. 4.4 (continued)

Specifically, after moving offshore, the MCV dissipates but triggers an oceanic storm in front. The associated maximum vorticity is located at low levels, a feature commonly found in tropical storms (Frank, 1977). As the storm matures, the system intensifies again. The structure of the vertical relative vorticity at 700 hPa is characteristic of a continental vortex while at 950 hPa it bears the signature of a tropical storm. It would be of interest to see if similar features can be found in our idealized simulation.

Fig. 4.5 shows the evolution of the maximum relative vorticity associated with the idealized mesovortex at 700 hPa and 950 hPa during the final 48 h. From 24 to 36 h, the vorticity at both levels decreases. Convection is inactive in this time interval and the mesovortex is dissipating. After 36 h, the low-level vorticity starts to increase because new convection is triggered in the southwesterly flow of the mesovortex over the ocean. In contrast, the midlevel vorticity further decreases slightly until 60 h. During the 36-60 h period, the oceanic storm slowly organizes itself and spins up. The increase of the low-level vorticity and the slight decrease of the midlevel vorticity signal a low-level development of the new vortex system characteristic of tropical systems. Obviously, this period can be regarded as a transition from a continental vortex to a tropical system. After 60 h, the vorticity at both levels increase simultaneously. This time marks the end of the transition period and the beginning of the rapid deepening phase of the tropical storm.

The evolution of the mesovortex will now be examined in terms of the 700 hPa relative vorticity and 700 hPa wind field at 24, 36, and 72 h. At 24 h, Fig. 4.6a shows

a concentrated vorticity pattern with closed circulations. The size and intensity of the mesovortex are comparable to those in the RDS. The vortex is embedded in the anticyclonic flow of the subtropical high over land. Twelve hours later, the intensity of the vortex has weakened by more than 20% (see Fig. 4.6b) and its circulation starts to interact with the south-westerly flow of the subtropical high over the ocean. Such confluence may provide dynamic forcing to generate new convection ahead of the vortex. Fig. 4.6c indicates that the vortex regains the intensity at 72 h. The increased vorticity at this level may result from the vertical advection of vorticity from low levels (see Fig. 4.11b) because the transformation of the continental vortex into a tropical storm was already complete prior to this time.

To analyze the growth of the 950 hPa relative vorticity after 36 h (Fig. 4.5), we further decomposed the vorticity in natural coordinate (n,s) into its shear component ($-\frac{\partial V}{\partial n}$) and curvature component ($V\frac{\partial \alpha}{\partial s}$) following Bell et al. (1993). Mathematically, we write

$$-\frac{\partial V}{\partial n} = -\frac{1}{V^2}\left[u^2 u_y - v^2 v_x - uv\,(u_x - v_y)\right]$$

$$V\frac{\partial \alpha}{\partial s} = \frac{1}{V^2}\left[u^2 v_x - v^2 u_y - uv\,(u_x - v_y)\right]$$

where V is the wind speed, and u and v are respectively the x and y components of the wind velocity.

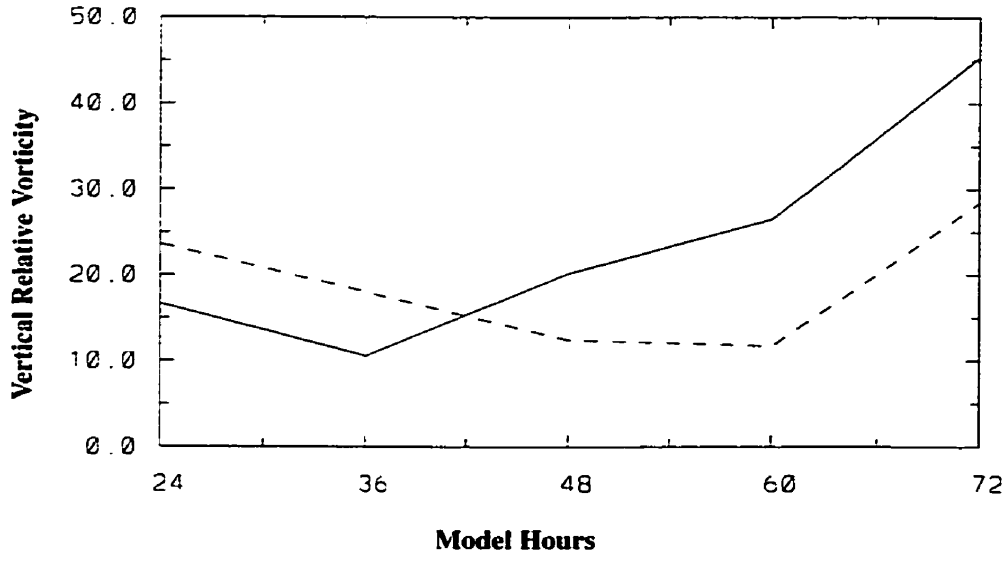

Fig. 4.5 The time evolution of the local maximum vertical relative vorticity (10^{-5} s^{-1}) at 700 hPa (dashed) and 950 hPa (solid) from 24 to 72 h integration.

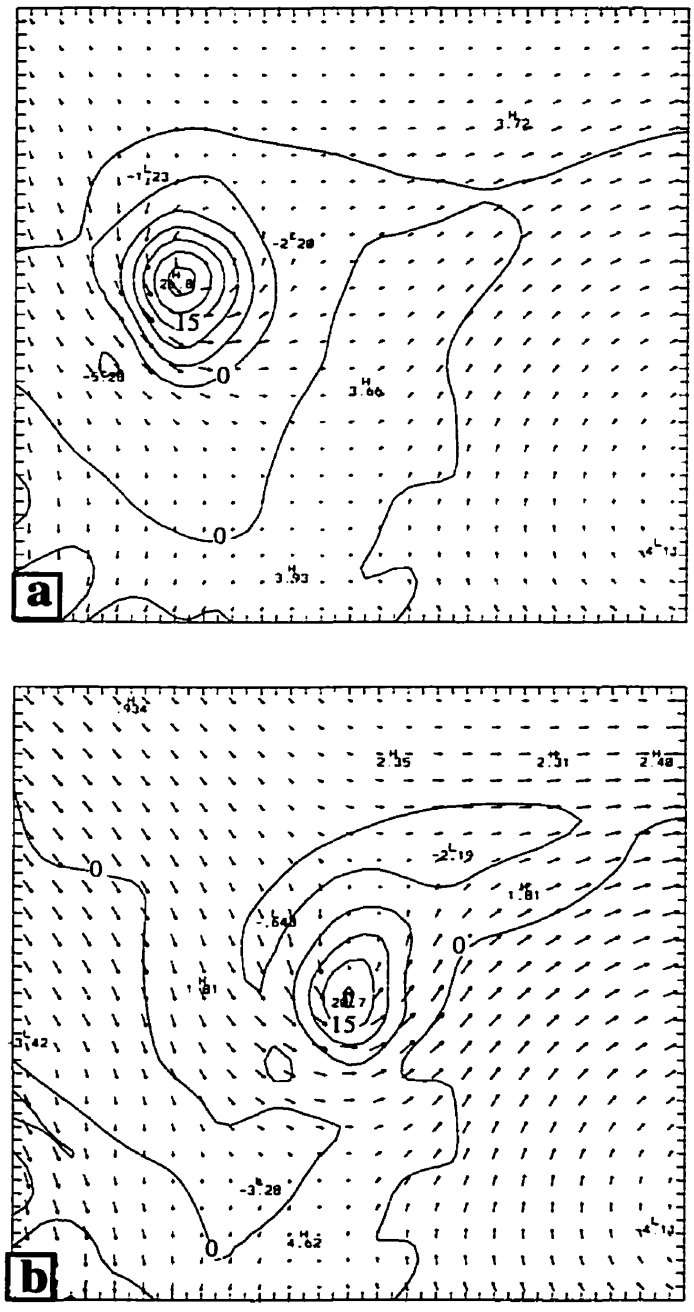

Fig. 4.6 Horizontal distribution of the vertical relative vorticity (every 5×10^{-5} s^{-1}) superposed with horizontal wind vectors from (a) 24 h; (b) 36 h; and (c) 72 h integration.

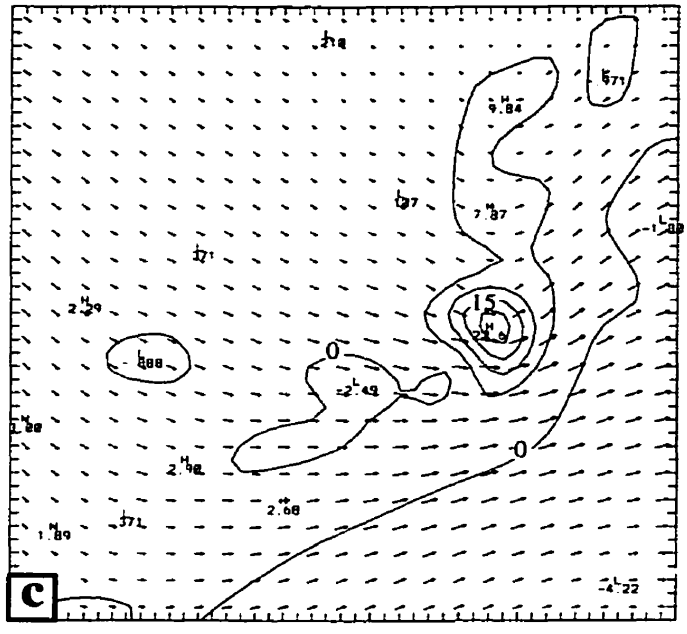

Fig. 4.6 (continued)

In Figs 4.7-4.9, we show the 950 hPa relative vorticity superimposed on the 950 hPa wind (top panels) and the curvature and shear vorticity components superimposed on the divergence field (bottom panels).

At 36 h, the relative vorticity is in the shape of a circular vortex with a northeast-southwest oriented vorticity band (Fig. 4.7a). The former is mainly associated with the remnant of the continental mesovortex, while the latter is associated with the new convection ahead of the mesovortex. Note that the curvature vorticity dominates over the shear vorticity, in terms of both areal coverage and intensity (Fig. 4.7b). This is true even in the vorticity band where shear vorticity occupies just a small area to the north of the vortex. The convergence zone, generated by the interaction of the mesovortex and the subtropical high, is in phase with the northeast-southwest oriented curvature vorticity band. In contrast, only a very small portion of shear vorticity overlaps the convergence zone. Thus, the increase of the vorticity through vortex stretching favors its curvature component.

By 60 h, the intensity of vorticity has doubled in the last 24 h (Fig. 4.8a). Again, the curvature vorticity constitutes the dominant component (Fig. 4.8b). The shear vorticity is still concentrated to the north of the vortex, but with larger areal coverage and stronger intensity than at 36 h. A region of strong convergence lies along the tail portion of the curvature vorticity. The shear vorticity on the eastern side of the vortex is also collocated with the convergence zone. It can be expected that the vortex would intensify significantly in its leading northeastern portion as a result of the combined contribution from the curvature and shear vorticities. Furthermore, the tail region of

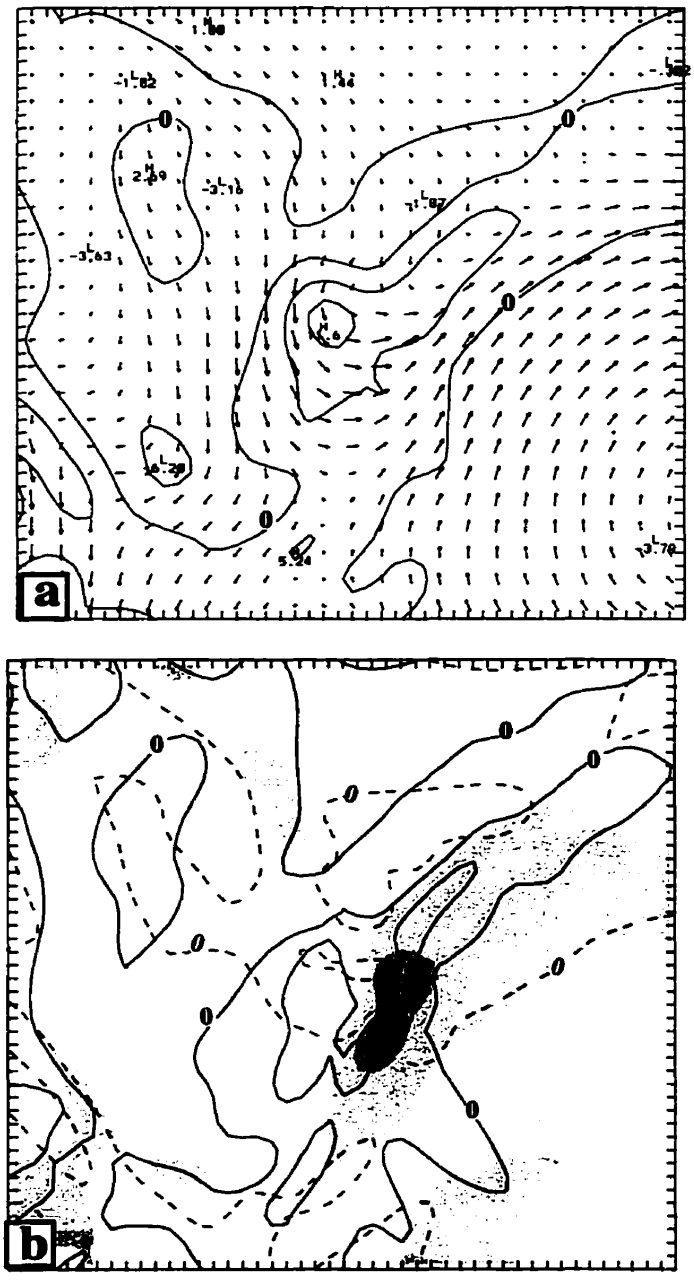

Fig. 4.7 (a) The 950 hPa winds plotted at every other grid point and the vertical relative vorticity (every 5×10^{-5} s^{-1}) from 36 h integration (b) the curvature vorticity (solid) and shear vorticity (dashed) contoured at 5×10^{-5} s^{-1}; superposed with areas of convergence (shaded at -3×10^{-5} s^{-1} and -6×10^{-5} s^{-1})

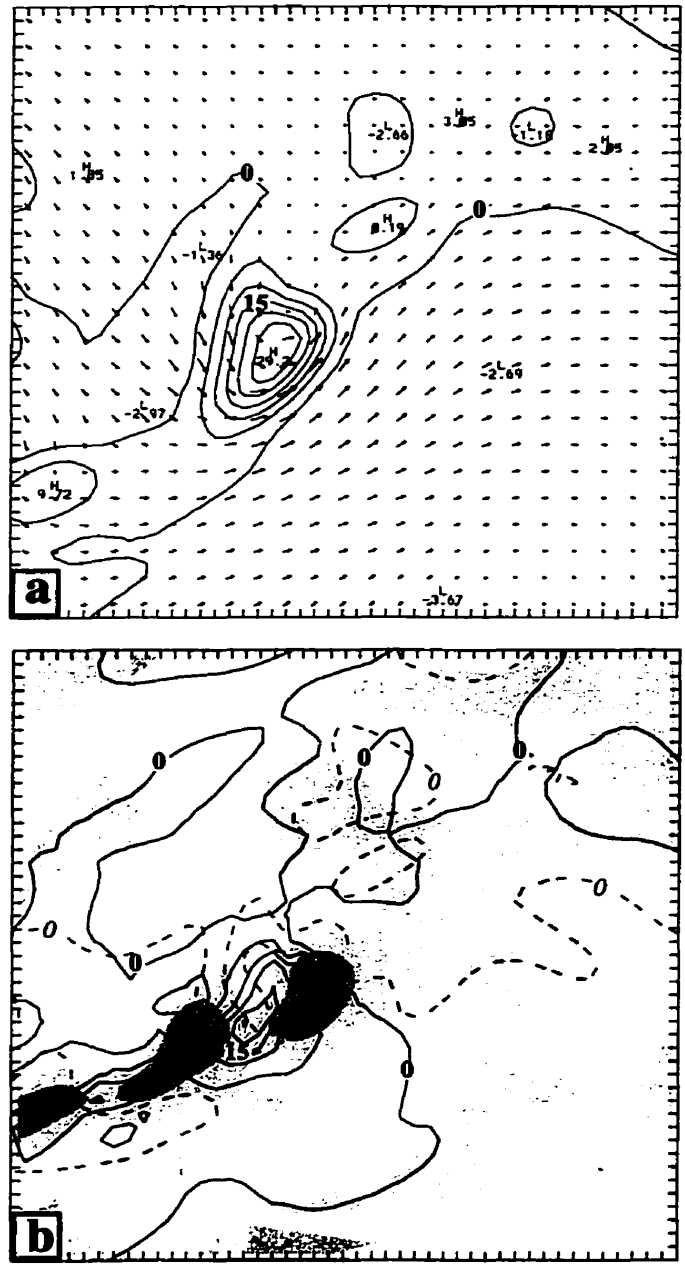

Fig. 4.8 As Fig. 4.7, but from 60 h integration.

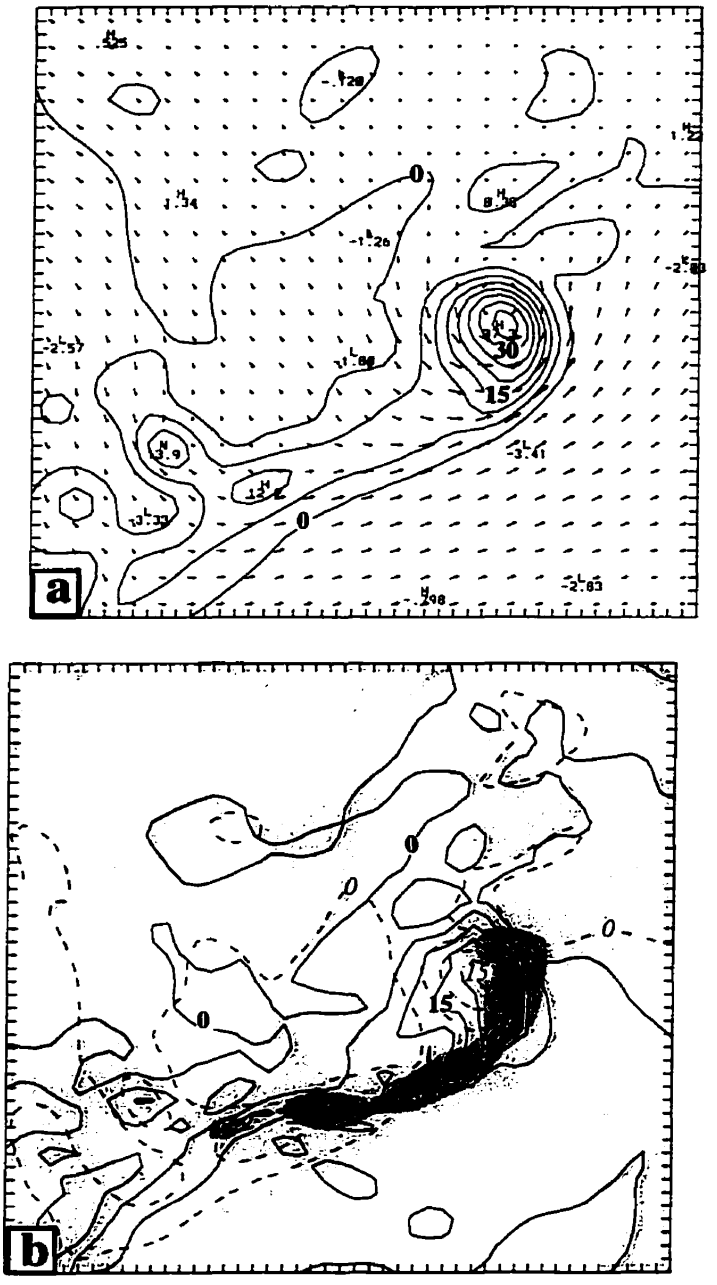

Fig. 4.9 As Fig. 4.7, but from 72 h integration.

the vortex also should intensify due to the phase lock between low-level convergence and curvature vorticity.

At 72 h, the vortex is well developed with closed circulations (Fig. 4.9a). The gradient is stronger along its leading edge due to vortex stretching associated with persistent convection. Similar to the vorticity pattern at 60 h, the area of most intense convection is located to the northeast of the vortex. The intensity of the northeast-southwest oriented tail band also increased. Note that the contribution of shear vorticity has increased (Fig. 4.9b), as judged from the large areal coverage and strong intensity.

The evolution of the vortex at 950 hPa indicates some features different from those in the RDS. In the present case, the curvature vorticity through stretching takes a leading role during the initial 24 hours in the amplification of the low-level vortex and the northeast-southwest oriented tail. The influence by the increasing shear vorticity on the growing vortex would mainly be reflected by the stronger gradient of total relative vorticity to the northeast of the vortex. In the RDS, the northeast-southwest oriented vorticity band is characterized by shear vorticity generated by persistent convection. The orientation of the band, advected by the northwesterly prefrontal flow, gradually takes on a north-south orientation. The shear vorticity is then advected inward and converted to curvature vorticity. By comparing the large-scale flow in both cases, it was found that the scale of cyclonic flow (meso-α scale) in the RDS, controlled by both the prefrontal flow and subtropical high, is larger than

the idealized case whose cyclonic circulation is more localized and is less affected by the large-scale flow.

4.3.4 Vertical structure

The cross sections of relative vorticity, and deviation temperature from its pressure level averages along the line A-B (see Fig. 4.3) at 24, 36 and 72 h are presented in Figs. 4.10a-c.

At 24 h, the model reproduces very well the vertical structure of the typical mesovortex generated by a land-based MCC as was demonstrated in the RDS. The maximum vorticity is near 650 hPa (Fig. 4.10a). A warm core lies above and a cold pool is situated below. Such a thermal couplet has been extensively studied in numerical simulations of continental MCSs by Zhang et al (1987; 1988; 1989) and Chen (1990), as well as observational analyses by Fritsch et al (1994) and Bister et al (1997). Because of the direct evidence of the transformation of a cold pool vortex to Hurricane Guillermo found during TEXMEX, there is increasing interest to investigate the processes involved in such transformation. Obviously, as a first step, it is important to simulate properly such a vortex.

The mechanism responsible for the formation of the thermal couplet presented here is the same as reported in Zhang et al (1987), where the midlevel warm core is produced by parameterized and grid-scale latent heating while the low-level cold pool is contributed by downdrafts and evaporative cooling. Note that the intensity and the structure shown in Fig. 4.10a are quite similar to those obtained in the RDS, although

the present MCS starts from an idealized initial condition which is representative of the typical summertime environment over the central U.S. The weak vertical wind shear in the large-scale flow helps to maintain the coherent vertical structure until 24 h.

By 36 h, the intensity of the vorticity associated with the MCV weakens significantly (Fig. 4.10b). During the time period from 24 to 36 h, convective activity was almost absent. Fritsch et al (1994) and Harr et al (1996) suggested that to maintain the intensity of the MCV, persistent organized convection and weak vertical wind shear are essential. On the other hand, the signature of the MCV can still be identified. Fig. 4.10b shows another vorticity maximum ahead of the cold pool situated in the lowest 200 hPa. Obviously, the generation of this low-level vorticity entity is closely related to the new convection occurring in the confluent zone indicated in Fig. 4.3b. The appearance of the low-level vorticity entity signals the beginning of the period when the MCV transforms into a tropical storm.

The generation of new vorticity ahead of the MCV indicates that the MCV may not evolve directly into a tropical system. As suggested in the RDS, the MCV acts in an indirect way through the interaction of its circulation with the flow of the subtropical high to provide the mesoscale forcing. In addition, the MCV furnishes the necessary cyclonic vorticity that is stretched along the convectively enhanced confluent zone. The scenario presented here is different from that proposed by Bister et al (1997), in which the breakout of new downdraft-free convection erupts in the center of the cold pool MCV. However, an alternative scenario has been proposed

during the TCM-93 experiment. Specifically, based on satellite imagery, Harr et al (1996) found that the initiation of new convection, leading to the formation of tropical storm Ofelia, lies along the southern portion of the MCV. This convective initiation may be caused by the enhanced low-level confluence that is induced by the interaction of the MCV circulation with the large-scale flow. The imagery also shows that the convection increases with time. The cells on the east move northward on the right side of the MCV and rotate in a cyclonic manner. Although it is still difficult to draw a definite picture of the evolution of the vertical structure of an MCV and its surrounding convection band from satellite-based studies, the case does suggest an alternative picture for the initiation of convection leading to tropical cyclogenesis.

At 72 h, a board relative vorticity band with maximum intensity near the surface is seen in Fig. 4.10c. The increase in both areal coverage and intensity of the band is mainly due to vortex stretching contributed by the persistent convection ahead of the MCV. Unlike the two vorticity bands during the later stages of the cyclone in the RDS, only one vorticity entity developed at 72 h. Recall that in the RDS, it is the strong wrap-around flow, enhanced by the prefrontal flow, that contributes to the generation of the second vorticity entity. Obviously, such mechanism does not exist in this idealized simulation.

A warm core appears in association with the low-level vorticity entity (Fig. 4.10c). Note that the maximum warming is around 800 hPa. The appearance of a warm core is one of the most important features in the formation of a tropical cyclone.

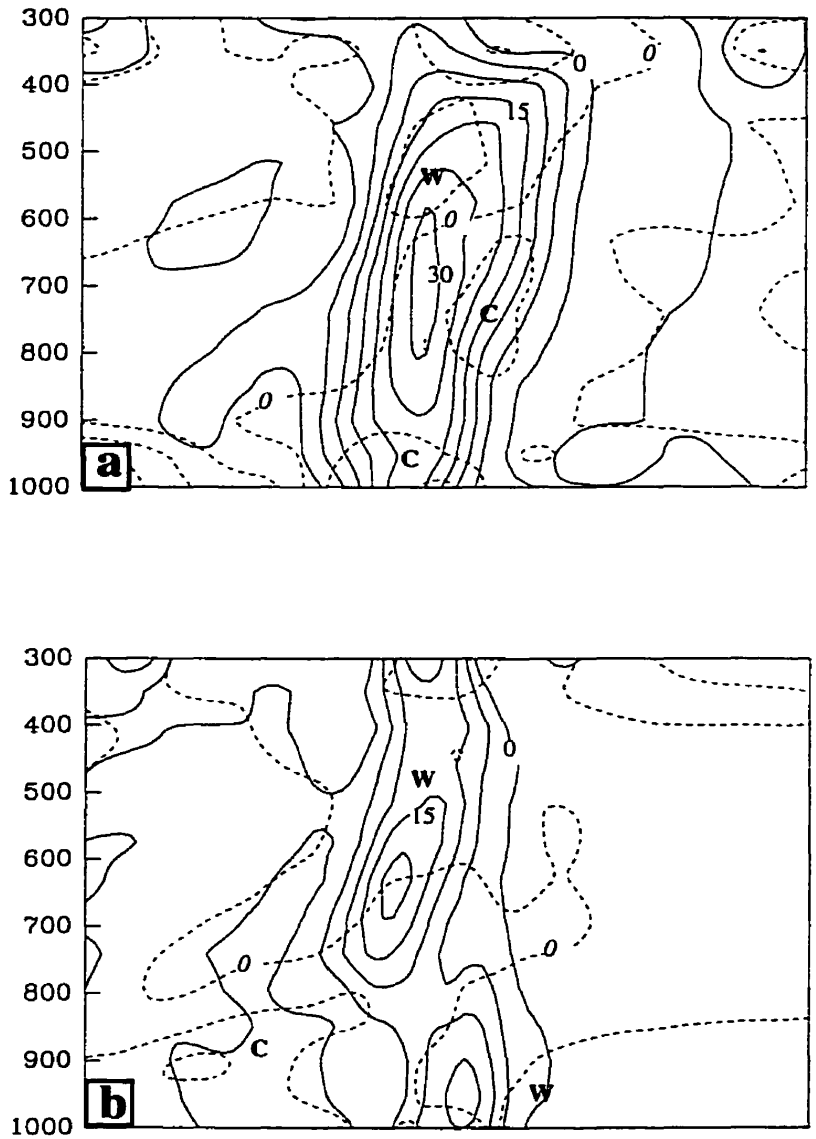

Fig. 4.10 Vertical cross section of the vertical relative vorticity (solid, 5×10^{-5} s^{-1}) and virtual temperature deviation (dashed, every 1°C) from (a) 24 h; (b) 36 h; and (c) 72 h integration.

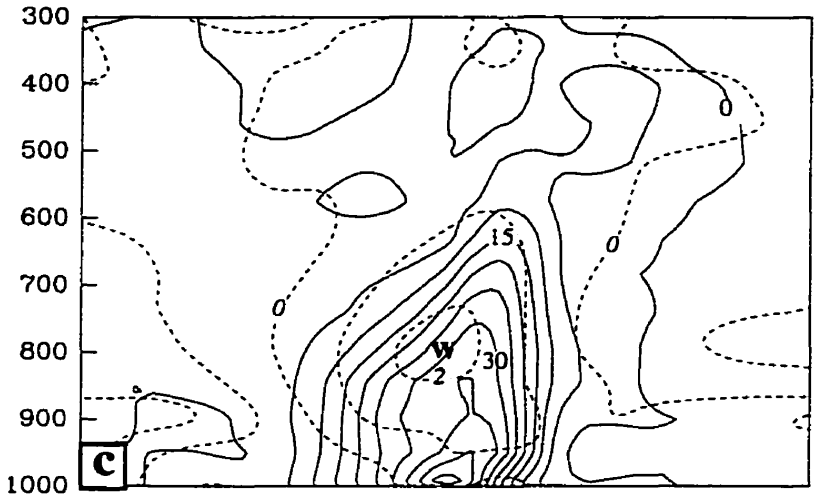

Fig. 4.10 (continued)

We shall discuss in the next section the formation of the warm core and explain why the maximum warming occurs near 800 hPa in the idealized simulation.

4.3.5 Formation of the warm core structure

Fig. 4.5 shows rapid surface development after 60 h. We therefore refer the last 12 hours as the rapid deepening phase. A vertical cross section of deviation temperature at 60 h is given in Fig. 4.11a, which shows a weak warm core with a magnitude of 0.5 K in the area of descent. Note that the descent area is concentrated in the center of the vortex and may be viewed as an eye-like structure surrounded by strong convection towers (Simpson et al., 1997). It is important to know whether the eye-like structure is a persistent feature throughout the deepening phase or just a transient feature.

Using the two-hourly model output, we computed the averaged vertical velocity at the center of the surface low for the last 12 hours of integration. Fig. 4.12 indicates that the descending motion occupies a deep layer from 950 to 300 hPa. The maximum subsidence is around 800 hPa with a magnitude of about 3 cm s^{-1}. Since the profile reflects the average state at the center of the system during the rapid deepening phase, the accumulating heating effect by the small but persistent downward motion may contribute to the formation of a warm core. To assess the heating effect in detail, a potential temperature budget analysis is performed.

For the budget computation, three factors are considered. First, the analysis is performed on a sub-domain with a radius of 200 km centered on the surface low

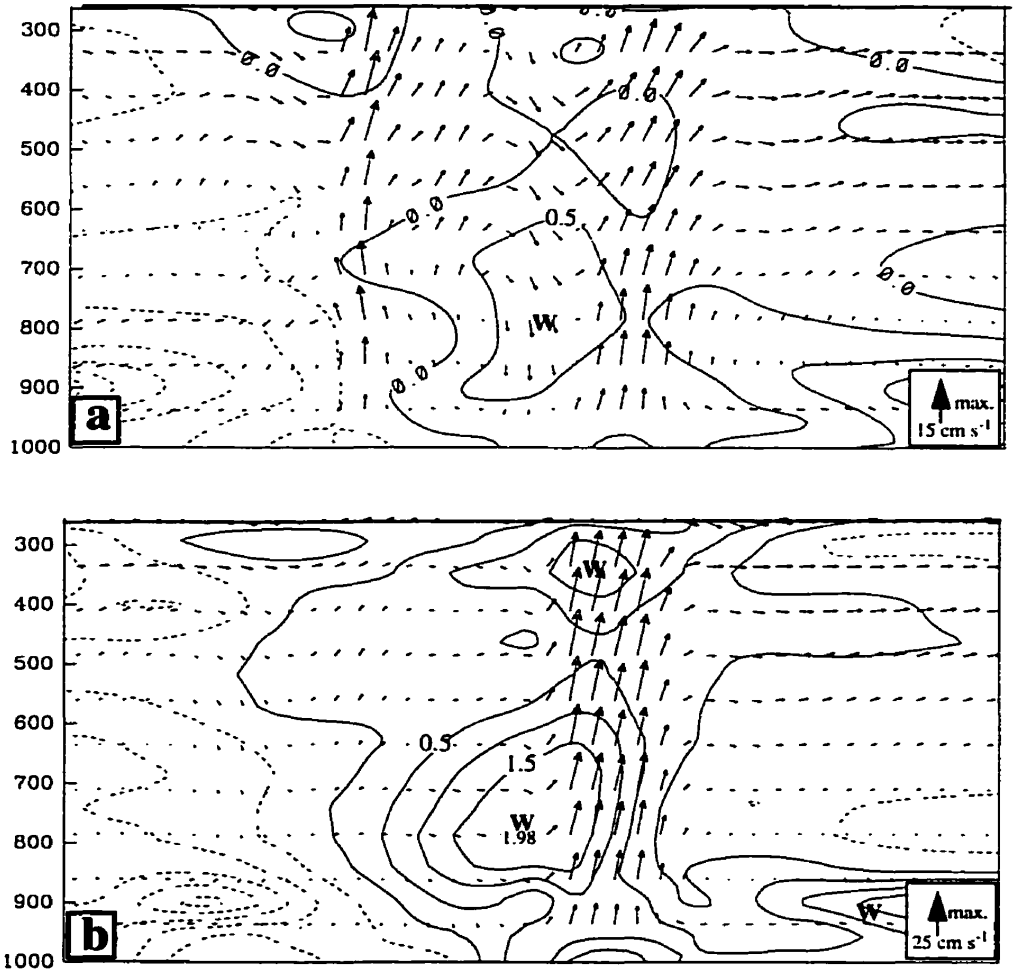

Fig. 4.11 Vertical cross section of deviation temperature (solid, every 0.5°C) from (a) 60 h, and (b) 72 h integration. The letter "W" denotes local warm core.

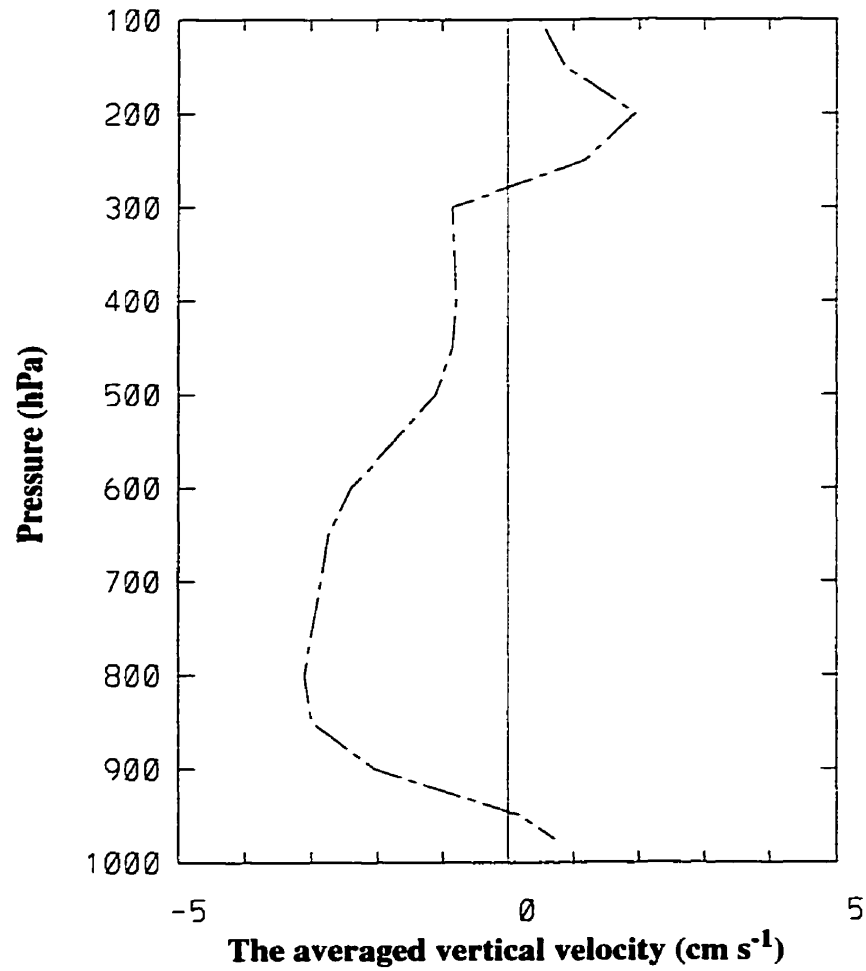

Fig. 4.12 The averaged vertical velocity (cm s^{-1}) at the center of the surface low during the last 12 h integration (i.e., from 60 h to 72 h) simulation.

because our primary focus is in the core area. Second, the budget calculation is performed on the instantaneous dataset every two hours and the terms are then time-averaged on a moving sub-domain over the last 12 hours. The reason for the time averaging is to enhance the signal of warming by the relatively weak downward motion. Even though this warming is much smaller than the heating by cumulus convection at any given instant, the fact that the eye-like structure is relatively stable in a moving sub-domain while convection does not remain in a fixed location would help the detection of the warming effect in the core region by time averaging. Third, the budget calculation is performed at 800 hPa because both Fig. 4.11a and Fig. 4.11b indicate that the maximum warming occurs around this pressure level.

The prognostic θ equation in isobaric coordinates is

$$\frac{\delta\theta}{\delta\tau} = \overline{-V_{rel}\cdot\nabla\theta} - \overline{\omega\frac{\partial\theta}{\partial p}} + \overline{\frac{\partial\theta}{\partial t}|_{pbl}} + \overline{\frac{\partial\theta}{\partial t}|_{con}} + \overline{\frac{\partial\theta}{\partial t}|_{grid}} + \overline{\frac{\partial\theta}{\partial t}|_{dif}} \qquad (4.2)$$

Note that $\frac{\delta\theta}{\delta\tau}$ is not the local tendency term, but represents the averaged net heating in the core region on the moving sub-domain. Therefore, the horizontal velocity V_{rel} is the flow speed relative to the sub-domain. The overbars represent the time average. The thermodynamic forcing terms are contributed by the PBL mixing, convective heating, grid-scale condensation and numerical diffusive processes.

Figs. 4.13a-f show the contribution of the each term to the net heating at 800 hPa. The contribution by horizontal advection is less than 0.5 degree per hour, in contrast to the budget calculation for the RDS, in which cold advection into the

convective band from the cyclonic northerly flow and the warm advection into the cyclone system from the northeasterly flow contribute more than 0.5 degree per hour. The difference is mainly due to the fact that in the idealized case, the prefrontal northerly flow is absent and the wrapped-round flow is not strong. Note that the convective heating (Fig. 4.13b) is located to the east of the surface low denoted by the symbol "L". Its curved band structure along the leading portion of the system, shown on the time-averaged map, indicates clearly that the eye-like structure is a persistent feature during this period. In the area of the eye, adiabatic warming by the subsiding motion is evident (Fig. 4.13c). On the other hand, adiabatic cooling almost offsets completely the diabatic warming in the region of convection (Figs. 4.13b-c). It should be pointed out that we have smoothed both the convective heating and the vertical advection terms before plotting, which has the effect of reducing the strong gradient near the center. If smoothing had not been applied, the zero contour in both fields should be shifted one grid point eastward and warming in the eye region would occur over a larger area.

The contribution made by the PBL is negligible (Fig. 4.13d) because the 800 hPa level is well above the PBL. The heating effect by grid scale condensation is also small because only a small amount of grid-scale precipitation occurs during the deepening stage (Fig. 4.13e). As a result, the net tendency is mainly determined by the difference between the convective heating term and the vertical advection term. Fig. 4.13f indicates that there is net warming in the center of the domain. The magnitude of around 0.1~0.2 °C per hour is equivalent to a 12 h temperature increase of 1.0~2.0

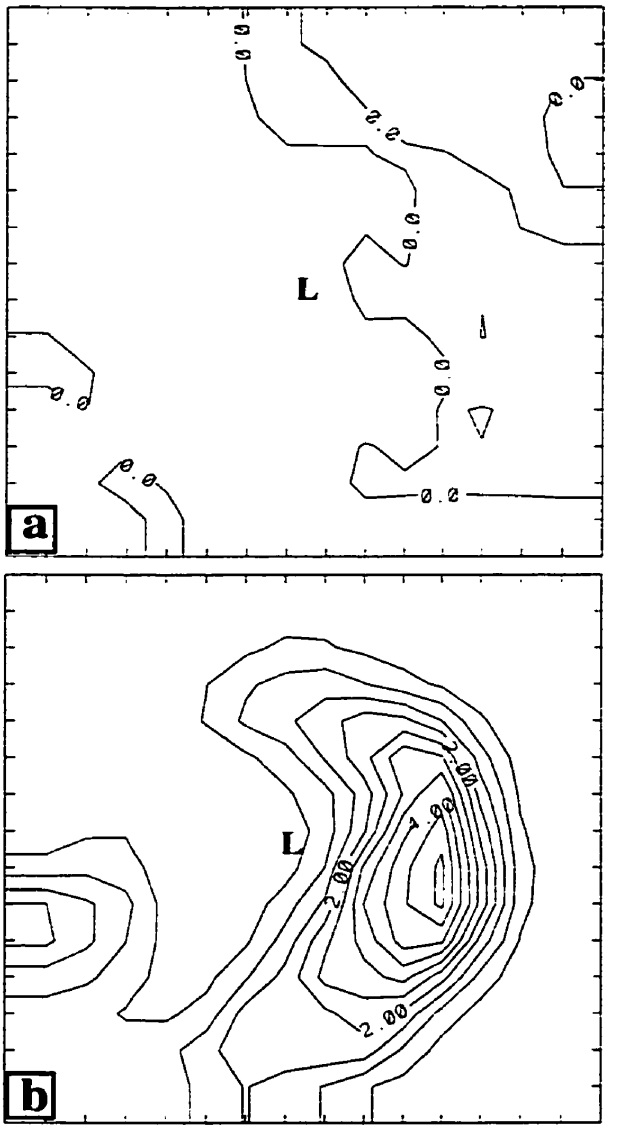

Fig. 4.13 Horizontal maps of the potential temperature budget over a moving subdomain averaged over a period of 12 hours (i.e., from 60 h to 72 h) at 800 hPa. (a) horizontal advection (every 0.5°C); (b) parameterized convection (every 0.5°C); (c) vertical advection (every 0.5°C); (d) boundary-layer mixing (every 0.5°C); (e) grid-scale condensation (every 0.5°C); and (f) net heating (every 0.1°C), "L" indicates the location of the surface low center.

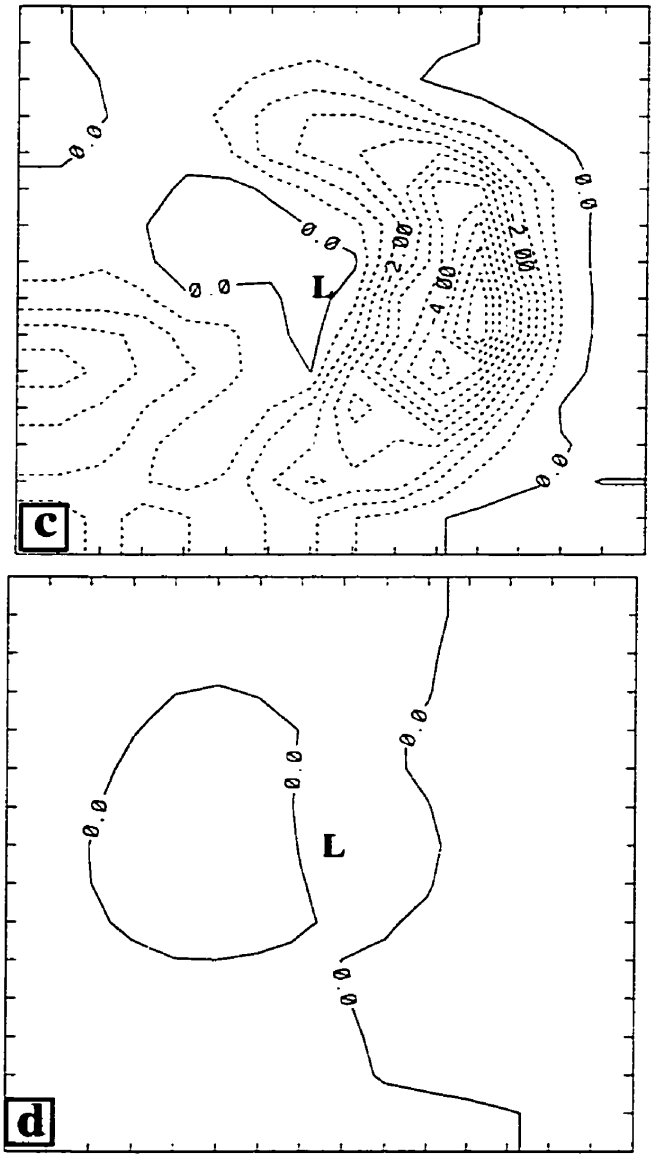

Fig. 4.13 (continued)

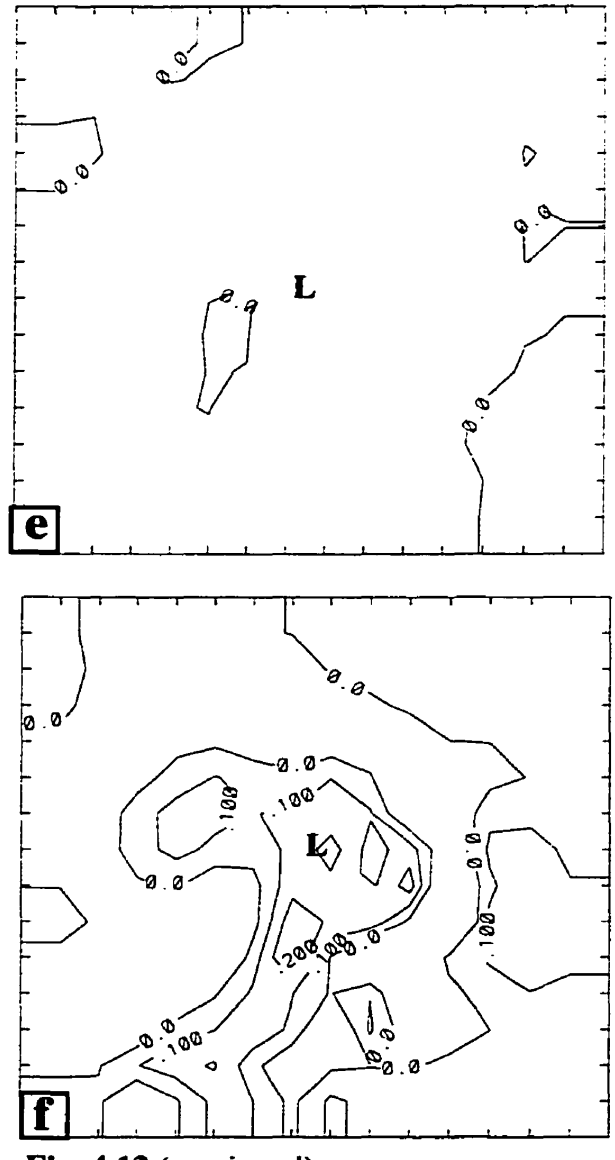

Fig. 4.13 (continued)

°C . This amount of temperature increase is similar to that shown in the cross sections at 60 and 72 h (see Figs. 4.11a,b).

Based on the above analysis, we conclude that the formation of the warm core in the idealized case is mainly due to subsidence warming within the eye-like structure. Although the heating rate is not very large, its persistency leads to accumulated heating effect in the core area. This warming mechanism may also have occurred in the RDS. In Fig. 3.13, adiabatic warming is depicted near the center of the system over a small area. Since the budget analysis performed in the RDS is based on instantaneous data instead of a time average, such weak signal was too weak to be detected. In addition, the strong effect of horizontal advection may further mask the signal. In the present idealized simulation, this mechanism could be clearly revealed because the MCV environment is devoid of the complexity of the large-scale flow which was present in the RDS.

Recent observational studies (Simpson et al 1997; Harr, 1996) reveal that the eye-like structures may exist during the genesis stage of some, if not all, tropical cyclones. Several theories have been put forth to explain the cause of the descending flow in the eye region. Shapiro and Willoughby (1982) proposed a conceptual model, referred to as the conventional model (Willoughby, 1998), in which the descending flow in the eye is a kind of compensational subsidence associated with vigorous convection in the eyewall. The air would detrain from the eyewall near the tropopause, sinks in the eye and is entrained into the eyewall at the bottom. The idea of subsidence directly caused by the eyewall convection was questioned by Emanuel

(1997). He used a balance model to demonstrate that the convectively induced subsidence cannot by itself raise the vertically averaged temperature in the eye to values greater than those inside the eyewall. He proposed that the heating in the eyewall would cause a collapse toward a thermal and momentum discontinuity at the eye boundary. Such a collapse may start the process of radial turbulent diffusion of momentum, which induces mechanically rather than thermally a secondary circulation to form a warm core. Willoughby (1998) argued that such collapse may be prevented by mixing. Meanwhile, he modified the conceptual model (Shapiro and Willougby, 1982), based on analysis of observational soundings taken in the center of some hurricanes, and suggested that the air of the descending flow above the inversion in the eye was present since the eye first formed. He showed that the time required to accomplish such a cycle is comparable to the life time of a hurricane. As the eye contracts, the slow descent in the eye, with a magnitude of a few centimeters per second, represents the response to the net mass loss caused by the moist downward cascade inside the eye and the convective updrafts in the eyewall above the inversion.

Montgomery and Enagonio (1998) suggest that the warm-core formation during the genesis stage is through the process of the so-called axisymmetrization, in which the convection along the periphery of the midlevel vortex can be regarded as a small PV anomalies. The ingestion of the PV anomalies into the parent vortex may lead to the spin up of a surface cyclone. Through axisymmetrization, the mean subsiding flow forms as a result of eddy-momentum fluxes.

Most recently, Zhang et al. (1999) examined the relative importance of buoyancy and dynamically induced vertical pressure gradients by inverting the balance equation using numerical simulation data associated with Hurricane Andrew (1992). They found that the net buoyancy effect is similar in magnitude but opposite in sign to the dynamically-induced pressure gradient force (PGF). Of importance is that the dynamically-induced PGF points downward in the eye to account for the maintenance of the general descent. But it points upward in the outer half portion of the eyewall to facilitate the lifting of high-θe air in the lower troposphere. Furthermore, this dynamic force is dominated by the radial shear of the tangential winds.

In our case, the small but persistent descent indicates features similar to those depicted in Zhang et al. (1999). However, the 25-km resolution used in our simulation cannot be expected to reveal much fine structure within the eye, such as the separation of the dry descent from the moist downward motion adjacent to the eye. To obtain more insight into the dynamic and thermodynamic properties of the eye, high-resolution simulations (e.g. Liu et al. 1997) would have to be performed in future studies of tropical cyclogenesis.

4.4. Summary

Using idealized initial conditions, a 72 h simulation of tropical cyclogenesis has been carried out. The construction of the initial conditions is based on a RDS, but is much general by removing the baroclinic system like a front. In such an environment,

the simulation of the transformation from a midlatitude mesovortex into a tropical storm is more relevant to the tropics, where the large-scale flow is near barotropic. The simulation reproduces very well the life cycle of a mesovortex which eventually leads to the formation of a tropical storm. Specifically, the generation of the midlevel mesovortex, the dissipation of the vortex, the initiation of the oceanic storm in the confluent zone created by the interaction between the circulation of the MCV and the southerly flow of the subtropical high, and the amplification of the vortex into a tropical storm are all simulated.

However, the idealized simulation does produce some features that were not present in the RDS. By decomposing the vertical relative vorticity associated with the oceanic storm into curvature vorticity and shear vorticity, our analysis shows that the amplification of the low-level vortex after 36 h is mainly contributed by the increase of curvature vorticity. The role of shear vorticity is reflected in the northeast portion of the intensifying vortex at a later stage. This picture is different from that presented in the RDS, in which the shear vorticity, associated with a north-south oriented convective band, increases first and is advected into the center by a wrap-around flow to be converted into curvature vorticity. The reason for the difference may be due to the influence of the northerly prefrontal flow on the evolution of the north-south convective band in the RDS, a situation which is absent in the idealized simulation.

The eye-like structure is successfully simulated during the period of rapid deepening of a tropical storm. The vertical profile of vertical velocity at the center of the surface low reveals that the descending motion is slow but persistent. The time

averaged θ budget calculated over the eye-like area at 800 hPa shows that the formation of the warm core is caused by the descending motion. This mechanism may not have been fully revealed in the RDS due to the presence of strong horizontal advection associated with the wrapped around flow.

Chapter 5

The impact of model physics on the idealized simulation: sensitivity studies

5.1 Introduction

In the preceding chapter, we presented a 72 h idealized simulation of the transformation of an MCV into a tropical storm. Such a transformation results from a series of dynamical and physical processes, such as persistent convection, air-sea interaction and radiation. Numerous studies have shown that the generation of a tropical storm is closely linked to multi-episodes of organized convection (Gray, 1998; Harr et al, 1996; Simpson et al, 1998). Moreover, Gray (1998) suggests that subsidence induced by radiative cooling may provide forcing to trigger new convection. The theoretical study of Emanuel (1986) proposes that the heat and moisture fluxes, supplied by the warm sea surface, are responsible for eliminating the cold pool associated with the midlevel MCV. In our model, these processes are represented by the planetary boundary layer (PBL) parameterization, the radiation package, the cumulus parameterization scheme (CPS) and the explicit moisture scheme. Among them, CPS may be considered as one of the most important components in mesoscale modeling, because the successful simulation of the different types of mesoscale convective systems (MCSs) may hinge upon closure assumptions and physical processes included in the parameterization. Certain changes in the CPS

may have significant impact on the structure and evolution of the simulated MCSs (e.g., Rosenthal, 1979; Baik, 1991).

In this chapter, we present the results of a number of sensitivity experiments. First, the impact of a different CPS on the structure and evolution of the MCV leading to the formation of a tropical storm will be examined. Instead of the Kain-Fritsch (hereafter, KF-CPS) scheme in the control simulation, the Betts-Miller (hereafter, BM-CPS) scheme will be tested. Our analysis will focus on a comparison of the vertical structure of the vortex, the time evolution of convection and the processes responsible for the formation of the warm core in the two schemes. Second, we will examine the effect of varying the heat and moisture fluxes, supplied by the warm ocean, on the persistent convection during the rapid deepening of a tropical storm. Third, the effect of varying the long-wave radiation on the control run will be investigated.

5.2 The BM-CPS simulation

The BM-CPS was originally designed for improving the simulation of precipitation over the tropics in large-scale models. Its success in large-scale models has led to its implementation in mesoscale models. For example, the modified version of BM-CPS has been incorporated into the NCEP Eta model (Black, 1994; Janjic, 1994 and Kain, 1999). Unlike large-scale models, the issue of convective parameterization in mesoscale models is complicated, because both the convective and stratiform components of precipitation and their interaction must be accounted

for. Therefore, it is necessary to assess the impact of BM-CPS on the structure and evolution of the simulated MCSs.

The basic idea behind the BM-CPS is that the local thermodynamic structures are constrained by cumulus convective activity to adjust towards an observed quasi-equilibrium state or the so-called reference state. The reference temperature profile is based on the moist adiabat for a conditionally unstable lower troposphere. It closely parallels a moist virtual adiabat below the freezing level. The reference moisture profile is computed from the temperature profile by specifying the saturation pressure deficit (SPD), defined as the difference between the pressure at the originating level of an air parcel and its saturation point (Betts, 1982). SPD is specified at cloud base, freezing level and cloud top and a linear interpolation is used to obtain its values at other levels. These reference profiles are constrained to satisfy the conservation of total enthalpy. Then, the convective precipitation rate (P_c) is calculated. If P_c is found to be negative, convection will not be 'triggered', which means that the tendency of temperature and moisture changes due to convection would be set to zero in the column. The time scale of adjustment depends on the model grid resolution. In the present study, it is set to one hour.

The absence of moist downdrafts is a weakness in the original BM-CPS. Moist downdrafts can significantly alter the thermodynamic structure near the surface over convective areas. Numerical simulations showed that moist downdrafts produce important low-level perturbations, such as mesohighs, mesotroughs and outflow boundaries (Zhang and Fritsch, 1988; Zhang et al. 1989). Observational studies have

also shown that moist downdrafts play an important role in the subcloud layer (Betts and Miller, 1993). To alleviate the shortcoming in the original version of the BM-CPS, Betts and Miller (1993) introduced a downdraft mass flux to account for low-level cooling and drying. They simply defined reference profiles for an unsaturated downdraft (T, Q_v). The profiles are given by the temperature and the water vapor content of an air parcel starting at a level near 850 hPa and descending under the constraint of constant θe and subsaturation. A separate adjustment time scale, related to the divergence of the downdraft mass flux, is also introduced. This time scale is determined by coupling the evaporation in the downdraft to the precipitation rate. Finally, the energy correction term is modified in accordance with the two adjustment time scales. In the present study, we adopted the implementation of downdrafts by Nagarajan (1999, personal communication).

Similar to the BM-CPS, the basic idea of the KF-CPS is also to nudge the atmosphere toward a convectively neutral state within a time scale of an hour (Kain, 1999). However, the way to reach the convective neutral state is different in the two schemes. In contrast to the empirically determined reference profiles of temperature and moisture in the BM-CPS, the KF-CPS applies a simple mass flux updraft and downdraft plume model to compute the adjusted temperature and moisture profiles. Such mass flux approach extracts moisture from a shallow layer near the cloud base to satisfy the closure assumption (i.e., the removal of available buoyant energy in the updraft layers). Therefore, it may not be sensitive to the presence of a deep layer of moisture (Kain, 1999). In addition, the mechanism of triggering convection in the KF-

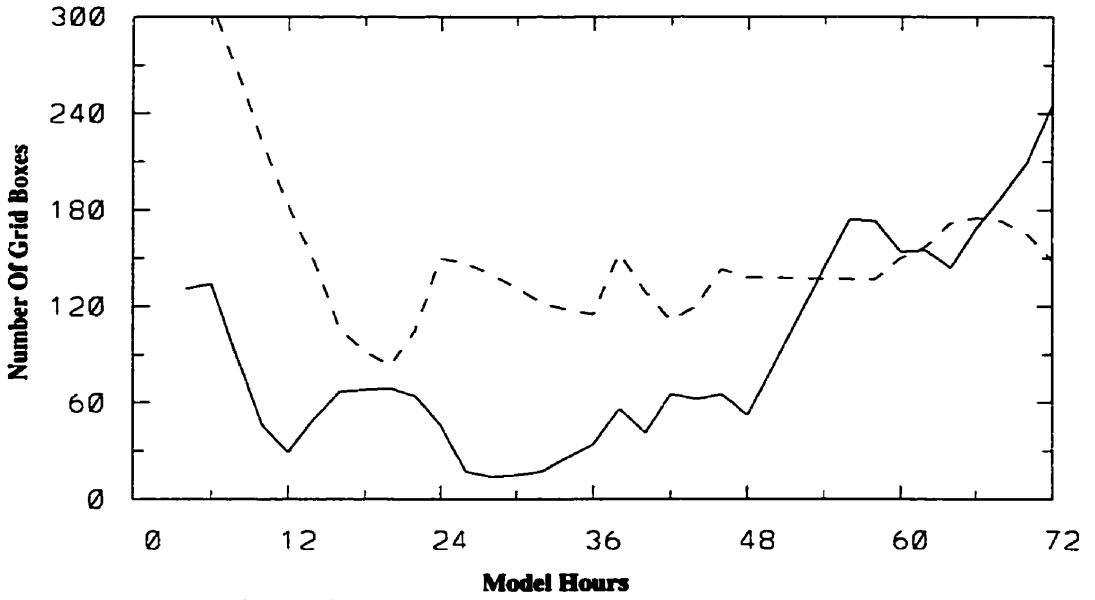

Fig. 5.1 The time evolution of area (number of grid boxes) occupied by convection for the KF-CPS run (solid line) and the BM-CPS run (dashed line).

CPS is based on CAPE and dynamic forcing (i.e., the intensity of upward motion), whereas in the BM-CPS, it is determined only by the thermodynamic structure of a deep layer. Because of the different approaches in reaching the 'reference state' in the two schemes, differences in the structures of precipitation and the subsequent evolution of MCSs may be expected. In the following sections, we will examine these aspects in a 72 h sensitivity simulation using the BM-CPS. The initial conditions, boundary conditions and the model configuration remain the same as the control run.

5.2.1 The time evolution of convective activity

Figure 5.1 compares the time evolution of deep convection between the control and the BM-CPS runs. During the first 24 hours, the areal coverage by deep convection in the BM-CPS run almost doubles that in the control run, indicating stronger convective activity. It should be recalled that the sounding over the center of the convective area at initial time, depicted in Fig. 4.2c, indicates a deep layer of conditional instability with ample moisture supply. As compared to the KF-CPS in the control run, the response of BM-CPS to such a moist sounding is especially large. The strong convective outbreak in the BM-CPS removes the moisture rapidly in a vertical column, rendering it more difficult for grid scale saturation to be reached. As a result, no grid-scale precipitation appears in the BM-CPS run during the first 24 h. In comparison, half of the total rainfall in the control run during the same period arises from grid-scale precipitation. Since the heating profile by grid-scale condensation and evaporation processes differs from that by convection, the vertical

structure of the simulated system may vary between the BM-CPS and the control runs, as will be shown below.

After 24 h, the areal coverage of convection in the BM-CPS experiment appears to reach a steady state. The hourly model output shows that deep convection is confined to the center of the surface pressure system during the remaining 48 hours. Alternating inactive (24 -36 h) and active convective (36 - 72 h) phases seen in the control run were absent (see Chapter 4). Observational study (Zehr, 1992) indicates that before a surface system spins up to become a tropical depression, it usually undergoes multiple convective phases. The failure by the BM-CPS to simulate these phases implies that the simulated deepening process by the BM-CPS is less realistic than that obtained by the KF-CPS.

5.2.2 The evolution of sea-level pressure (SLP)

The simulated sea-level pressure at 24 and 72 h is shown in Figs. 5.2 a-b. At 24 h, the surface low is already strong enough to exhibit a closed isobar, in contrast to a shallow trough in the control run. Organized convection accompanied the surface low, in contrast to isolated and scattered convection in the control run. These results clearly indicate that the BM-CPS does not simulate properly the dissipation of the MCS after it moves offshore. At 72 h, a well-developed surface low occurs (Fig. 5.2b). The intensity of the low is nearly the same as that in the control run, but with a different distribution of convection. In the control case, a spiral band with a northeast-southwest oriented tail lies ahead of the center of the low (Fig. 4.3d). Here, the convective area covers most of the low although its orientation indicates some degree

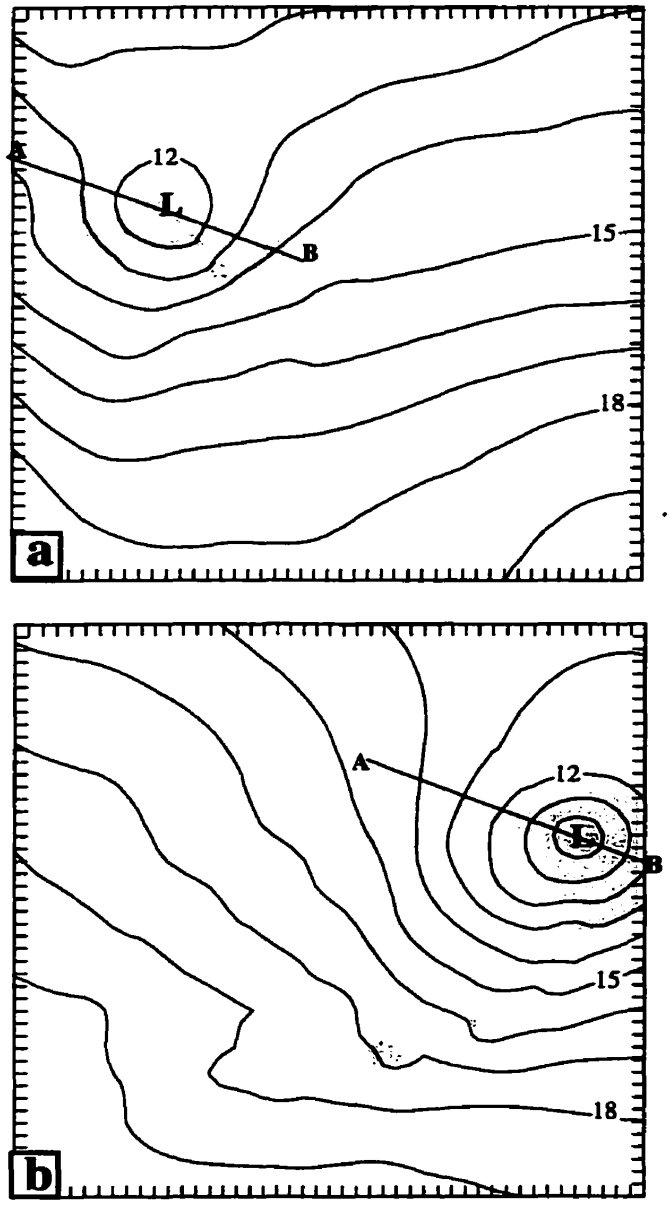

Fig. 5.2 Distribution of sea-level pressure (solid, every 1 hPa), and convective areas (shaded) from (a) 24 h; and (b) 72 h integration in the BM-CPS run. Line AB denotes the location of cross section used in Fig. 5.4.

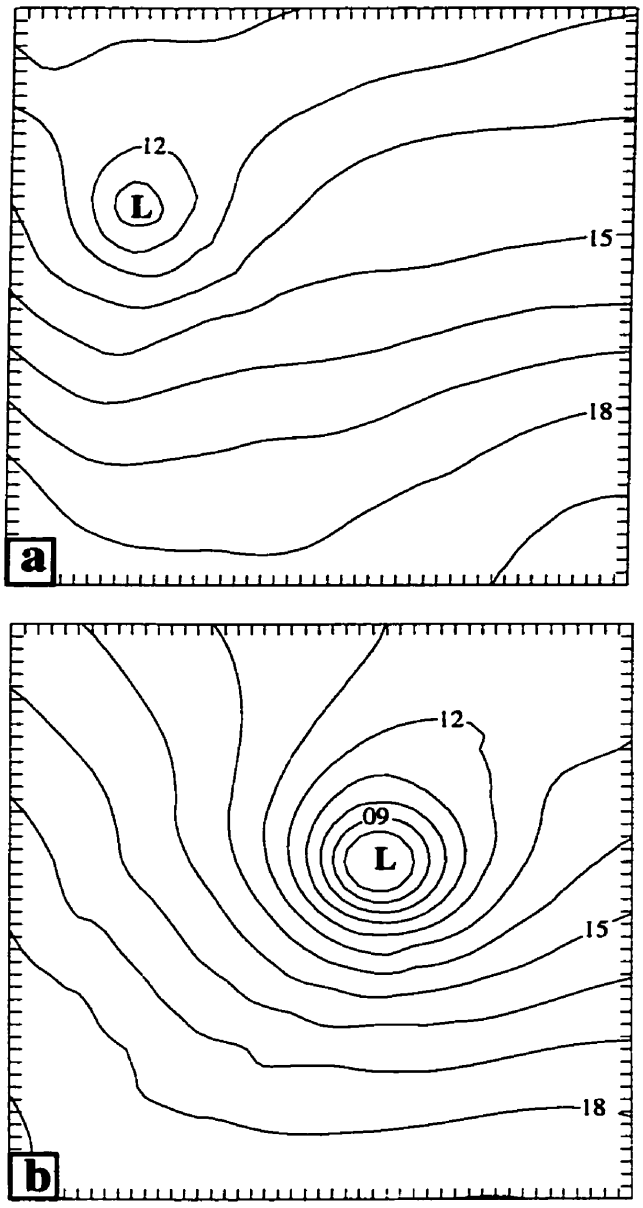

Fig. 5.3 The simulated SLP of the BM-CPS run (without downdrafts) (a) at 24 h and (b) at 60 h.

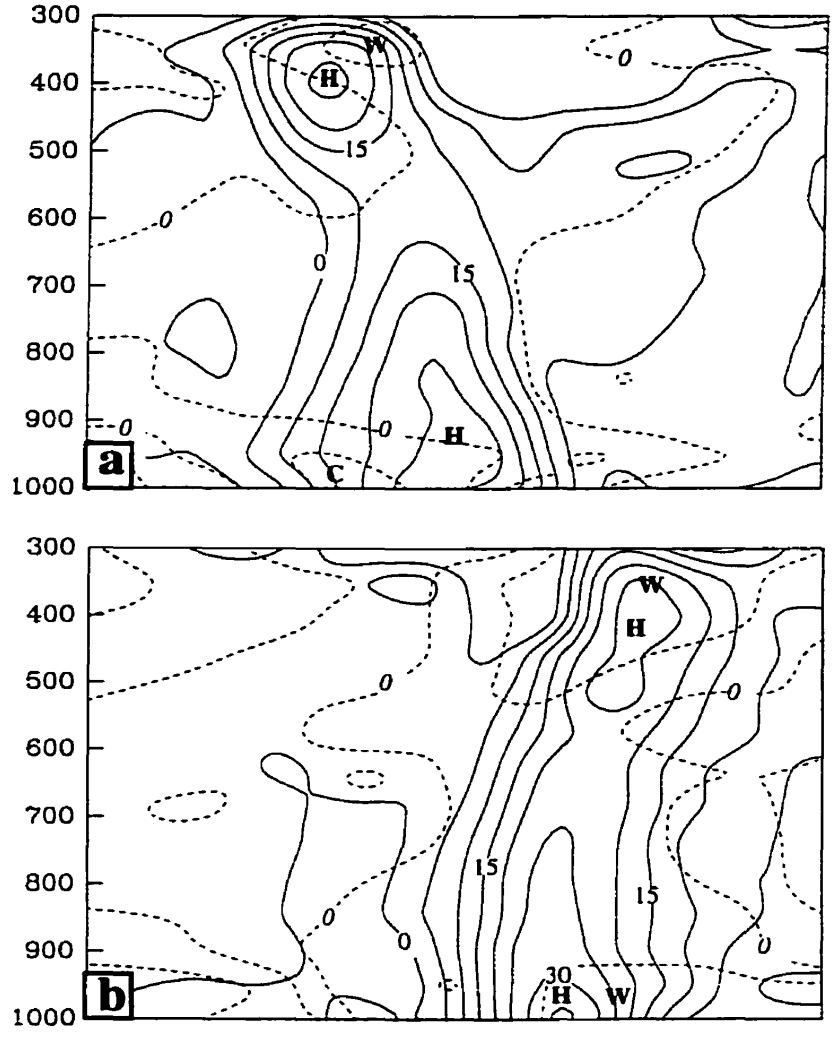

Fig. 5.4 Vertical cross section of vertical relative vorticity (solid) at interval of 5×10^{-5} s^{-1} superposed with deviation temperature (dashed) at intervals of 1°C from (a) 24 h; and (b) 72 h in the BM-CPS simulation.

of rotation. The tail is not well organized and breaks into pieces. The simulation also fails to generate an eye-like structure. Since the triggering of convection in the BM-CPS is not directly related to the dynamics field, convection may be initiated even in a weakly descending flow as long as the thermodynamic profiles favor the generation of precipitation. To simulate properly an eye-like structure, an additional constraint in the triggering function of the BM-CPS may be needed (Yubao Liu, personal communication, 1999).

Although at 24 h, the sea-level pressure in the BM-CPS run already exhibits a closed isobar, the intensity of the system at 72 h is similar to the control case. The reason may lie in the inclusion of downdrafts in the BM-CPS. To substantiate this point, we perform another sensitivity experiment in which the downdrafts are turned off. The simulated SLPs, given in Figs. 5.3 a-b, indicate that at 24 h, the surface low is deeper and it undergoes rapid deepening during the next 36 hours. Its intensity is much stronger at 60 h than the control case at 72 h. Obviously, such rapid development is not realistic at least for the case of the transformation of a midlevel MCV into a tropical storm, because it usually takes much longer to complete such a transformation in nature. Our experiment confirms the findings of previous studies that the proper representation of downdrafts in CPS may be critical in the simulation of some meso-β scale surface pressure systems.

5.2.3 The vertical structure

The impact of the BM-CPS on the structure of the vortex can be examined from the vertical cross sections over the center of the surface low. Fig. 5.4a shows

that the vertical structure of relative vorticity and temperature deviation are different from the control case. Instead of a maximum intensity at the midlevel, the strongest vorticity is located at the upper (400 hPa) and the lower (900 hPa) levels. Consistent with a deep convection heating profile in the vertical, the warm core is located as high as 350 hPa and the cold pool is confined only to the boundary layer.

The failure of the BM-CPS to simulate properly the warm core/cold pool couplet is attributable to the lack of latent heat release by grid-scale condensation processes at the midlevel and the accompanying evaporative cooling below. The BM-CPS was designed to prevent saturation at conditionally unstable grid points, it is therefore rare that even if it is combined with an explicit moisture scheme, would generate stratiform rainfall within a time scale of less than two days (Baik, 1991; Kain et al, 1997). However, observational studies (Bartels and Maddox, 1991; Gamache and Houze 1985) do suggest that MCVs may result from vertical heating gradients in the stratiform precipitation region. Numerical simulations (Zhang and Fritsch, 1987; Zhang et al, 1988; Chen, 1990; Rogers, 1999) also demonstrated that the KF-CPS or the Frank-Cohen-CPS can, in combination with an explicit moisture scheme, develop grid-scale heating which contributes to the generation of MCVs. Similarly, Bister and Emanuel (1997) generated stratiform precipitation in an artificial rain shaft and produced an MCV.

Nevertheless, the structure of relative vorticity, depicted in Fig. 5.4a, indicates some features of a tropical system with a maximum in vorticity located within the boundary layer. Because the cold pool is shallow, it is easily destroyed by

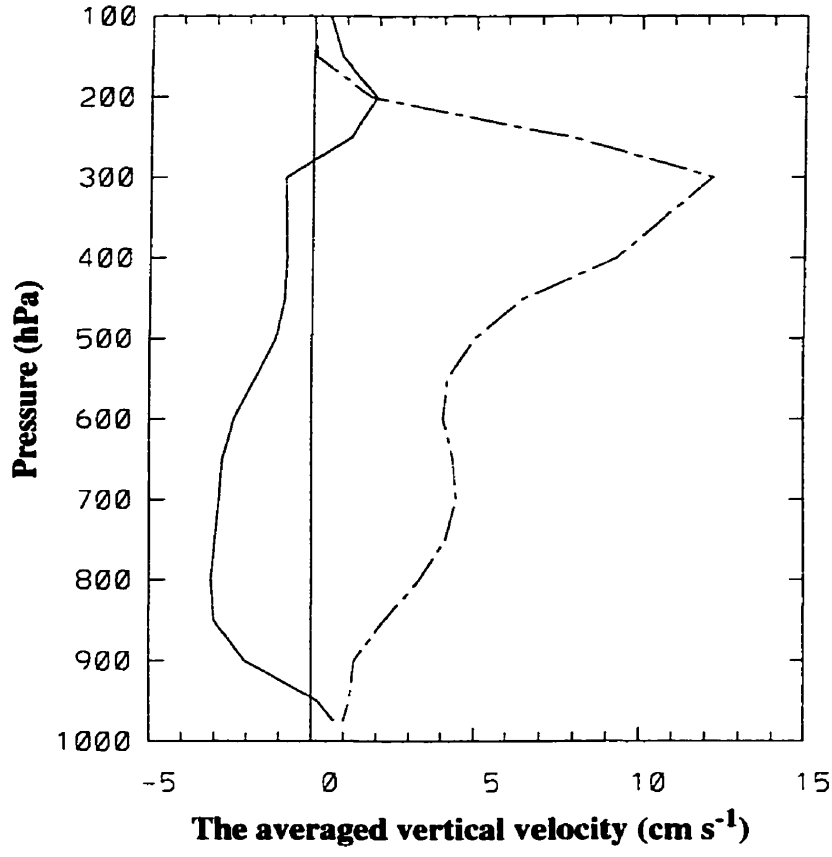

Fig. 5.5 Vertical velocity at the center of the surface low that is averaged between the 60 h to 70 h in the KF-CPS (solid) and the BM-CPS (dashed) simulations.

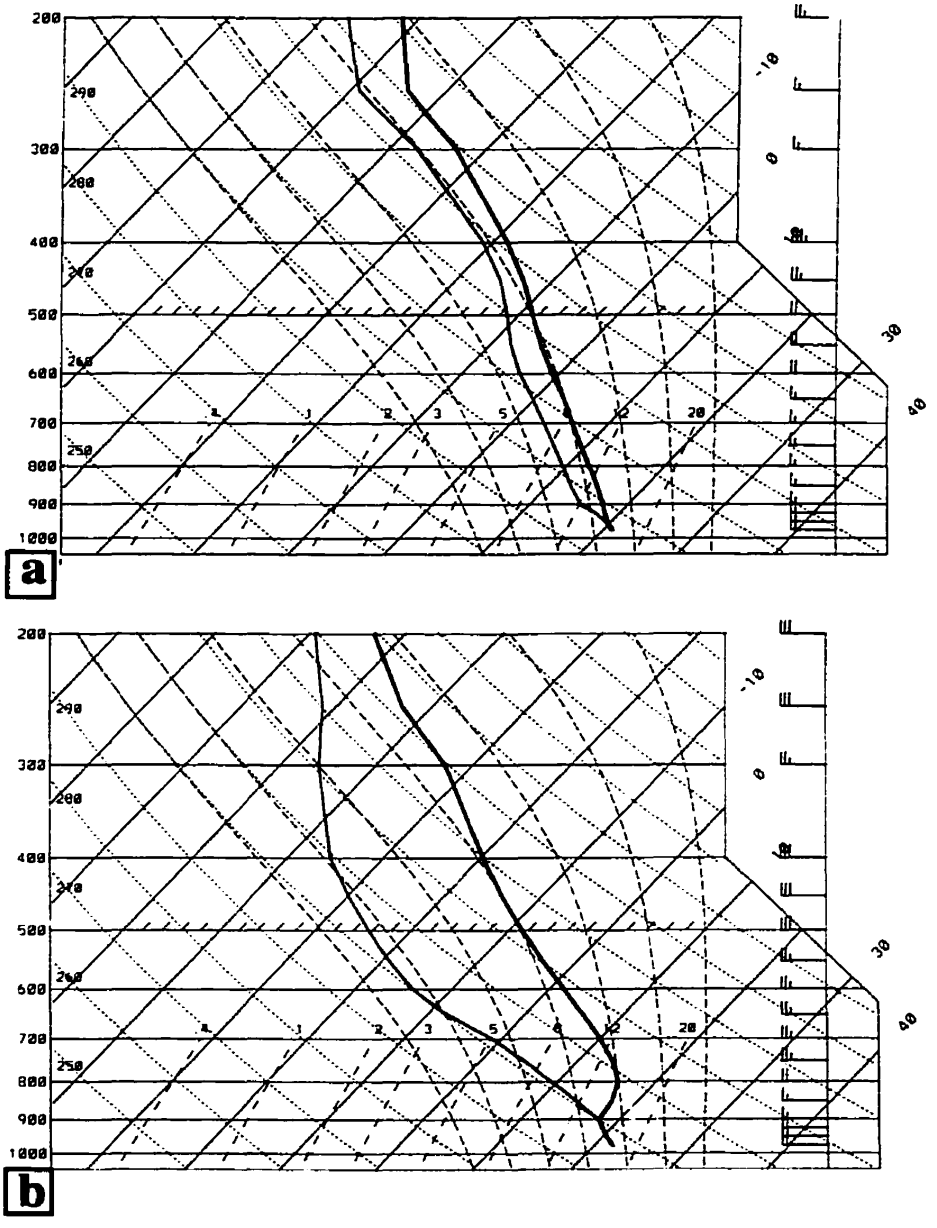

Fig. 5.6 A skew T-Log P sounding taken at the center of the surface cyclone from the 72 h simulation with (a) the BM-CPS; and (b) the KF-CPS. A full barb is 5 m s^{-1}.

sensible heat fluxes when the system moves over warm water after 60 h. Indeed, Fig. 5.4b shows that the cold pool is eliminated at 72 h and warm air occupies the whole column associated with the vortex. There are two centers of warm air: one above 400 hPa arising in response to the convective heating, and the other is confined within the boundary layer. Note that there is no warm center near 800 hPa.

Fig. 5.5 depicts the averaged vertical velocity at the center of surface low over the last 12 hours (i.e., 60 - 72 h). In contrast to the descending motion in the control case, ascending motion is present at all levels in the BM-CPS run. This result is consistent with the fact that the central area of the surface low is covered by active convection. Fig. 5.6 compares the soundings taken at the center of the surface low from the two experiments. The BM-CPS run produces a moist sounding with near-moist adiabatic lapse rate at the cyclone center (Fig. 5.6a), whereas the control sounding exhibits a dry atmosphere above the boundary layer with an inversion in the 900-800 hPa layer (Fig. 5.6b). In summary, the process of descent-induced warming is not present in the BM-CPS run. Instead, deep convection and latent heating, leading to ascending motion, occupy the air column over the surface low. Consequently, the simulation did not generate the typical eye-like structure.

5.3 Sensitivity to surface fluxes

Since all tropical cyclones are initiated over warm water, the characteristics of the marine environment may have a strong influence on the formation of tropical cyclones. Therefore, it is of interest to examine the impact of surface sensible heat and moisture fluxes.

Three experiments were conducted: NOHFX, NOQFX and NOFLX denote no sensible heat flux, no latent heat flux and no sensible + latent heat fluxes, respectively. Because in the control run, the MCV moves offshore after 24 h and initiates a tropical storm at 36 h, we begin sensitivity experiments with the initial state of the control run at 24 h and then integrate for a duration of 48 h.

The simulated SLPs at 72 h (after 48 h) for these experiments are shown in Fig. 5.7. The effect of neglecting surface heating (NOHFX) turns out to be quite small. The SLP differs by 1 hPa and the pattern of convection is similar whether surface sensible heat fluxes are included or excluded. The largest difference relative to the control run arises when moisture fluxes are turned off. The storm did not develop in both the NOFLX and the NOQFX runs (Figs. 5.7a-b). The pattern of convection near the surface trough indicates no organization.

The surface sensible and latent heat fluxes at the incipient stage of the storm (60 h) for the control case (CTL) are given in Fig. 5.8. The magnitudes of both fluxes are similar to those found in the RDS. When compared to the analysis by Black and Holland (1995) for tropical cyclone Kerry (1979), the latent heat fluxes presented here and in the RDS are small due to the different surface wind speeds. In particular, the analysis by Black and Holland was for an intensifying tropical cyclone, with maximum surface wind speeds around 40 m s^{-1}. The latent heat fluxes presented in Fig. 5.8 are associated with an incipient tropical storm, with a simulated surface wind speed of less than 17 m s^{-1}. The distribution of deep convection almost coincides with the area having strong sensible heat fluxes. The presence of cold downdrafts

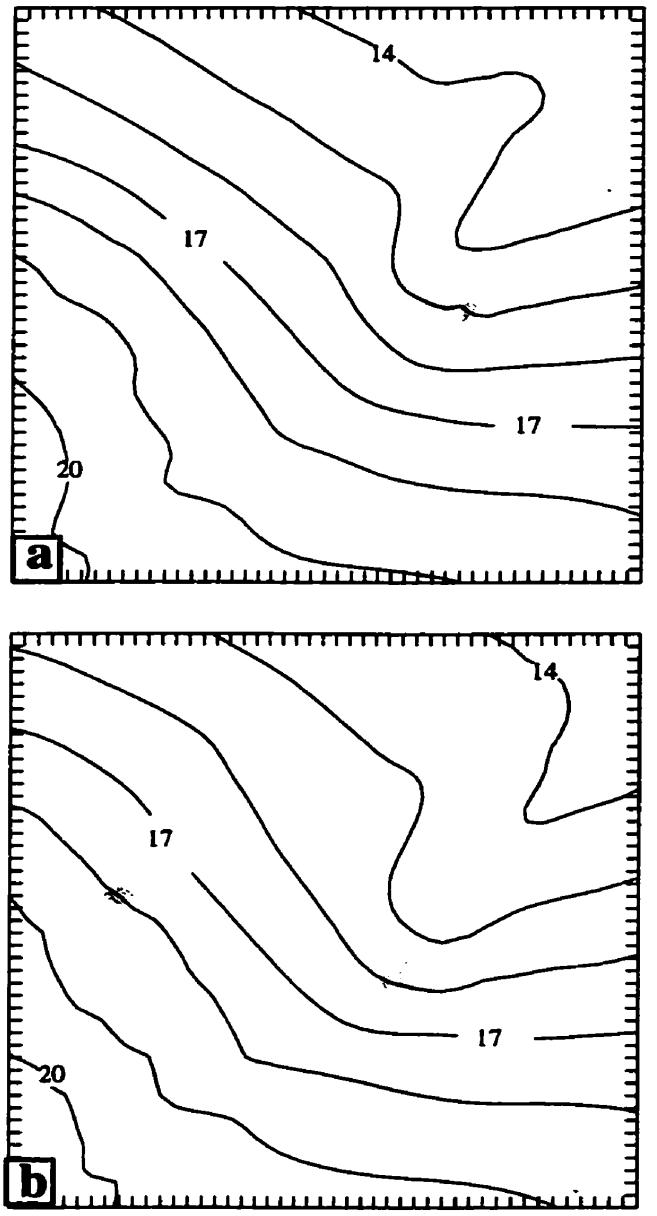

Fig. 5.7 As in Fig. 5.2b but for experiment (a) NOFLX; (b) NOQFX; and (c) NOHFX.

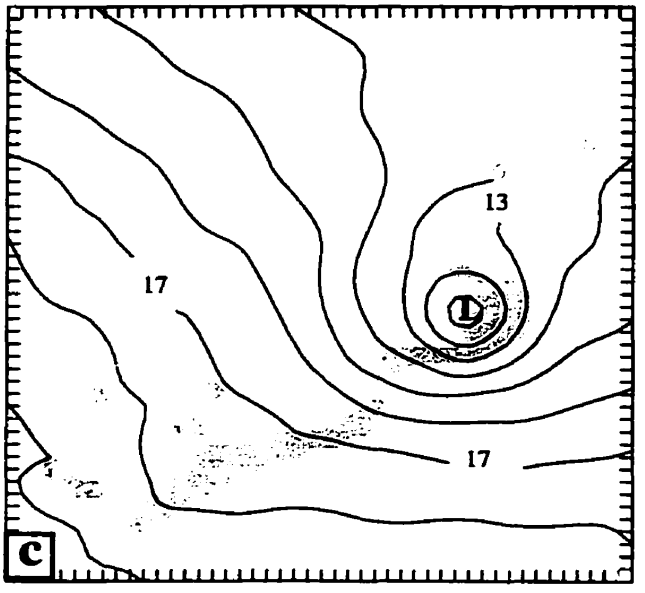

Fig. 5.7 (continued)

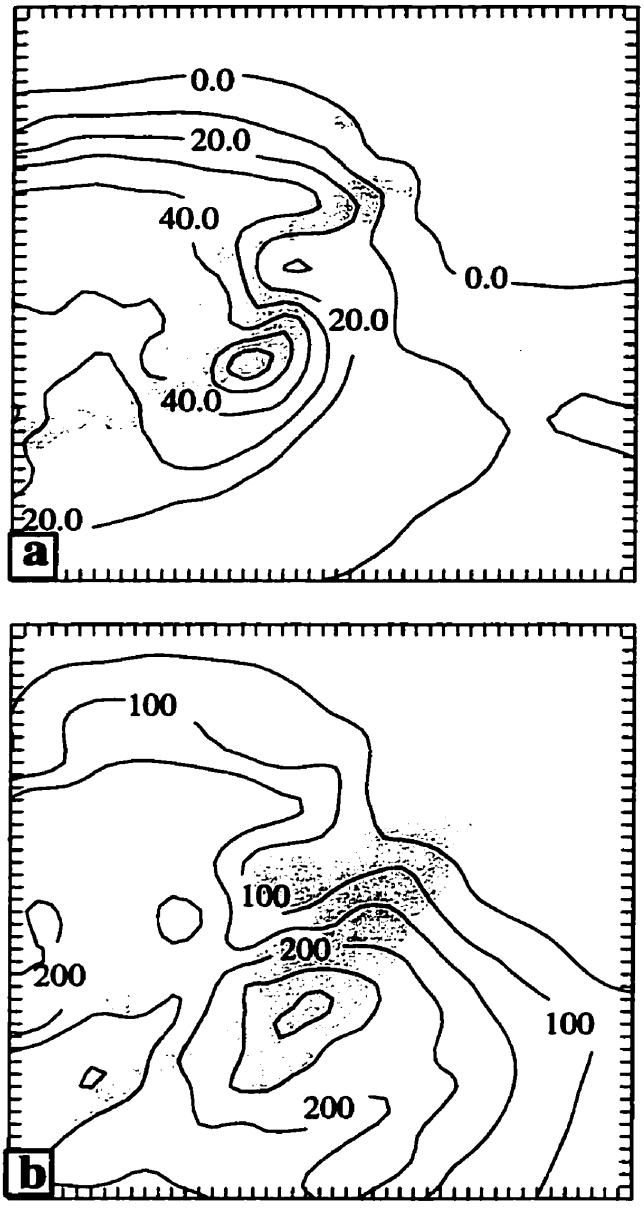

Fig. 5.8 Surface sensible heat flux (solid) at intervals of 10 W m^{-2} and active convection (shaded); and (b) latent heat flux at intervals of 50 W m^{-2} with CAPE larger than 1000 J Kg^{-1} (two hours later) (shaded). Both are taken from the 60 h control simulation.

over the convective area contributes to the sharp air-sea temperature difference. The result suggests that the enhanced sensible heat fluxes may be the outcome of deep convection rather than its cause. In contrast, larger latent heat fluxes are located ahead of the convection band. Over that area, there is relative dry descending flow and strong surface winds. Both can act to increase the positive moisture fluxes. It is interesting to note that the area with the largest latent heat fluxes closely match the distribution of the larger CAPE two hours later (Fig. 5.8b). It appears that the latent heat fluxes play a leading role to moisten and destabilize the PBL and render the environment conducive to the generation of new convection. On the other hand, the convective activity helps to enhance moisture fluxes ahead of the convective band. Therefore, a positive feedback mechanism is in operation to maintain the persistent convection with the moisture fluxes ahead of the convective band helping in the production of CAPE. More support for this positive feedback can be found in the time evolution of the area covered by positive CAPE in the three experiments (Fig. 5.9). The area with positive CAPE in the NOQFX run is about 30 % of the control case before 48 h. The percentage decreases after 54 h to attain a value of only 10 % at the end of the integration. Recall that during the last 18 h (54 -72 h) in the control run, deep convection develops dramatically. The stronger convective activity generates larger surface moisture fluxes, which in turn produces more CAPE in the control (CTL). Thus, the surface moisture fluxes represent the most important source of the production of CAPE, to maintain persistent deep convection. The time variation of the area of CAPE in NOHFX is similar to the control. The smaller magnitude in the

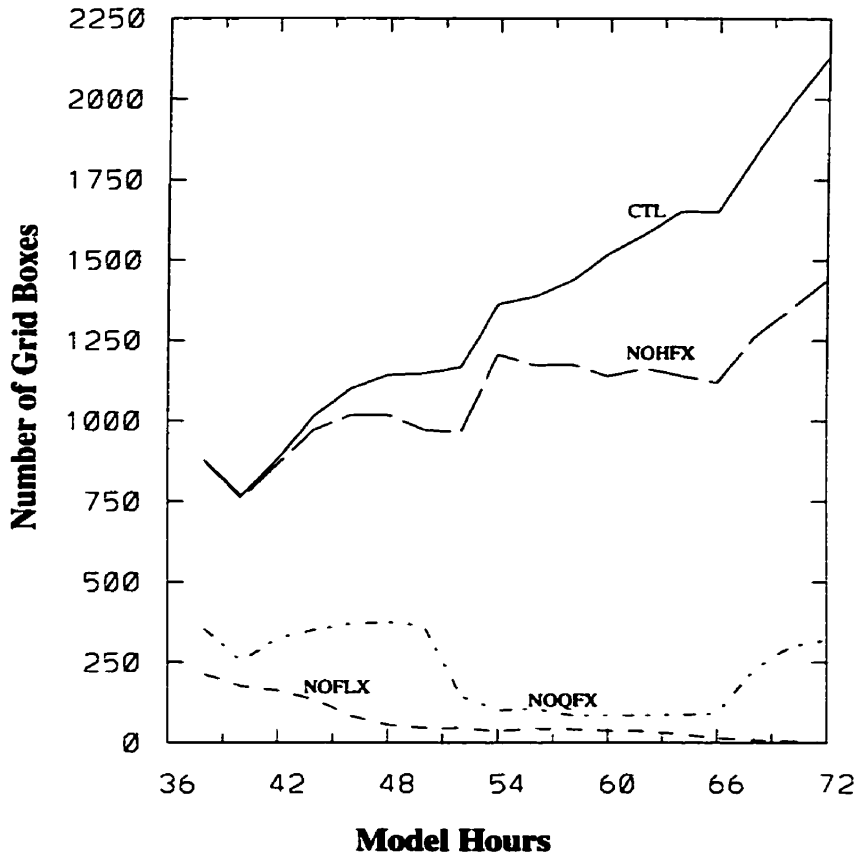

Fig. 5.9 The time evolution of the area occupied by positive CAPE from the CTL, NOFLX, NOQFX and NOHFX simulations.

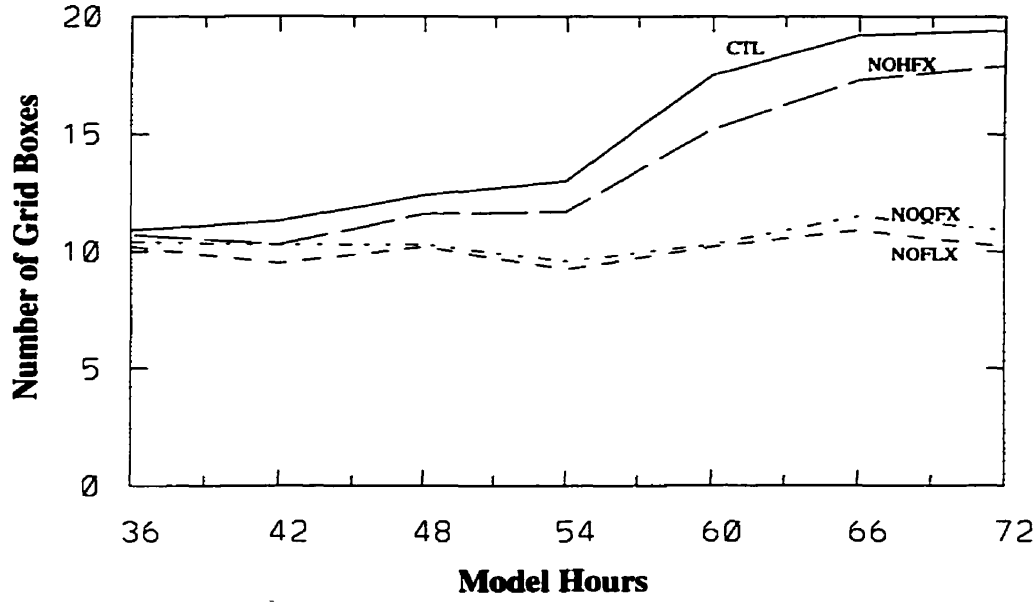

Fig. 5.10 As in Fig. 5.9 but for the maximum surface wind associated with the cyclone.

former case indicates that the sensible heat fluxes can still make a small contribution to the production of CAPE.

The maximum surface wind associated with the storm is an important link in the processes of air-sea interaction and impacts strongly on the transfer of surface fluxes (Emanuel, 1986; Fritsch et al., 1994). Its magnitude is highly dependent on the convective activity. The curves in Fig. 5.10 indicate that an increase in the surface wind in runs CTL and NOHFX at 54 h. This timing is consistent with the beginning phase of active convection. At this time, the amplitude of the surface wind in the two experiments is about 12 m s^{-1}, similar to the strength of the start-up vortex used in the study of Rotunno and Emanuel (1987). Note that in the NOQFX and NOFLX runs, the surface wind fluctuates with time, but never exceeds 12 m s^{-1}. The weaker surface wind speed is a result of the smaller surface latent-heat fluxes, which reduce the generation of CAPE and render the environment unfavorable to the maintenance of persistent convection. Consequently, the positive feedback mechanism for air-sea interaction cannot be effective.

5.4 Sensitivity to long-wave radiation

To study the impact of long-wave radiation on the cyclone development, a sensitivity experiment is conducted in which everything is identical to the control experiment except that long-wave radiative flux divergence is set to zero after 24 h (NOIR). As compared to the control run, the intensity of the simulated surface low is about halved at 72 h (Fig. 5.11). This is due to the significantly weaker convective activity during the later stages. Fig. 5.12b displays the accumulated convective

precipitation (ACP) over the final 18 h. The areal coverage and orientation of the convection are quite different from the control run, and the differences grow significantly with time (cf. Figs. 5.12a vs. 4.4e; Figs. 5.12b vs. 4.4g).

The destabilization of the storm environment by long-wave radiation is assessed, following the approach by Krishnamurti et al. (1991). The effect of radiative destabilization can be expressed simply as:

$$\frac{\partial \overline{\Gamma_m}}{\partial t} = -\frac{\partial \overline{H_R}}{\partial p} \tag{5.1}$$

where H_R is radiative cooling and Γ_m is moist static stability. The overbars denotes a horizontal area average representative of the synoptic scale. When the cooling rate at the upper level exceeds that at a lower level, destabilization occurs because the moist static stability parameters become more negative. To evaluate the radiative cooling of the environment of the simulated storm, we first obtain the vertical profiles of the domain-averaged temperature from the CTL and the NOIR runs at 48 h and 72 h. We then subtract the vertical profiles of the NOIR run from those of the control run. The cooling by long wave radiation at 48 h is given in Fig. 5.13a, which shows that the cooling increases slightly above 800 hPa. This is indicative of the effect of radiative destabilization, particularly when considering that this vertical profile represents the cumulated cooling effect at a given time after the mass and wind adjustment. The phenomenon becomes more pronounced at 72 h (Fig. 5.13b). A comparison of Figs. 5.13a and 5.13b indicates that the net radiative cooling rate is around 1 ° C ~ 1.5 ° C per day. Although the magnitude of this cooling is not large, its cumulative effect on the atmospheric flow over three days could be substantial.

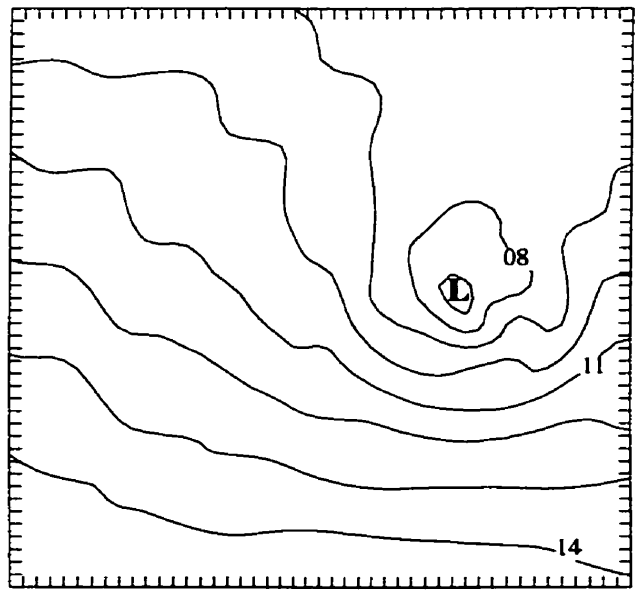

Fig. 5.11 The simulated sea level pressure at 72 h for the NOIR run.

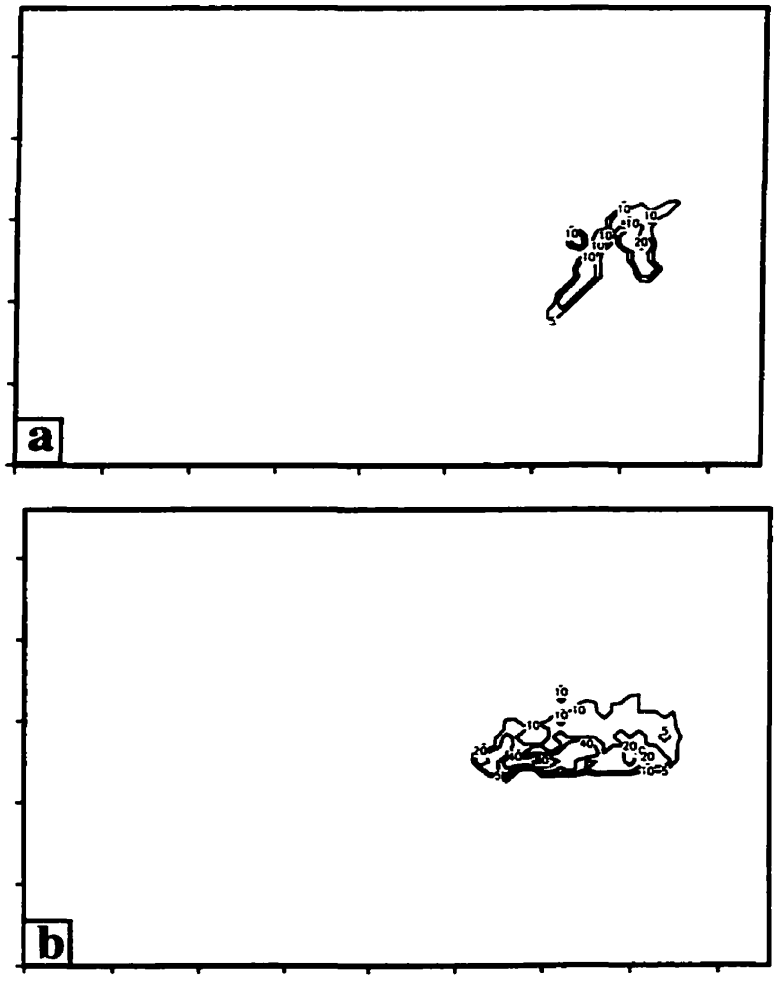

Fig. 5.12 Accumulated convective precipitation (mm) from the NOIR run between (a) 24-54 h; and (b) 54-72 h. The intervals of the contours are the same as in Fig. 4.4a.

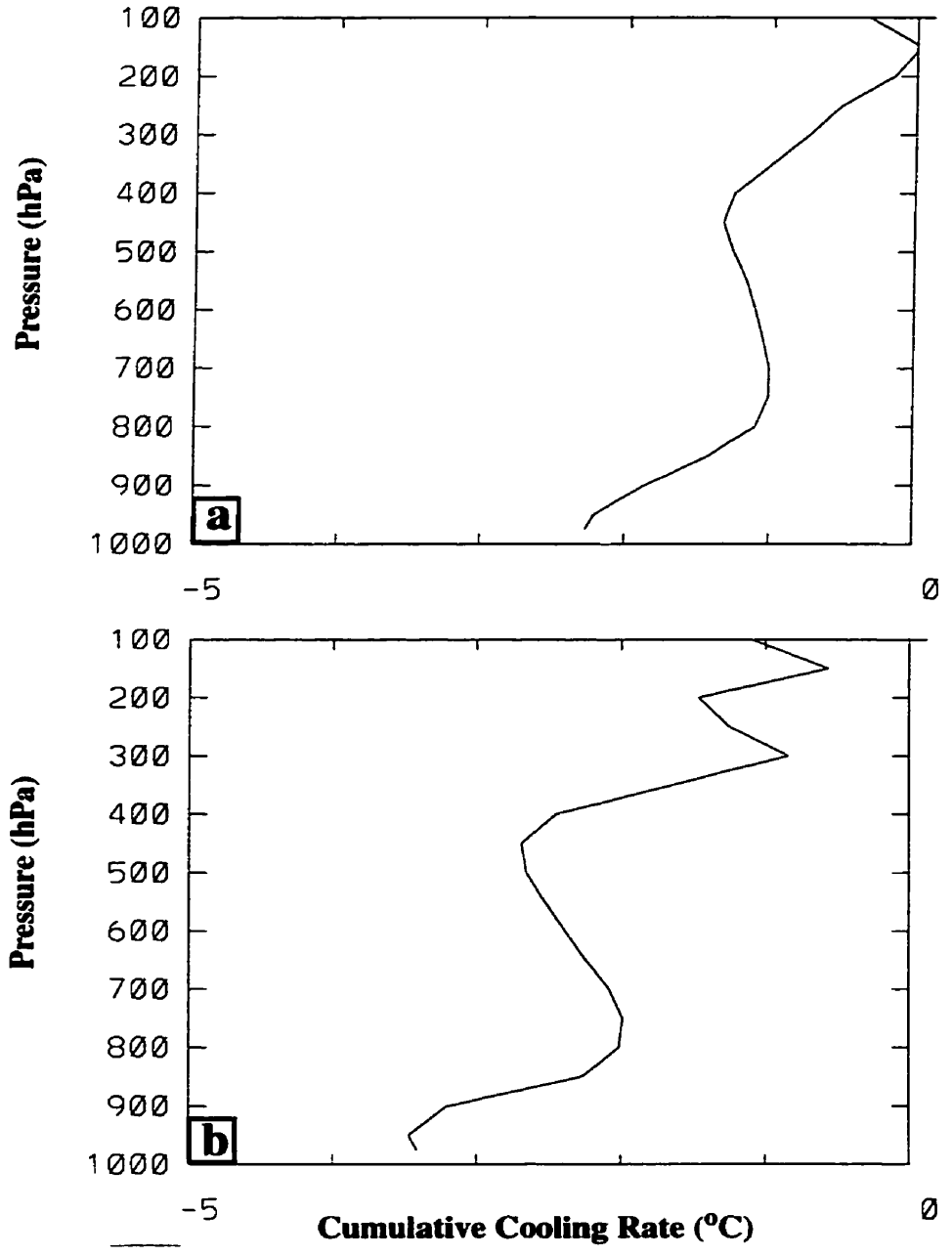

Fig. 5.13 The domain-averaged vertical profiles of cumulative cooling by long wave radiation in °C from (a) 48 h and (b) 72 h of simulation in experiment CTL. See text on how the accumulated cooling is calculated.

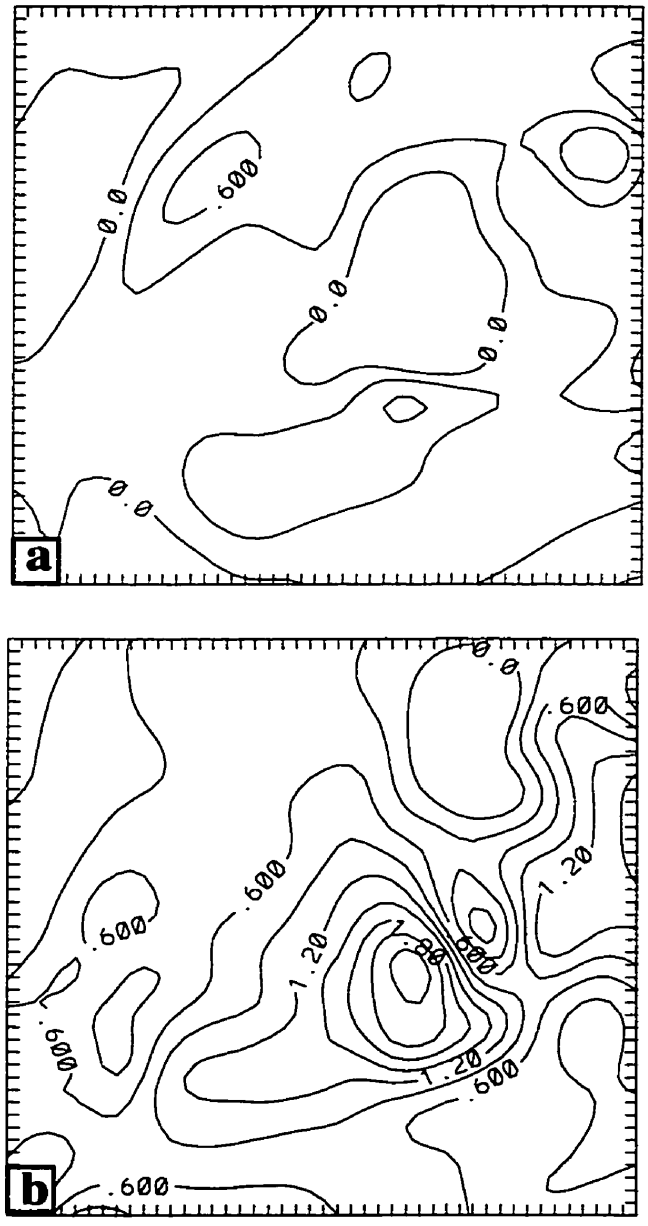

Fig. 5.14 The horizontal distribution of the destabilization by radiative forcing (every 0.3°C/300 hPa) from (a) 48 h; and (b) 72 h simulations in experiment CTL. See text for the method of calculation.

To examine the horizontal distribution of destabilization, we compute the difference in the cooling in the 800-500 hPa layer at 48 h and 72 h. A board area of small positive values is found to the northeast and southwest of the storm at 48 h (Fig. 5.14a). The area of destabilization expands at 72 h (Fig. 5.14b). It is evident that radiative destabilization over these areas contributes to the generation of the northeast-southwest oriented convective band in the control run which is totally absent in the NOIR run (cf. Figs. 5.12b and 4.4e).

5.5 Summary

In this chapter, three groups of sensitivity experiments are performed to examine the impact of CPS, surface energy fluxes and long wave radiation on the idealized simulation of tropical cyclogenesis from a midlevel mesovortex using the simulation shown in Chapter 4 as a control run.

The results show that the BM-CPS fails to simulate properly a midlevel mesovortex. When moist downdrafts are included, the BM-CPS run can produce a shallow and weak cold pool instead of a deep couplet of warm core and cold pool. As stated in the preceding chapter, the observational analysis supports the existence of such a deep thermal couplet (Bister et al, 1997). The failure to simulate such a structure in the BM-CPS run may be due to the lack of grid-scale condensation and its interaction with the CPS. On the other hand, the shallow and weak cold pool is eliminated easily by surface energy fluxes when the system moves over warm water, so that the tropical storm forms too quickly. In addition, the time evolution of convective activity simulated in the BM-CPS run does not indicate the characteristic

multiple-episodes of convection as revealed in the observational study of tropical cyclogenesis (Zehr 1992) and the numerical simulation using the KF-CPS (e.g. the control run). It appears that the simulation of midlevel mesovortex and its transformation to a tropical storm by the KF-CPS is more realistic than the BM-CPS in this case. However, we should not exclude the possibility of improving the BM-CPS run if suitable modification to the convective scheme can be made.

The sensitivity tests also show that the surface latent fluxes is a dominant factor in the production of CAPE to maintain the persistent convection, resulting in a positive feedback mechanism to spin up the storm. The cumulative cooling effect by long-wave radiation over a three-day period is significant enough to destabilize the environment of the storm, thereby enhancing convection responsible for the rapid deepening of the tropical storm during the final 18 h integration.

Chapter 6

Conclusion and summary

In this thesis, we simulated the transformation of a long-lived mid-level mesovortex into a tropical storm. Using an improved version of the PSU-NCAR mesoscale model, a 90 h real-data simulation has been carried out. The work is an extension of the 18 h simulation of the MCSs, which were responsible for the Johnstown flash flood of July 1977, by Zhang et al. (1986, 1987, 1989). The verification of the present simulation against observational data demonstrates the capabilities of the model in reproducing much of the meso-β-scale structures and the evolution of the long-lived MCSs up to 90 hours. These include (i) the dissipation of the MCSs and the weakening of the surface mesolow to a mesotrough as they moved offshore; (ii) the maintenance of the mesovortex system; (iii) the timing and location of the initiation of a new MCS at 36 hr; (iv) the genesis of a surface low over the warm Gulf Stream water at 60 h and the subsequent evolution of the surface low leading eventually to the formation of a "tropical storm"; (v) the orientation and areal coverage of convective band associated with the storm. In addition, the evolution of the synoptic scale systems, a cold front and the subtropical high in relation to the storm, were simulated very well.

The initiation of new MCS at the southern periphery of the previous mesovortex over warm water is attributable to the interaction between the circulation of the mesovortex with the southwesterly flow of the subtropical high. The

mesovortex is characterized by a warm anomaly above and a cold anomaly below. Within a weak-sheared environment, the deep and vertically coherent vortex can be maintained for over 60 hr. As the surface trough associated with the mesovortex moved southeastward to the subtropical high, the pressure gradient ahead of the axis of the vortex/trough system intensified with time. This intensifying flow helped to enhance mesoscale convergence in the PBL and organized the deep convection. Furthermore, the flow increased surface energy fluxes from the warm water and transported air with higher θ_e aloft into regions with lower θ_e to produce further conditional instability. This mechanism resulted in persistent convection and contributed to amplification of the low-level cyclonic vorticity at the southern periphery of the mesovortex. After 66 hr, the intensifying flow of the developing surface cyclone, assisted by the northeasterly prefrontal flow, advected the cold air mass associated with the continental mesovortex into the area of active convection and transported warm air (by a wrapped around flow) into the cyclone. The processes caused the transformation of the low-level cold anomaly to a warm core structure and the pronounced concentration of cyclonic vorticity. The surface cyclone deepened rapidly to become a tropical storm.

Using idealized initial conditions, a 72 h simulation has also been carried out. The initial conditions resemble the basic structure of the subtropical high presented in BS81, but without the embedded frontal system which may have affected the formation of the tropical storm in the real-data case. The simulation is capable of reproducing the essential features associated with the life cycle of a mesovortex as

demonstrated in the RDS. The generation and dissipation of the mesovortex, the initiation of the second round of convection in the confluent zone created by the interaction between the circulation of the MCV and the southerly flow of the subtropical high, and the amplification of the vortex into a tropical storm are all simulated.

The diagnostic analysis for the idealized simulation also clarifies the processes responsible for the amplification of a low-level vorticity and the formation of a warm core in the environment without the influence of a cold front. By decomposing the vertical relative vorticity associated with the tropical storm into curvature vorticity and shear vorticity, our analysis shows that the amplification of the low-level vortex after 36 h is mainly contributed by the increase of curvature vorticity. The role of shear vorticity is reflected in the northeastern portion of the intensifying vortex at a later stage. This picture is different from that presented in the RDS, in which the shear vorticity, associated with a north-south oriented convective band, first increases in magnitude and is then advected into the center by a wrapped-around flow to be converted into curvature vorticity. The reason for the difference may be the influence of the northerly prefrontal flow on the evolution of the north-south convective band in the RDS which is not present in the idealized simulation.

The eye-like structure is simulated during the period of rapid deepening of a tropical storm. The vertical profile of vertical velocity of the surface low reveals that the descending motion is slow but persistent. The time averaged θ budget calculated over the eye-like area at 800 hPa shows that the formation of the warm core is caused

by this descending motion. This mechanism may not have been fully revealed in the RDS due to the presence of strong horizontal advection associated with the wrapped-around flow.

The impact of model physics on the idealized simulation was investigated through three groups of sensitivity experiments. The results show that the BM-CPS fails to simulate properly a mid-level mesovortex. When downdraft is included, the BM-CPS run can produce a shallow and weak cold pool instead of a deep couplet of a warm core and a cold pool. The absence of grid-scale condensation and its interaction with the CPS are the reasons for the failure of the BM-CPS to simulate properly the MCV structures. On the other hand, the shallow and weak cold pool is eliminated easily by surface energy fluxes when the system moves over warm water, so that the tropical storm forms too quickly. In addition, the time evolution of convective activity simulated in the BM-CPS run does not indicate the characteristic multiple-episodes of convection revealed in observational study of tropical cyclogenesis and the control simulation using the KF-CPS. In this case study, it appears that the simulation of a mid-level mesovortex and its transformation to a tropical storm by the KF-CPS is more realistic than the BM-CPS. However, we should not exclude the possibility of improving the BM-CPS run if suitable modification to the convective scheme can be made.

The sensitivity tests also show that the surface latent fluxes is a dominant factor in the production of CAPE to maintain the persistent convection, resulting in a positive feed back mechanism to spin up the storm. The cumulative cooling effect by

long wave radiation over three days is significant enough to destabilize the environment of the storm, thereby enhancing convection which is responsible for the rapid deepening of the tropical storm during the last 18 hours of the integration.

Future research should be directed toward the following areas:

The present study focuses on simulating the evolution of a long-lived mid-level mesovortex and its transformation into a warm core tropical storm in the westerly flow regime. However, a large number of tropical storms occur in the easterly flow regime. Therefore, a similar attempt should be made for the easterly flow. Our preliminary results (Appendix) show that a similar strategy used in the westerly flow is not effective for the easterly flow case, although the behavior of the mid-level mesovortex indicates many similarities in both flow regimes. One of the problems is associated with the less organized convection by the KF-CPS during the later stage. Although the BM-CPS captures much of the organized convection at the same stage, the shortcoming of the BM-CPS (Chapter 5) hinders its application to such simulations without any modification. This suggests the need to improve the KF-CPS or the BM-CPS in future studies. In addition, the creation of an environment having more realistic EFC may be critical for the success of simulating the second round of convective outbreak leading to the formation of a tropical storm in the easterly flow regime.

Appendix

The transformation of a mid-level mesovortex into a tropical storm in the easterly flow regime: preliminary results

Laing and Fritsch (1993) suggest that some MCCs originated from West Africa, can develop into tropical storms over the Atlantic Ocean. Based on climatological data, Gray and Landsea (1992) show high correlation between tropical storms in the western Atlantic Ocean and convective activity over West Africa. Motivated by these observational findings and the success of the aforementioned simulation, we attempted to simulate the transformation of a mid-level mesovortex into a tropical storm embedded in an easterly flow.

For our preliminary tests, we set the initial conditions for large scale flow identical to the one used in the idealized simulation, except for (i) southward shift of the fine mesh (reduced f parameter), (ii) the initiation of convection in the easterly flow, and (iii) the land-sea configuration now represents symbolically the coast line along West Africa. The model was integrated for 60 hours

Using the same approach as the control run in the idealized simulation, we initiated convection within a 300 km x 300 km area (shaded area in Fig. A1a). The time evolution of the area of convection is given in Fig. A3. At 6 h, convective

activity reaches its first peak. It then weakens but is near the original strength at 60 h, giving an indication of alternating phases of convective activity. The first round of convection is responsible for the generation of the mid-level MCV in the area of stratiform rainfall (not shown). Due to the weak vertical shear, the MCV maintains its identity even when the parent MCS dissipated. At 18 hr, the mesoscale surface trough just moved offshore, and all convection dissipated (Fig. A1b). The vertical cross section (A-B in Fig. A1b) of the relative vorticity and temperature deviation shows a typical mid-level vortex with a deep thermal couplet (Fig. A2a). The intensity of the vortex is comparable to that at a similar time period in the control case of the idealized simulation. By 60 h, a mesoscale surface low appears (Fig. A1c). The vertical structure of the relative vorticity associated with the low indicates some features of a tropical system. Fig. A2b shows that its maximum vorticity was located at 950 hPa. In addition, surface energy fluxes destroy the cold pool located within the boundary layer. Although the total areal coverage of convection increases between 48-60 h, the convective outbreak is less organized. The scattered convection around the surface low makes it difficult to concentrate the condensational heating to enable a self-sustaining development process. Thus, the surface low did not deepen any further when the integration was extended out to 72 h. (not shown)

The less organized convection occurring at the late stages may be due to the application of the convective triggering function of the KF-CPS, tested extensively for cases occurring at midlatitude, to the tropics. Using the BM-CPS, the simulation captured much of the organized convection at the same stage (not shown). However,

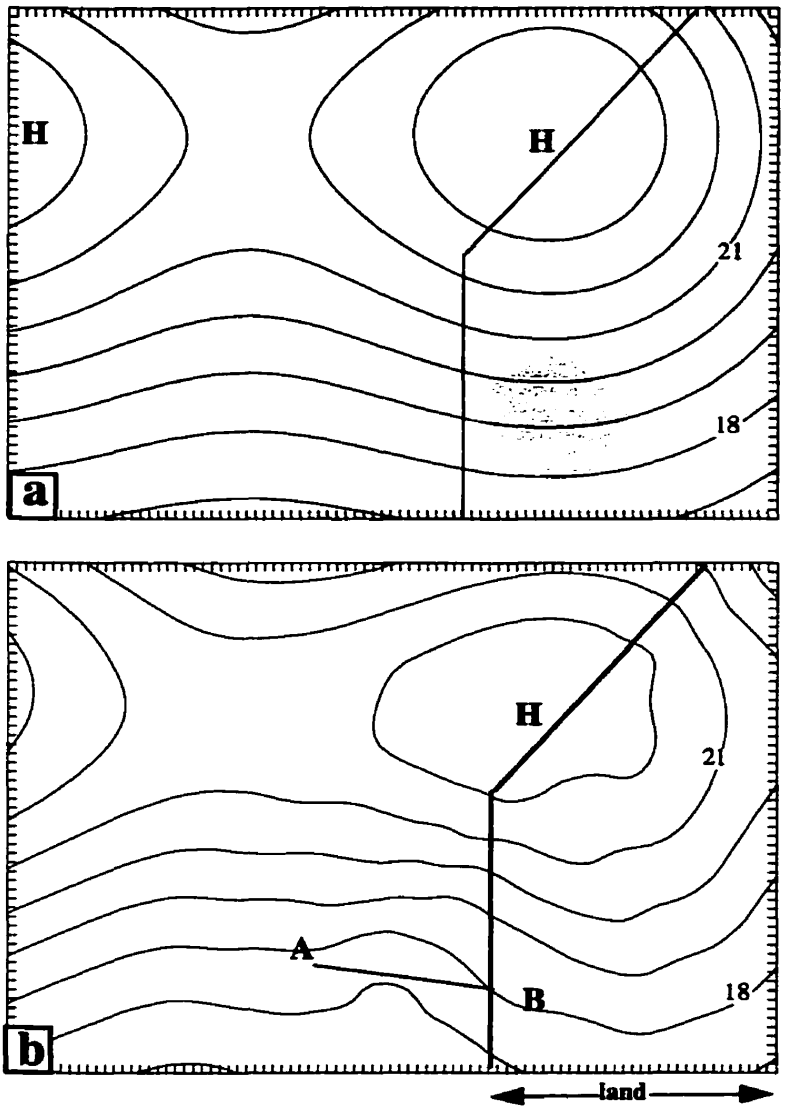

Fig. A1 The sea-level pressure (solid, every 1 hPa) and the convective areas (shaded) from (a) 0 h; (b) 18 h; and (c) 60 h integration. Line AB denotes the location of cross section used in Fig. A2.

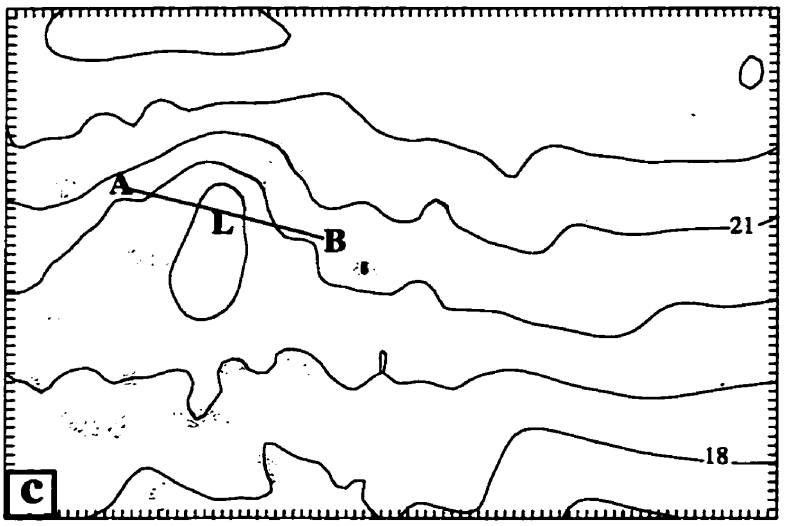

Fig. A1 (continued)

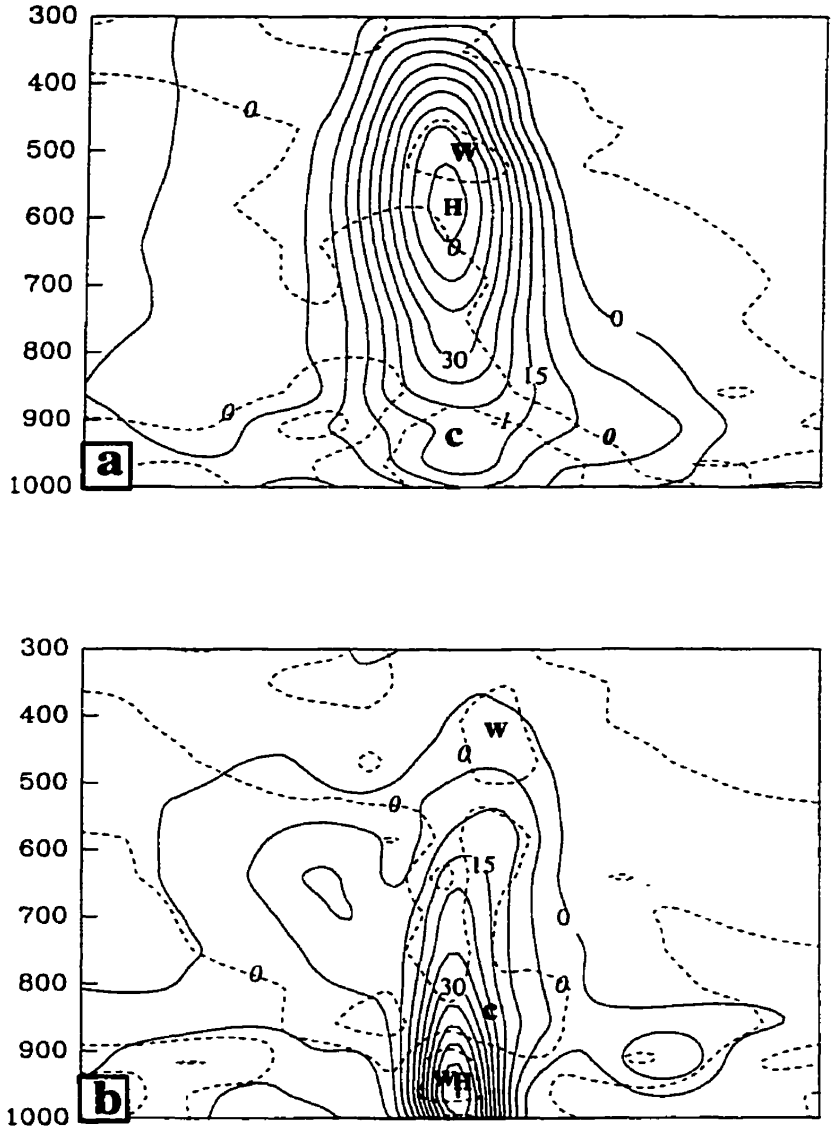

Fig. A2 Vertical cross section of vertical relative vorticity (solid) at intervals of 5×10^{-5} s^{-1}, superimposed with the deviation temperature (dashed) at intervals of 1°C at (a)18 h and (b) 60 h.

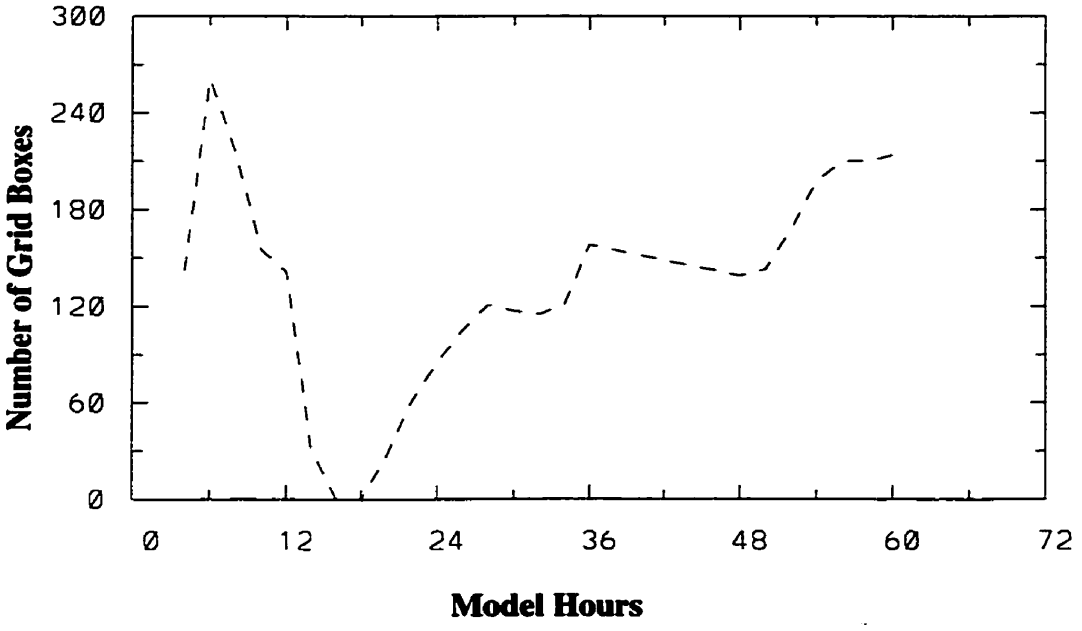

Fig. A3 The time evolution of the area (number of grid boxes) occupied by convection.

the BM-CPS used in the present study fails to simulate properly the structure of the mid-level mesovortex due to the absence of an effective interaction with grid-scale condensational processes (see Chapter 5). This suggests the need to improve the KF-CPS or the BM-CPS in future studies. Besides, the convective pattern leading to the formation of a tropical storm may vary with environment flow. Tuleya and Kurihara (1981) found that the 'comma' type of convection, with a northeast-southwest tail, is more frequently associated with a tropical storm in a westerly flow, while 'circular' type of convection is more frequently related to a tropical storm in an easterly flow. These differences were attributed to various factors such as the latitudinal variation of the Coriolis parameter and the low-level convergence patterns. In short, the simulation of the formation of a tropical storm in an easterly flow may not be achieved easily by using a strategy similar to that applied to developing cases in the westerly flow. To create the environment having more realistic EFC (Gray, 1998) in modeling studies may be critical for the success of simulating the second round of convective outbreak leading to the formation of a tropical storm in the easterly flow regime.

References

Anthes, R.A., 1982: *Tropical Cyclones: Their Evolution, Structure and Effects.* American Meteorological Society, 208pp.

--------,and D. P. Baumhefner, 1984: *A diagram depicting forecast skill and predictability. Bull. Amer. Meteor. Soc.*, **65**, 701-703.

--------,E.-Y. Hsie, and Y.-H. Kuo, 1987: Description of the Penn State/NCAR mesoscale model version 4 (MM4). NCAR Tech. Note NCAR/TN-282, 66pp.

Augustine, J. A., and K.W. Howard, 1988: Mesoscale convective complexes over the United States during 1985. *Mon. Wea. Rev.*, **116**,685-701.

--------, and --------, 1991: Mesoscale convective complexes over the United States during 1986 and 1987. *Mon. Wea. Rev.*, **119**, 1575-1589.

Baik, J.-J., M. DeMaria and S. Raman, 1991: Tropical cyclone simulations with the Betts convective adjustment scheme. Part III Comparisons with the Kuo convective parameterization. *Mon. Wea. Rev.* **119**, 2889-2899.

Bartels, D. L., and R. A. Maddox, 1991: Midlevel cyclonic vortices generated by mesoscale convective systems. *Mon. Wea. Rev.*, **119**, 104-118.

Bell, G. D., and D. Keyser, 1993: Shear and curvature vorticity and potential-vorticity interchanges: Interpretation and application to a cutoff cyclone event. *Mon. Wea. Rev.*, **121**, 76-102.

Benoit, R., J. Cote and J. Mailhot, 1989: Inclusion of a TKE boundary-layer parameterization in the Canadian regional finite-element model. *Mon. Wea. 7Rev.*, **117**, 1726-1750.

Burpee, R. W., 1972: The origin and structure of easterly waves in the lower troposphere of North Africa. *J. Atmos. Sci.*, **29**, 77-90.

--------,1974: Characteristics of North African easterly waves during the summers of 1968 and 1969. *J. Atmos. Sci.*, **31**, 1556-1570.

--------,1975: Some features of synoptic-scale waves based on compositing analysis of GATE data. *Mon. Wea. Rev.*, **103**, 921-925.

--------,1986: Mesoscale structure of hurricanes. *Mesoscale Meteorology and Forecasting*, P. S. Ray, Ed., American Meteorological Society, 311-330.

Betts, A. K., 1982: Saturation point analysis of moist convective overturning. *J. Atmos. Sci.*, **39**, 1484-1505.

--------,1986: A new convective adjustment scheme. Part I: Observational and theoretical basis. *Quart. J. Roy. Meteor. Soc.*, **112**, 677-692.

--------,and M. J., Miller, 1993: Convective parameterization for mesoscale models: The Betts-Miller scheme. *The Representation of Cumulus Convection in Numerical Models, Meteor.* Monogr., No. 46, Amer. Meteor. Soc., 107-121.

Bister, M. and K. A. Emanuel, 1997: The genesis of hurricane Guillermo: TEXMEX analyses and a modeling study. *Mon. Wea. Rev.*, **125**, 2662-2682.

Black, P. G., and G. J. Holland, 1995: The boundary layer of Tropical Cyclone Kerry (1979). *Mon. Wea. Rev.*, **123**, 2007-2028.

Black, T. L., 1994: The new NMC mesoscale Eta model: Description and forecast examples. *Wea. Forecasting*. **9**, 265-278.

Bosart, L. R., and F. Sanders, 1981: The Johnstown flood of July 1977: A long-lived convective storm. *J. Atmos. Sci.*, **38**, 1616-1642.

Charney, J. G., and Eliassen, A., 1964: On the growth of the hurricane depression. *J. Atmos. Sci.*, **21**, 68-75.

Chen, S. S. 1990: A numerical study of the genesis of extratropical convective mesovortices. Ph.D. Thesis, 178 pp, Penn State.

--------,and W. M. Frank, 1993: A numerical study of the genesis of extratropical convective mesovortices. Part I: Evolution and dynamics. *J. Atmos. Sci.*, **54**, 2401-2426.

Cotton, W.R., R. L. George, P.J. Wetzel, and R. L. McAnelly, 1983: A long-lived mesoscale convective complex. Part I: The mountain-generated component. *Mon. Wea. Rev.*, **111**, 1893-1918.

--------,M. S. Lin, R. L. McAnelly, and C. J. Tremback, 1989: A composite model of mesoscale convective complexes. *Mon. Wea. Rev.*, **117**, 765-783.

Davidson, N. E., G. I. Holland, J. L. McBride, and T. D. Keenan, 1990: On the formation of AMEX tropical cyclones Irma and Jason. *Mon. Wea. Rev.*, **118**, 1981-2000.

Davis, C.A. 1992: Piecewise potential vorticity inversion. *J. Atmos. Sci.*, **49**, 1397-1411

--------,and M. L.Weisman, 1994: Balanced dynamics of mesoscale vortices produced in simulated convective systems. *J. Atmos. Sci.*, **51**, 2005-2030.

Dovark, V., 1975: Tropical cyclone intensity analysis and forecasting. *Mon. Wea. Rev.*, **103**, 420-430.

Dudhia, J., 1989: Numerical study of convection observed during the winter monsoon experiment using a mesoscale two-dimensional model. *J. Atmos. Sci.*, **46**, 3077-3107.

Emanuel, K. A., 1986: An air-sea interaction theory for tropical cyclones. Part I : Steady state maintenance. *J. Atmos. Sci.*, **43**, 585-604.

--------,N. Renno, L. R. Schade, M. Bister, M. Morgan, D. Raymond, and R. Rotunno, 1993: Tropical cyclogenesis over the eastern North Pacific: Some results of TEXMEX. Preprints, *20th Conf. Hurricanes and Tropical Meteorology*, San Antonio, TX, Amer. Meteor. Soc., 110-113.

--------,K. A., 1997: Some aspects of hurricane inner-core dynamics and energetics. *J. Atmos. Sci.*, **54**, 1014-1026.

Frank, W. M., 1977a: The structure and energetics of the tropical cyclone, Part I: Storm structure. *Mon. Wea. Rev.*, **105**, 1119-1135.

--------,1977b: The structure and energetics of the tropical cyclone, Part II: Dynamics and energetics., **105**, 1136-1150.

Fritsch, J. M., and C. F. Chappell, 1980: Numerical prediction of convectively driven mesoscale pressure systems. Part I : Convective parameterization. *J. Atoms. Sci.*, **37**, 1722-1733.

--------,and R. A. Maddox, 1981: Convectively driven mesoscale weather systems aloft. Part I: Observations. *J. Appl. Meteor.*, **20**,9-12.

--------,and J. M. Brown, 1982: on the generation of convectively driven mesohighs aloft. *Mon. Wea. Rev.*, **110**, 1554-1563.

--------,R. J. Kane, and C. R. Chelius, 1986: The contribution of mesoscale convective weather systems to the warm-season precipitation in the United States. *J. Climate Appl. Meteor.*, **25**, 1333-1345.

--------,J. D. Murphy, and J. S. Kain, 1994: Warm-core Vortex amplification over land. *J. Atmos. Sci.*, **51**, 1780-1807.

Gamache, J. F., and R. A. Houze Jr. 1985: Further analysis of the composite wind and thermodynamic structure of the 12 September GATE squall line. *Mon. Wea. Rev.* **113,** 1241-1259.

Garand, L., 1983: Some improvements and complements to the infrared emissivity algorithm including a parameterization of the absorption in the continuum region. *J. Atmos. Sci.*, **40**, 230-244.

Gray, W. M., 1979: Hurricanes: their formation, structure and likely role in the tropical circulation. Supplement of Meteorology Over the tropical Oceans. Published by RMS, James Glaisher Hourse, Grenville Place, Brackbell, Bershire, RG 12 1BX, D. B. Shaw, (ed)., 155-218.

--------,and C. W. Landsea, 1992: African rainfall as a precursor of hurricane-related destruction on the U.S. east coast. *Bull. Amer. Meteor. Soc.*, **73,** 1352-1364

--------,1998: The formation of tropical cyclones. *Meteo. Atmos. Phys.*, **67,** 37-69.

Harr, P. A. and R. L. Elsberry, 1996: Structure of a mesoscale convective system embedded in typhoon Robyn during TCM-93. *Mon. Wea. Rev.*, **124**, 634-652.

--------,M. S. Kalafsky, and R. L. Elsberry, 1996: Environment conditions prior to formation of a midget tropical cyclone during TCM-93. *Mon. Wea. Rev.*, **124**, 1693-1710.

--------,and R. L. Elsberry, 1996: Transformation of a large monsoon depression to a tropical storm during TCM-93. *Mon. Wea. Rev.*, **124**, 2625-2643.

Hawkins, H. F., and D. T. Rubsam, 1968: Hurricane Hilda, 1964 I. Genesis as revealed by satellite photographs, conventional and aircraft data. *Mon. Wea. Rev.*, **96**, 428- 452.

Houze, R. A., Jr., 1989: Observed structure of mesoscale convective systems and implications for large-scale heating. *Quart. J. Roy. Meteor. Soc.*, **115**, 425-461.

Hoxit, L. R., R. A. Maddox, C. F. Chappell, F. L. Zuckerberg, H. M. Mogil, I. Jones, D. R. Greene, R. E. Saffle, and R. A. Scofield, 1978: Meteorological analysis of the Johnstown, Pennsylvania flash flood, 19-20 July 1977. NOAA Tech. Rep. ERL 401-APCL43, 71 pp.

Hsie, E.-Y., R. A. Anthes, and D. Keyser, 1984: Numerical simulation of frontogenesis in a moist atmosphere. *J. Atmos. Sci.*, 41, 2581-2594.

Huo, Z., D.-L. Zhang, and J. Gyakum, 1998: An application of potential vorticity inversion to improving the numerical predication of the March 1993 superstorm. *Mon. Wea. Rev.*, **126**, 424-436.

Janjic, Z. I., 1994: The step-mountain Eta coordinate model: Further developments of the convection, viscous sublayer, and turbulence closure schemes. *Mon. Wea. Rev.*, **122**,927-945.

Kain, J. S., and J. M. Fritsch, 1990: A one-dimensional entraining/detraining plume model and its application in convective parameterization. *J. Atmos. Sci.*, **47**, 2784-2802.

--------,and--------,1993: Convective parameterization for mesoscale models: The Kain-Fritsch scheme. *The Representation of Cumulus Convection in Numerical Models, Meteor.* Monogr., No. 46, Amer. Meteor. Soc., 165-170.

-------,and--------,1997: Interactions between convective and stratiform precipitation regimes in meso-β scale simulation of a tropical cyclone. Preprints, *21st - Conference on hurricane and tropical meteorology.* Amer. Meteor. Soc. 419-421.

--------,1999: Parameterized convection and the quantitative precipitation problem. Preprints, *23rd Conference on hurricane and tropical meteorology.* Dallas, Texas, Amer. Meteor. Soc. 870-872.

Krishnamurti, T. N., K. S. Yap, and D. K. Oosterhof, 1991: Sensitivity of tropical storm forecast to radiative destabilization. *Mon. Wea. Rev.*, **119**, 2176-2205.

Kuo, Y.-H., and R. A. Anthes, 1984: Mesoscale budgets of heat and moisture in a convective system over the central United States. *Mon. Wea. Rev.*, **112**, 1482-1497.

Kurihara, Y., and R. E. Tuleya, 1981: A numerical simulation study on the genesis of a tropical storm. *Mon. Wea. Rev.*, **109**, 1629-1653.

Laing, A. G., and J. M. Fritsch, 1993: Mesoscale convective complexes over the Indian monsoon region. *J. Glimate*, **6**, 911-919.

Liu, Yubao, Da-Lin Zhang and M.K. Yau, 1997: A multiscale numerical study of Hurricane Andrew (1992). Part I: Explicit simulation and verification. *Mon. Wea. Rev.*, **125**, 3073-3093.

Lopez, L., D. Raymond, and K. Emanuel, 1993: Preliminary results from TEXMEX: The development of tropical storm Guillermo. Preprints, *20th Conf.*

Hurricanes and Tropical Meteorology, San Antonio, TX, Amer. Meteor. Soc., 114-117.

Maddox, R. A., 1980: Mesoscale convective complexes. *Bull. Amer. Meteor. Soc.*, **61**, 1374-1387.

--------,D. M. Rodgers, and K. W. Howard, 1982: Mesoscale convective complexes over the United States during 1981---Annual Summary. *Mon. Wea. Rev.*, **110**, 1501-1514.

--------,1983: Large-scale meteorological conditions associated with midlatitude mesoscale convective complexes. *Mon. Wea. Rev.*, **111**, 1475-1493.

Mapes, B. E., and R. A. Houze Jr., 1993: An integrated view of the 1987 Australia monsoon and its mesoscale convective systems. Part II: Vertical structure. *Quart. J. Roy. Meteor. Soc.*, **119**, 733-754.

--------,and--------,1995 : Diabatic divergence profiles in western Pacific mesoscale convective systems. *J. Atmos. Sci.*, **52**, 1807-1828.

McAnelly, R. L., and W. R. Cotton, 1989: The precipitation life cycle of mesoscale convective complexes over the central United States. *Mon. Wea. Rev.*, **117**, 784-808.

McBride, J. L., 1981a: Observational analysis of tropical cyclone formation, Part I: basic description of data sets. *J. Atmos. Sci.*, **38**, 1117-1131.

--------,1981b: Observational analysis of tropical cyclone formation, Part III: Budget analysis. *J. Atmos. Sci.*, **38**, 1152-1166.

Menard, R. D., and J. M. Fritsch, 1989: A mesoscale convective complex-generated inertially stable warm core vortex. *Mon. Wea. Rev.*, **117**, 1237-1261.

Miller, D., and J. M. Fritsch, 1991: Mesoscale convective complexes in the western Pacific region. *Mon. Wea. Rev.*, **119**, 2978-2992.

Molinari, J., and M. Dudek, 1992: Parameterization of convective precipitation in mesoscale numerical models. A critical review. *Mon. Wea. Rev.*, **120**, 326-344.

Montgomery, M. T., and J. Enagonio, 1998: Tropical cyclogenesis via convectively forced vortex Rossby waves in a three-dimensional quasigeostrophic model. *J. Atmos. Sci.*, **55**, 3176-3206.

Parsons, D., W. Dabberdt, H. Cole, T. Hock, C. Martin, A.-L. Barrett, E. Miller, M. Spowart, M. Howard, W. Ecklund, D. Carter, K. Gage, and J. Wilson, 1994: The integrated sounding system: Description and preliminary observations from TOGA COARE. *Bull. Amer. Meteor. Soc.*, **75**, 553-567.

Perkey, D. J., and C. W. Kreitzberg, 1976: A time-dependent lateral boundary scheme for limited-area primitive equation models. *Mon. Wea. Rev.*, **104**, 744-755.

Raymond, D. J., and H. Jiang, 1990: A theory for long-lived mesoscale convective systems. *J. Atmos. Sci.*, **47**, 3067-3077.

--------,1992: Nonlinear balance and potential-vorticity thinking at large Rossby number. *Quart. J. Roy. Meteor. Soc.*, **118**, 987-1105.

Rodgers, D. M., K. W. Howard, and E. C. Johnston, 1983: Mesoscale convective complexes over the United States during 1982---Annual summary. *Mon. Wea. Rev.*, **111**, 2363-2369.

--------, M. J. Magnano, and J. H. Arns, 1985: Mesoscale convective complexes over the United States during 1983--- Annual summary. *Mon. Wea. Rev.*, **113**, 888-901.

Rogers, R. F., 1999: Amplification of warm-core vortices by convective redevelopment: a key component of tropical cyclogenesis. Preprints, *23rd Conference on hurricane and tropical meteorology.* Dallas, Texas, Amer. Meteor. Soc. 929-932.

Rosenthal, S. L., 1979: The sensitivity of simulated hurricane development to cumulus parameterization details. *Mon. Wea. Rev.*, **107**, 193-197.

Rothman, L.S., and Co-authors, 1987: The HITRAN database: 1986 edition. *Appl . Optics*, **26**, 4058-4097.

Rotunno, R., and K. A. Emanuel, 1987: An air-sea interaction theory for tropical cyclones. Part II: Evolutionary study using a nonhydrostatic axisymmetric numerical model. *J. Atmos. Sci.*, **44**, 542-561.

Ryan, B. F., G. M. Barnes, and E. J. Zipser, 1992: A wide rainband in a developing tropical cyclone. *Mon. Wea. Rev.*, **120**, 431-447.

Sadler, J., 1976: A role of the tropical upper tropospheric trough in early season typhoon development. *Mon. Wea. Rev.*, **104**, 1266-1278.

--------, 1978: Mid-season typhoon development and intensity changes and the tropical tropospheric trough. *Mon. Wea. Rev.*, **106**, 1137-1152.

Schubert, W. H., and J. J. Hack, 1982: Inertial stability and tropical cyclone development. *J. Atmos. Sci.*, **39**, 1687-1697.

Shapiro, L. J., 1977: Tropical storm formation form easterly waves: A criterion for development. *J. Atmos. Sci.*, **34**, 1007-1021.

--------,and H. E. Willoughby, 1982: The response of balanced hurricanes to local sources of heat and momentum. *J. Atmos. Sci.*, **39**, 378-394.

Simpson, R. H. , N. Frank, D. Shideler and H. M. Johnson, 1968: Atlantic tropical disturbances, 1967. *Mon. Wea. Rev.*, **96**, 251-259.

--------,J. B. Halverson, B. S. Ferrier, W. A. Petersen, R. H. Simpson, R.Blakeslee, and S. L. Duren, 1998: On the role of " hot towers" in tropical cyclone formation. *Meteo. Atmos. Phys.*, **67**, 15-35.

-------,E. Ritchie, G. J. Holland, J. Halverson and S. Stewart, 1997: Mesoscale interaction in tropical cyclone genesis. *Mon. Wea. Rev.*, **125**, 2643-2661.

Stull, R. B., 1985: Predictability and scales of motion. *Bull. Amer. Meteor. Soc.*,**66**, 432-436.

Tuleya, R. E., and Y. Kurihara, 1981: A numerical study on the effects of environmental flow on tropical storm genesis.

--------,and--------,1984: The formation of comma vortices in a tropical numerical simulation model. *Mon. Wea. Rev.*, **112**, 491-502.

Velasco, I., and J. F. Fritsch, 1987: Mesoscale convective complexes in the Americas. *J. Geophys. Res.*, **92**, 9591-9613.

Vincent, D. G., and R. G. Waterman, 1979: Large-scale atmospheric conditions during the intensification of Hurricane Carmen (1974). I. Temperature, moisture and kinematics. *Mon. Wea. Rev.*, **107**, 283-294.

Wallace, J. M., 1975: Diurnal Variations in precipitation and thunderstorm frequency over the continental United States. *Mon. Wea. Rev.*, **103**, 406-419.

Webster, P. J., and R. Jukas, 1992: TOGA COARE: The coupled ocean-atmosphere response experiment. *Bull. Amer. Meteor. Soc.*, **73**, 1377-1416.

Wetzel, P. J., W. R. Cotton, and R. L. McAnelly, 1983: A long-lived mesoscale convective complex. Part II: Evolution and structure of the mature complex. *Mon. Wea. Rev.*, **111**, 1919-1937.

Willoughby, H. E., 1998: Tropical cyclone eye thermodynamics. *Mon. Wea. Rev.*, **126**, 3053-3067.

Yanai, M., 1961: Dynamical aspects of typhoon formation. *J. Meteor. Soc. Japan*, **39**(4), 282-309.

------, 1968: Evolution of a tropical disturbance in a Caribbean Sea region. *J. Meteor. Soc. Japan*, II, **46**, 86-108.

------, S. Esbensen, and J. Chu, 1973: Determination of bulk properties of tropical cloud clusters from large-scale heat and moisture budgets. *J. Atmos. Sci.*, **30**, 611- 627.

Zehr, R. M., 1992: Tropical cyclogenesis in the western North Pacific. *NOAA Technical report NESDIS* 16, 181pp. (available from NESDIS, Washington, DC or CIRA, Colo. State Univ., Ft. Collins, CO).

Zhang, D. L., and R. A. Anthes, 1982: A high-resolution model of the planetary boundary layer, Sensitivity tests and comparison with SESAME-79 data. *J. Appl. Meteor.*, **21**, 1594-1609.

--------,and J. M. Fritsch, 1986: Numerical simulation of the meso-β-scale structure and evolution of the 1977 Johnstown flood. Part I: Model description and verification. *J. Atmos. Sci.*, **43**, 1913-1943.

--------,H. -R. Chang, N. L. Seaman, T. T. Warner, and J. M. Fritsch, 1986: A two-way interactive nesting procedure with variable terrain resolution. *Mon. Wea. Rev.*, **114**, 1330-1339.

--------,and--------,1987: Numerical simulation of the meso-β-scale structure and evolution of the 1977 Johnstown flood. Part II: Inertially stable warm-core vortex and the mesoscale convective complex. *J. Atmos. Sci.*, **44**, 2593-2612.

--------,and--------,1988a: A numerical investigation of a convectively generated, inertially stable, extratropical warm-core mesovortex over land. Part I: Structure and evolution. *Mon. Wea. Rev.*, **116**, 2660-2687.

--------,and--------,1988b: Numerical sensitivity experiments of varying model physics on the structure, evolution and dynamic of two mesoscale convective systems. *J. Atmos. Sci.*, **45**, 261-293.

--------,E.-Y. Hsie, and M. W. Moncrieff, 1988c: A comparison of explicit and implicit prediction of convective and stratiform precipitating weather systems

with a meso-β-scale numerical model. *Quart, J Roy. Meteor. Soc.*, **114**, 31-60.

--------,1989: The effect of parameterized ice microphysics on the simulation of vortex circulation with a mesoscale hydrostatic model. *Tellus*, **41A**, 132-147.

--------,J. S. Kain, J. M. Fritsch, and K. Gao, 1994: Comments on "Parameterization of convective precipitation in mesoscale numerical models. A critical review." *Mon. Wea. Rev.*, **122**, 2222-2231.

--------,and N. Bao, 1996a: Oceanic cyclogenesis as induced by a mesoscale convective system moving offshore. Part I: A 90-h real-data simulation. *Mon. Wea. Rev.*, **124**, 1449-1469.

--------,and N. Bao, 1996b: Oceanic cyclogenesis as induced by a mesoscale convective system moving offshore. Part II: Genesis thermodynamic transformation. *Mon. Wea. Rev.*, **124**, 2206-2225.

--------,Y. Liu, and M.K. Yau, 1999: A multiscale numerical study of Hurricane Andrew (1992). Patrt III: Dynamically-induced vertical motion. *Mon. Wea. Rev.* (in press)

Zipser, E. J., 1977: Mesoscale and convective-scale downdrafts as distinct components of squall-line structure. *Mon. Wea. Rev.*, **105**, 1568-1589.